Atomic and molecular ionization dynamics in strong IR and XUV fields probed by time-resolved coincidence spectroscopy

Oliver Herrwerth

München 2011

Atomic and molecular ionization dynamics in strong IR and XUV fields probed by time-resolved coincidence spectroscopy

Oliver Herrwerth

Dissertation
an der Fakultät für Physik
der Ludwig–Maximilians–Universität
München

vorgelegt von
Oliver Herrwerth
aus Weinheim

München, den 17.10.2011

Erstgutachter: Prof. Dr. Matthias Kling
Zweitgutachter: Prof. Dr. Armin Scrinzi
Tag der mündlichen Prüfung: 13.12.2011

Abstract

In the work for this thesis, a split-mirror-setup was designed and build, which was used to split the XUV laser-pulse of FELs (Free Electron Laser) into two identical pulses from which one can be delayed. With this setup the laser pulses of FLASH, Hamburg and SCSS, Harima(Japan) where characterized temporally, to determine the temporal pulse-structure for subsequent experiments. The intermolecular dynamics of the homonuclear diatomic molecules nitrogen and oxygen were examined and the experimental results were reproduced by classical simulations. In the measurement with oxygen for an energy band of the coincident singly charged ions, an ionization probability was found that depends on the delay between the two XUV-pulses. This can most probably be explained by the autoionization of an excited singly charged molecular state. Subsequently the investigation of the two photon double ionization (TPDI) of deuterium is presented. In the single pulse experiments simulations within the Born-Oppenheimer approximation made it possible to distinguish between the direct and sequential TPDI. In the pump-probe experiments light was shed onto the dynamics of the TPDI. In addition, experiments with strong few-cycle near-infrared (NIR) pulses are presented that examined the carrier envelope phase (CEP) dependence of the non-sequential double ionization of argon. Implementing single-shot CEP-tagging in conjunction with coincidence spectroscopy allowed to achieve unprecedented accuracy in measuring correlated electron dynamics.

Zusammenfassung

In dieser Arbeit wurde ein "Split-Mirror-Setup" aufgebaut mit dem XUV Laserpulse von FELs (Freie Elektronen Laser) in zwei identische Lichtpulse aufgeteilt und einer der beiden verzögert werden konnte. Mit diesem Aufbau wurden die XUV-FELs FLASH in Hamburg und SCSS in Harima, Japan zeitlich charakterisiert, um die Pulsstruktur für die Analyse anschließender Experimente zu ermitteln. Die innermolekulare Dynamik der homonuklearen diatomaren Moleküle Stickstoff und Sauerstoff wurde untersucht und die experimentellen Ergebnisse mittels klassischer Simulationen reproduziert. In den Messungen mit Sauerstoff wurde in einem Energiebereich der koinzidenten einfachgeladenen Sauerstoffionen eine Ionisationswahrscheinlichkeit gefunden, welche von dem zeitlichen Versatz der beiden XUV Pulse abhängt. Diese Dynamik kann vermutlich mit der Autoionisation eines angeregten einfachgeladen Molekülzustandes erklärt werden kann. Anschließend wurde anhand von Deuterium die Doppelionization mit zwei Photonen (engl. TPDI) untersucht. In den Einzelpuls Experimenten konnte mittels Simulationen innerhalb der Born-Oppenheimer Näherung zwischen der direkten und der sequentiellen TPDI unterschieden werden. In Pump-Probe Messungen waren wir in der Lage, die Dynamik der TPDI zu beleuchten. Des Weiteren wurden Experimente durchgeführt, um die Abhängigkeit der nicht sequentiellen Doppelionization in starken nah-infraroten (NIR) Laserfeldern, bestehend aus nur wenigen Zyklen von der Träger-Einhüllende-Phase (engl. carrier-envelope phase, CEP), zu untersuchen. Durch den Einsatz der Einzelschuss CEP-Messung konnte eine bisher nicht erreichte Genauigkeit in der Messung korrelierter Elektronenprozesse erreicht werden.

Contents

Preamble

Light induced non-linear reactions were observed first in 1931, when Göppert-Mayer predicted that the energies of more than one photon can be absorbed to ionize a bound electron [1]. Although the first signs of two-photon processes had been measured in the radio frequency absorption spectra of molecular Rubidium fluoride in 1950 [2], it took until the development of the laser in the 60ies to provide experimental results to prove multi-photon ionization [3]. Nearly at the same time it was found that mechanisms of non-linear ionization depend on the frequency as well as the intensity of the light. In this time basic theoretical concepts for strong-field-induced phenomena, which are still valid today, were developed [4–7]. Especially in the pioneering work of Keldysh, quantitative conditions for the practicality of the perturbative photon or the quasi-static non-perturbative field description of non-linear optical processes have been developed [4].

With the development of laser sources with even higher intensities, it became possible to release more than one electron from an atom. Since the first observation of doubly charged ions produced by multi-photon ionization [8], many-electron dynamics and electron-electron correlations in intense laser pulse interacting with matter [9, 10], along with the studies of few-electron ionization with single photon absorption [11, 12], have become one of the most interesting topics in atomic, molecular and optical physics. Whereas the latter process, where the electrons have to share the energy of a single photon, is only possible due to electron-electron correlation. It turned out that in case of strong field double or multiple ionization, both independent ("sequential") or correlated ("direct" or "non-sequential") electron emission takes place. Which one is taking place depends on the parameters of the light field and the atomic or molecular structure. In particular, field induced correlation by laser-driven electron recollision was found to be of crucial importance at moderate field intensities, in some cases enhancing multiple ionization cross sections for linearly polarized light by many orders of magnitude [13–16]. However, the details of the underlying dynamics are not completely settled and are subject of continuing experimental as well as theoretical effort (see e.g. [17–20]).

Until very recently, measurements of non-linear few-electron processes were only possible in the optical and infrared domain, where a non-perturbative description of the light-atom interaction is required. In the last ten to twenty years the rapid development of laser- (high-harmonic generation, HHG) [21, 22] and accelerator-based (FEL) [23–26] light sources made it possible to generate intense, ultra short pulses with a wavelength from the XUV up to the X-ray regime. Those made it feasible to extend experiments on multi-

photon multi-electron reactions towards the perturbative regime at shorter wavelengths. This regime is not accessible with synchrotron sources [27–45]. Enormous theoretical interest has emerged to describe basic few-photon few-electron reactions for simple atomic and molecular systems because of their fundamental nature and some practical applications.(see [46–65] for a selection of recent publications). Furthermore, these novel light sources, which currently provide pulses shorter than ten fs with the realistic prospects of reaching into the sub-fs regime (FELs), or even less than one hundred as (HHG), are opening the door for a variety of novel time-resolved experiments. These will significantly extend the borders of today's ultrafast science, not only in terms of the time resolution that can be achieved ([66–68], see [21] for a current review), and new electronic states that can be accessed with exclusively or X-ray pulses [66, 69, 70], also in terms of techniques imaging the dynamics. In particular, time-resolved X-ray diffraction [71] or electron holography [72] experiments raise the hope of recording the "molecular movie", i.e. tracking the nuclear motion during a chemical reaction. Also the three dimensional imaging of photo-electrons emerging upon absorption of an XUV- or X-ray probe pulse will enable to directly follow the evolution of electronic states during the "breaking and making" of molecular bonds without the need of spectroscopic information as in a typical femto-chemistry experiment in the optical regime [73].

Decades of research with intense optical lasers and synchrotron radiation established dedicated experimental tools for investigation of multiple ionization and fragmentation processes in atoms and molecules. Starting with measuring intensity-dependent ion yields and total ionization cross sections respectively and continuing with measurements of single or multiple differential cross sections, instrumental progress recently culminated in experiments yielding fully differential data for fragmentation of simple atomic [17, 74–76] and molecular [77–80] systems. Here, a major step was achieved with the invention of coincident cold-target recoil-ion and electron momentum spectroscopy. These spectrometers (sometimes called "reaction microscopes" [81–84]), based on combined electric- and magnetic-field projection techniques, time- and position-sensitive micro-channel plate (MCP) detectors and supersonic gas jets providing cold atomic or molecular targets, allowed for the simultaneous and coincident measurement of the full 3D momentum vectors for several charged reaction fragments (the so-called kinematically complete experiments). Due to the fact that the fragments are imaged with a large (often reaching 4π) solid angle, in many cases these spectrometers enabled recording complete probability densities of the final many-particle momentum states. This, along with the possibility of reliable background elimination procedures applying momentum conservation conditions [84, 85] generating remarkable clean spectra, made this technique extremely successful in time-resolved experiments [69, 70, 86–90]. Because of its capabilities to separate different reaction channels leading to the same final states and cleanly revealing even weak ionization pathways based on the energy- and angular-resolved many particle detection, this approach has now become a state of the art technique for FEL [36, 37, 40–44, 91] and HHG [69, 70] based atomic and molecular research.

With IR lasers, time resolved measurements [73, 87, 88, 92–95] gave ground breaking insight into the dynamics of molecular reactions. Here, higher charge states of the molecules

can be reached via multi-photon and tunnel ionization processes. The combination of time resolved experiments with XUV light from FELs or HHG sources [66, 67, 70, 96–98], allowed to examine dynamics of higher ionized states of atoms and molecules that are produced within a single or multi-photon excitation.

In the first chapter the theoretical background for the understanding of the experiments performed with XUV-radiation and reaction microscopes during this work is introduced. It starts with an overview of ionization mechanisms in matter-light interactions, and then an introduction into the single photon interactions in the perturbation picture, valid in the XUV experiments, is given. In the end of this chapter an insight is given into the concepts of molecular physics necessary for the experiments performed with deuterium, nitrogen and oxygen as target gases.

The second chapter describes the experimental tools used to perform the experiments. In the beginning the technique of Free Electron Lasers (FELs) is explained. These FELs were used because until now they are the only machines that are able to produce XUV radiation with such intensities to perform multi-photon experiments. After this the reaction microscope is explained that was mentioned before and also the calculation of the momenta is detailed. Then the split mirror setup that enabled us to perform XUV pump XUV probe measurements at the FELs in Hamburg and in Harima, Japan is introduced.

The third chapter is the first chapter to describe experimental results. The intermolecular reaction dynamic in molecules in oxygen and nitrogen triggered by a pumping ionization with an XUV pulse and the evolution in the pumped state and then the final Coulomb explosion is induced by a second XUV pulse is investigated. This way a nearly unperturbed molecule can be examined. This leads to a nearly perfect benchmark experiment to test molecular theories. Here a simple simulation using Newton's physics is performed. The most limiting factor is the absence of molecular potential curves of highly excited molecules.

In the fourth chapter the temporal behavior of free electron laser pulses is characterized. These pulses show a totally different temporal behavior than the IR laser pulses used for the experiments chapter in seven. While IR pulses are relatively Gaussian shaped, the pulses of FELs consists of several spikes and due to the stochastically formation from shot noise (see section 2.1) none looks like the other. With the split mirror setup described in section 2.3 it was possible to measure autocorrelation traces the FLASH in Hamburg, Germany and SCSS in Harima, Japan. These pulse characterizations are necessary to enable the modeling of the experiments performed at these FELs described in the subsequent chapters. We were the first to characterize the pulses at SCSS but only the second to perform such measurements at FLASH.

Chapter number five is dedicated to transient depletion of inner-valence states with a subsequent autoionization in oxygen. The time-dependence of this autoionization mechanism could be measured. Especially for molecules, autoionization is an important electronic many-body problem where not many theories are available because the wave-functions cannot be described in the Born-Oppenheimer approximation. It was found that the autoionization distance is in the order of 30 Å. This long range interaction between the two oxygen atoms is usually neglected.

The sixth chapter describes the two photon double ionization of deuterium. It is among the most fundamental nonlinear processes in atomic physics and it can be considered as a benchmark process to test nonlinear theories and to investigate electron-electron correlations in atoms and the coupling between electronic and nuclear motion in molecules beyond the Born-Oppenheimer approximation (BOA). In this experiment it was possible to distinguish between the direct two photon double ionization and the sequential one. The split mirror setup enabled us to trace the time dependence of this processes in agreement with calculations presented in this chapter. This model experiment leads the way to the understanding of the two photon double ionization in more complex systems.

The sevenths and last chapter describes experiments that were performed independently to examine strong-field near-IR ionization in contrast to the XUV experiments. Here although the light has the same intensities, because of the much larger wavelength, the ionization shows a completely different characteristic and has to be described in the field regime. The chapter introduces strong-field ionization of atoms, describes the femtosecond laser system and the setup used for single-shot CEP tagging. Finally, the CEP dependence of the non-sequential double ionization (NSDI) of argon and neon is examined. Special attention is put in the different behavior of the two doubly ionization mechanism of NSDI with direct recoil ionization where the second ionization is an $(e, 2e)$-like process on the one hand and recoil excitation with subsequent tunneling ionization (RESI) on the other. In the NSDI of argon RESI is the dominant ion process while in the NSDI of neon the $(e, 2e)$-like process is dominant. Therefore these two rare gases are perfect model systems to explore the different behaviors of the CEP dependence of the two different processes.

Chapter 1

Theory

In this chapter a short introduction into the theory of the interaction between matter and light and molecular reactions is given.

In the first part the interaction of light with matter is explained starting with the dipole interaction parameter, which is subsequently handled within the dipole approximation. Afterwards the selection rules in one photon transitions, that are important for the XUV experiments, are deduced. To give a general view of the effects of single ionization these are discussed before the trajectories of charged particles in an oscillating field are investigated. The latter are necessary to understand the mechanisms of the non sequential double ionization which is explained at the end of this chapter.

1.1 Ionization of atoms and molecules in light-fields

In principle there are four different types for ionization with light that can be treated within different models: The single-photon ionization (1), the multi-photon ionization (2), the tunneling ionization (3) and the over-the-barrier ionization (4). The ionization schemes (1) and (2) are described in the photon pictures, while (3) and (4) can be described via light as a time-dependent electric field.
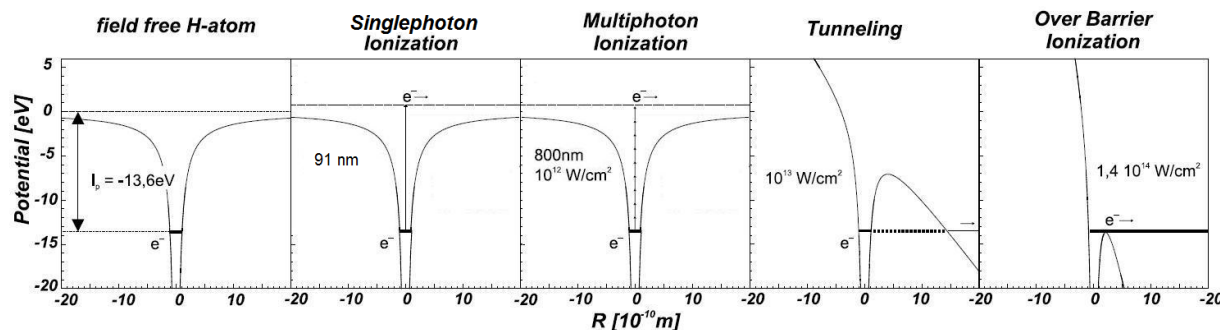

Figure 1.1: Mechanisms of the ionization of atoms on the example of Hydrogen. (Figure from [99])

Keldysh showed in his groundbreaking work in 1965, that all these mechanisms are only different aspects of the universal process of nonlinear photoionization [4].

Whereas the single- and the multi-photon ionization can be explained to a good approximation with perturbation theory, the tunneling ionization which occurs at higher intensities can be explained using the electric field of the laser pulse. To distinguish the cases where the two models are valid, Keldysh considered the time an electron takes to tunnel through the potential barrier as given in 1.1.

$$t = \frac{\sqrt{2m_e I_P}}{eE} \propto \omega_t^{-1},\tag{1.1}$$

where I_P is the ionization potential of the atom or molecule and E is the momentary electric field strength. The Keldysh parameter γ puts this frequency ω_t in relation to the external electric field and the ionization potential I_P to the ponderomotive potential U_P respectively,

$$\gamma = \frac{\omega_{laser}}{\omega_t} = \sqrt{\frac{I_P}{2\,U_P}}.\tag{1.2}$$

where U_P is the ponderomotive potential, averaged over at least one cycle of the electric field average kinetic energy of an oscillating electron within the laser field. It is defined as:

$$U_P = \frac{e^2 E_0^2}{4m_e\omega_{laser}^2} = \frac{Ie^2\lambda^2}{2\pi\varepsilon_0 c^2 m_e},\tag{1.3}$$

here E_0 is the maximum electric field strength of the oscillating field with frequency ω. This means U_P is proportional to the square of the wavelength. At a wavelength of 800 nm and an intensity $I = 10^{13}\text{W/cm}^2$ U_P is 0.6 eV while at a XUV wavelength of 30 nm U_P is significantly smaller with $8.5 \cdot 10^{-4}$ eV. Therefore U_P can typically be neglected in the XUV wavelength regime and the photon picture has to be applied, even if the electic field of the light has the same strength.

Two cases are distinguished: If the oscillation period of the external electric field is small in comparison to the tunneling time, tunneling ionization can occur and represent an adequate picture to describe the ionization. This is true for:

$$\gamma \ll 1,\tag{1.4}$$

tunneling regime.

But if the oscillation time is short in comparison to the tunneling time, this picture can not be used and the ionization has to be treated in the photon picture. In this case it is valid when:

$$\gamma \gg 1,\tag{1.5}$$

photon regime.

1.2 Perturbation Theory

As described in the last section, when the Keldysh parameter γ is larger than one, the photon picture in the pertubation regime has to be applied. This is the case for XUV radiation.

The basis to the description of the atom-light interaction is the Hamilton operator $\hat{H}$ of the system. It consists of the Hamiltonian of the free atom $\hat{H}_{at}$ and the atom-light interaction operator $\hat{V}$:

$$\hat{H} = \hat{H}_{at} + \hat{V} \tag{1.6}$$

We imagine the atom thereby simplified as a two level system. This means that there is a ground state $|1\rangle$ as well as an excited state $|2\rangle$, which are separated by an energy difference of $\Delta E_{21} = \hbar (\omega_2 - \omega_1) = \hbar \omega_{21}$ from each other. A monochromatic light field with the oscillation frequency $\omega_l aser$ is allowed to interact with this two-level atom.
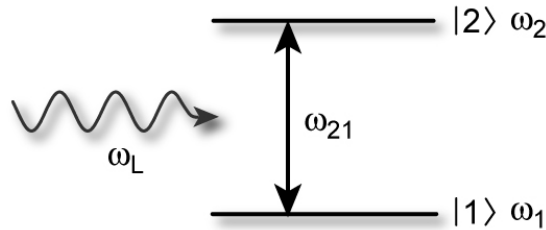

Figure 1.2: For the atom-light interaction we reduce the atom to two states, which interacts with a light field of frequency $\omega_L/2\pi$. For a majority of cases this is a good approximation if a near resonance interaction is present, i.e. $\omega_{21} \approx \omega_L$, because coupling between other energy states can be neglected due to of the large detuning. For the ionization this assumption is valid for the XUV, but not strong-field IR, experiments.

1.2.1 The atom-light-interaction operator

For a particle with a dipole moment in an external electric field, an interaction energy of $V = -\vec{d} \cdot \vec{E}$ is valid. In our case the external electric field is not static, but it is rather described by the oscillating electric field $\vec{E}(\vec{r}, t)$ of a light field.

In the case considered here, the wavelength of light in the visible range is much larger than the size of a single atom. The spatial variation of the electric field across the atom can be neglected and therefore we can in first-order approximation evaluate the electric field at the location $\vec{R}$ of the atom:

$$E(\vec{r}, t) \sim E(\vec{R}, t) = \vec{E}(t) \tag{1.7}$$

In our further examination the atom does not change its position during the atom-light interaction. Because of this, the spatial dependence of the electric field on the coordinate
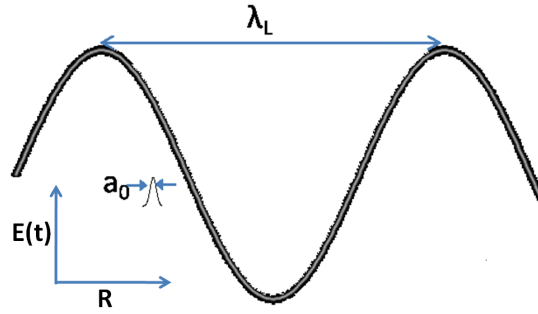
Figure 1.3: Electric dipole approximation. An atom at the position $\vec{R}$ has an extension of the electron cloud that is in the order of the Bohr radius a_0. This is dependent upon on the wavelength being 1.000 to 10.000 times smaller than that of the light field interacting with the atom. Therefore the electric field at the location of the atom is given, to a very good approximation, as $\vec{E}(\vec{r}, t) \approx \vec{E}(\vec{R}, t)$.

of the atom can be neglected. The oscillating electric field of a light beam can be described as:

$$\vec{E}(t) = \vec{\varepsilon} E_0 \cos(\omega_L t), \tag{1.8}$$

where $\vec{\varepsilon}$ stands for the to 1 normalized polarization vector, E_0 is the amplitude and ω_L the oscillation frequency of the light field.

Therefore the atom-light interaction operator, $\hat{V}$, can be written as:

$$\hat{V} = -\vec{d} \cdot \vec{E}(t) \tag{1.9}$$

with the electric dipole operator $\vec{d} = -e\vec{r}$.

1.2.2   Optical Bloch equation

The goal is to predict the temporal evolution of an arbitrary state vector in the two level atom under the influence of light. For this the time-dependent Schrödinger equation is applied:

$$i\hbar \frac{\partial}{\partial t} \psi(\vec{r}, t) = \hat{H} \psi(\vec{r}, t) = \left(\hat{H}_{at} + \hat{V} \right) \psi(\vec{r}, t) \tag{1.10}$$

We use the following ansatz for the wave function:

$$\psi(\vec{r}, t) = c_1(t) e^{-i\omega_1 t} u_1(\vec{r}) + c_2(t) e^{-i\omega_2 t} u_2(\vec{r}), \tag{1.11}$$

whereas $c_1(t)$ and $c_2(t)$ describe the time-dependent amplitudes of the two stationary eigenfunctions $u_1(\vec{r})$ and $u_2(\vec{r})$. The insertion of 1.11 in 1.10 and the formation of the scalar

product from the left with $e^{-i\omega_j t}u_j(\vec{r})$ delivers the two equations for the time-dependent coefficients $c_1(t)$ and $c_2(t)$

$$\begin{aligned}
\dot{c}_1(t) &= i\frac{d^{\varepsilon}_{21}E_0}{\hbar}e^{-i\omega_{21}t}\cos(\omega_L t)c_2(t) \\
\dot{c}_2(t) &= i\frac{d^{\varepsilon}_{21}E_0}{\hbar}e^{-i\omega_{21}t}\cos(\omega_L t)c_1(t).
\end{aligned} \tag{1.12}$$

Here $d^{\varepsilon}_{21} = \langle 2|\vec{d}|1\rangle \cdot \vec{\varepsilon} = \int u^*_2(\vec{r})\vec{d}u_1(\vec{r})\,d^3r \cdot \vec{\varepsilon}$ is the projection of the dipole matrix element onto the polarization vector.

The dipole matrix element $\vec{d}_{21} = \langle 2|\vec{d}|1\rangle$ determines the coupling strength of the transition. The transition probability will then be proportional to the coupling strength and the intensity. If the dipole matrix element is vanishing, the transition is forbidden.

If we are putting our atom now into a high intensity light field (intensity $I \approx 10^{12} - 10^{13}\text{W/cm}^2$) of IR radiation with $\omega_L \ll \omega_{21}$, the transition with one photon is not possible and we have to modify our model. Fabre *et al.* found the experimental ionization rates can be described very well with lowest order perturbation theory, as described above, with the absorption of n photons [100]. The ionization rate ω_n follows the power law according to:

$$\omega_n = \sigma_n I^n. \tag{1.13}$$

This law has been reviewed and could be approved for low intensities. Unfortunately the power law loses its validity if the assumption for the population of the initial state can not be neglected anymore. This means that the initial state is depleted and therefore the yield saturates. Additionally, intensity dependent corrections of ω_n are necessary if the states of the atom are Stark shifted in the electric field of the laser [101]. If the intensities are higher than 10^{13} W/cm^2, perturbation theory can not be applied anymore and other theories have to be applied (see section 7.1.1.2).

1.2.3 Selection rules

Not all energetically possible transitions are valid and some are more likely to occur than others. This section addresses the question of which transitions are possible and will occur and therefore have to be treated in the simulation of the ionization events.

1.2.3.1 Selection rules for optical dipole transitions

If an atom-light interaction occurs, for the dipole transition the following conditions have to be fulfilled:

$$\vec{d}_{21} \cdot \vec{\varepsilon} \neq 0 \Leftrightarrow \langle 2|\vec{d}|1\rangle \cdot \vec{\varepsilon} \neq 0 \Leftrightarrow \langle 2|\vec{r} \cdot \vec{\varepsilon}|1\rangle \neq 0 \tag{1.14}$$

First of all, the dipole matrix element may not disappear, i.e. $\vec{d}_{21} \neq 0$. Additionally 1.14 means that the projection of the dipole matrix element on the polarization vector $\vec{\varepsilon}$ of the light field is not allowed to vanish. If these conditions are fulfilled a transition is possible.

In general we are able to expand an arbitrary polarization state of a light field in basis vectors. For our purposes the following basis vectors lend themselves to usage:

basis vector	notation	remark
$\hat{\varepsilon}_1 = -\frac{1}{\sqrt{2}}(\hat{x} + i\hat{y})$	σ^+ polarization	circular, right turning
$\hat{\varepsilon}_0 = \hat{z}$	π polarization	linear
$\hat{\varepsilon}_{-1} = \frac{1}{\sqrt{2}}(\hat{x} - i\hat{y})$	σ^- polarization	circular, left turning

For a closer analysis of 1.14 we take a look at $\vec{r} \cdot \vec{\varepsilon}$:

$$r_1 = \vec{r} \cdot \vec{\varepsilon}_1 = -\frac{1}{\sqrt{2}}(x + iy) = -\frac{1}{\sqrt{2}} r \sin\theta e^{i\varphi} = r\left(\frac{4\pi}{3}\right)^{\frac{1}{2}} Y_{1,1}(\varphi, \theta),$$

$$r_0 = z = r\cos\theta = r\left(\frac{4\pi}{3}\right)^{\frac{1}{2}} Y_{1,0}(\varphi, \theta), \tag{1.15}$$

$$r_{-1} = \vec{r} \cdot \vec{\varepsilon}_{-1} = -\frac{1}{\sqrt{2}}(x - iy) = \frac{1}{\sqrt{2}} r \sin\theta e^{-i\varphi} = r\left(\frac{4\pi}{3}\right)^{\frac{1}{2}} Y_{1,-1}(\varphi, \theta).$$

For the projection of the dipole matrix element from equation 1.14 we deduce:

$$\vec{\varepsilon} \cdot \vec{d}_{21} = e \sum_{q=0,\pm1} \vec{\varepsilon}_q^*(\vec{r}_{21})_q \qquad \text{with } (\vec{r}_{21})_q = \hat{\varepsilon}_q \cdot \vec{r}_{21} \text{ and } \vec{\varepsilon}_q = \hat{\varepsilon}_q \cdot \vec{\varepsilon} \tag{1.16}$$

if one considers the quantum states $|1\rangle$ and $|2\rangle$ to be two states $|n, l, m\rangle$ and $|n', l', m'\rangle$ of a hydrogen like atom. For $(\vec{r}_{21})_q$ together with 1.15 it results:

$$(\vec{r}_{n'l'm',nlm})_q = \left(\frac{4\pi}{3}\right)^{\frac{1}{2}} \int_0^\infty dr \, r^3 R_{n'l'}(r) R_{nl}(r) \times \int d\Omega \, Y_{l'm'}^*(\varphi, \theta) Y_{1,q}(\varphi, \theta) Y_{lm}(\varphi, \theta). \tag{1.17}$$

The radial part in equation 1.17 is always larger than zero and in the dimension of the Bohr radius $a_0 = 5,3 \cdot 10^{-11}$ m. The angular dependent fraction of the integral can be written with the Clebsch-Gordan coefficients as:

$$\int d\Omega \, Y_{l'm'}^*(\varphi, \theta) Y_{1,q}(\varphi, \theta) Y_{lm}(\varphi, \theta) = \left(\frac{3}{4\pi} \frac{2l+1}{2l'+1}\right)^{\frac{1}{2}} \langle l100|l'0\rangle \langle l1mq|l'm'\rangle. \tag{1.18}$$

The last Clebsch-Gordan coefficient $\langle l1mq|l'm'\rangle$ is only unequal to zero if:

These selection rules also have a descriptive meaning. For example circularly polarized σ^+ light with $q = +1$ has to be used for a transition of $m' = m + 1$. This is easy to see, because a superposition of m and $m + 1$ states inherits a rotating charge distribution around the z axis with a positive rotation direction. Such a rotating charge distribution can only be excited by a positive circular polarized light field.

$$\boxed{\begin{aligned} m + q = m', &\quad \Delta m = 0, \pm 1, \\ l' = l \pm 1, &\quad \Delta l = \pm 1, \end{aligned}}$$

1.2.3.2 Selection rules concerning the parity of the states

On the basis of the parity of the dipole matrix element involved wave functions and operators, among other things one can determine if the matrix element vanishes or not.

The parity operator, $\hat{P}$, results in an inversion at the origin. Due to the commutation of the parity operator with the atomic Hamiltonian, the eigenstates of the hydrogen atom are also eigenstates of the parity operator with eigenvalues of ± 1.

The position operator $\vec{r}$ of the electron transforms under the parity operator in the following way:

$$\hat{P}^{-1}\vec{r}\hat{P} = -\vec{r}. \tag{1.19}$$

For the wave function of the hydrogen atom it is imperative that:

$$\hat{P}R_{nl}(r)Y_{lm}(\varphi, \theta) = (-1)^{l}R_{nl}(r)Y_{lm}(\varphi, \theta). \tag{1.20}$$

The parity of the hydrogen wave function is accordingly either +1 (gerade) or -1 (ungerade) depending on if l is even or uneven.

The dipole matrix element between two hydrogen-like states can then be written as:

$$\begin{aligned} \langle n'l'm'|\vec{r}|nlm\rangle &= \langle n'l'm'|\hat{P}\hat{P}^{-1}\vec{r}\hat{P}\hat{P}^{-1}|nlm\rangle \\ &= (-1)^{l+l'+1}\langle n'l'm'|\vec{r}|nlm\rangle. \end{aligned} \tag{1.21}$$

If $l + l' + 1$ is uneven, equation 1.21 can only be fulfilled if the dipole matrix element is zero. From this we draw the conclusion, that the dipole operator is only connecting quantum states with different parities.

1.3 Molecular physics concepts

This section covers only a few of the most relevant concepts necessary for the understanding of the data presented in this thesis.

1.3.1 Potential energy curves

Due to the large number of possible configurations of its constituent particles (nuclei and electrons), the representation of a molecule can be complicated. One way of presenting a simple diatomic molecular system is a potential energy curve diagram. Figure 1.4 shows an example of such a diagram for doubly charged O_2.The x axis is the internuclear distance and the y axis presents the potential energy.

Figure 1.4 shows that despite the large numbers of states and shapes of the potential curves, they dissociate into a relatively small number of final states.
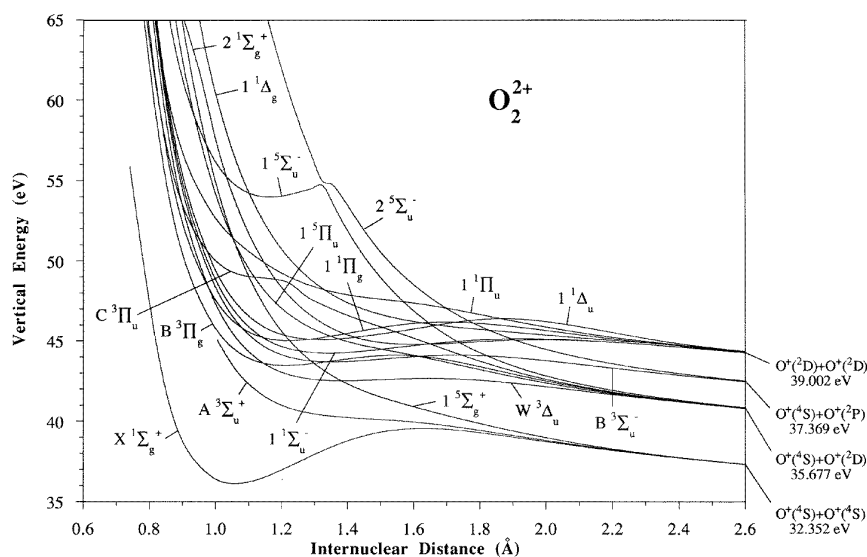
Figure 1.4: Molecular potential energy curves of the doubly charged oxygen molecule [102].

Other important characteristics are the shapes of the potential energy curves. Some like the $X^1\Sigma_g^+$ show a clear potential well indicating that the molecule is bound. Others show no well at all, indicating that these are dissociating states of the molecule. This means that after those particular potential energy curves are populated, the molecules will split into two separated particles.

The specific shape of the potential energy curves at small internuclear distances (>5 Å) is mainly determined by the molecular electron wave function interacting with the nuclei (i.e.: the particular molecular electron orbital). At large internuclear distances (also called the dissociation limit), the potential energy curves will group into a finite number of possibilities governed by the atomic states of the dissociation fragments. An example for O_2^{2+} is given in figure 1.4.

1.3.2   Franck-Condon principle

The Franck-Condon principle can be described both classically and quantum mechanically. The IUPAC Compendium of Chemical Terminology [103] refers to the Franck-Condon principle as:

"Classically, the Franck-Condon principle is the approximation that an electronic transition is most likely to occur without changes in the positions of the nuclei in the molecular entity and its environment. The resulting state is called a Franck-Condon state, and the transition involved a vertical transition. The quantum mechanical formulation of this principle is that the intensity of a vibronic transition is proportional to the square of the overlap integral between the vibrational wave functions of the two states that are involved in the transition."

For the purpose of analysis in this thesis, the important aspect of this principle is all

transitions between potential energy curves will happen at fixed internuclear distances. The target in the interaction region consists of a supersonic cold molecular gas jet and because of this the molecules can assumed to be in their neutral ground states before interaction with the laser pulses. The width of the ground state wave function determines the range of internuclear distances over which the upper states of the molecules can be populated by the first photon interaction. This corresponds to the region between the vertical dashed lines in figure 5.1 and is called the Franck-Condon region.

1.3.3 Molecular structure

The study of molecular structure is a very complex field. Various theories such as the valence-bond theory and the molecular orbital theory try to explain the chemical bonds formed in nature. Because the molecules studied here are diatomic (homonuclear for D_2, N_2 and O_2 and heteronuclear for NO and CO), determining the molecular orbital structure is a little easier. Many textbooks [103, 104] cover the subject of molecular structure. This text will only give a quick review of some of the terminology and definitions.

Similar to atomic orbitals which are labeled s, p, d, and so on, molecular orbitals are labeled by the Greek equivalent σ, π, δ, etc. Just as the atomic states are labeled by the capitalized version of the orbitals (S, P, D, etc.), the molecular states are also designated by their capitalized Greek letters (Σ, Π, Δ, etc.). Molecular orbitals can be thought of as the linear combination of the atomic orbitals of the valence shell of the constituent atoms. For diatomic molecules, σ orbitals can be built from s and p_z atomic orbitals and have cylindrical symmetry around the internuclear axis. On the other hand, π orbitals can be built from p_x and p_y atomic orbitals. The coupling strength between atomic orbitals when forming a molecular orbital is determined by an integral of the electron wave function overlap:

$$S = \int \psi_1^*(r)\psi_2(r)dr^3 \tag{1.22}$$

where dr^3 is the volume element. This explains, for example, why an s orbital will not couple with a p_x orbital as their overlap integral is zero. Another important element is the concept of bonding and antibonding orbitals. A bonding orbital is defined as an orbital that, if occupied, helps to bind the two atoms together. For a diatomic molecule, an electron orbital whose wave function has a high probability density between the atoms is a bonding orbital. In contrast, an electron orbital whose wave function has a node between the atoms will cause that the nuclei are pushed apart and it is labeled an antibonding orbital.

One last notation element that can be seen in figure 1.4 has to do with parity. This concept is only important in homonuclear diatomic molecules and is concerned the with inversion symmetry of the electron wave function. If after inversion, the wave function has the same sign, the molecule is said to have even parity and the orbital is labeled "g" from the German word for even: *gerade*. If the wave function changes sign through the inversion, the molecular orbital is labeled "u" for *ungerade*.

Chapter 2

Experimental tools

The setups of the various experiments carried out forming the basis of this thesis are outlined over the course of this chapter. First the free electron laser (FEL) technology, which was used at FLASH (Free Electon LASer Hamburg) in Hamburg (Germany) and at SCSS (SPring8 Compact SASE Source) in Harima (Japan), is explained. Following this outline, the reaction microscope, which is the spectrometer used in these studies, is described followed by the split mirror setup that enabled us to perform XUV-XUV pump probe experiments. Finally, the instruments used for the IR experiments in Garching, Germany, the amplified Ti:saphire laser system with compression of the pulse with a hollow core fiber and the stereo ATI to enable single shot carrier-envelope phase measurements, are described.

2.1 The Free Electron Laser

Free electron lasers (FELs) were a revolution in the field of XUV-physics. With the newly built machines at DESY in Hamburg, Germany and at Spring8 in Harima, Japan photon fluxes and intensities were reachable that had, up to this point, not been possible to be reached with high harmonic generation (HHG) sources. Although synchrotrons also deliver a high photon flux, these are not suited for measurements with high temporal resolution due to their long pulses in the order of several tens of ps. FELs now give access to high intensity, up to 10^{16} W/cm^2 and short pulses in the region of as low as 20 fs. This chapter describes the basic principle of a FEL and gives insight into the differences between FLASH and SCSS.

2.1.1 Electron gun and linear accelerator (FLASH)

The required electrons are generated in the electron gun by a pulsed laser, which hits a Cs_2Te-photocathode. This device is situated in a superconducting radiofrequency (RF)-cavity that accelerates the generated electrons using a field strength of 40 MV/m, to relativistic speed. This strong acceleration makes it possible to avoid the electron bunch

to broaden due to space charge[2]. Subsequently, the process is continued with a linear accelerator consisting of five modules, each having a length of 12 m and composed of eight superconducting RF-cavities. These accelerate the electrons further up to an energy of 1 GeV. By choosing an appropriate phase of the high-frequency voltage, which is applied to the cavities, the width of the energy distribution can be reduced. Additionally, there are devices for bunch compression, respectively dispersion control, installed in between the accelerator modules. A detailed description of the electron gun, the accelerator and the associated beam-optics can be found in ref. [105].

2.1.2 Undulator

An undulator is a long periodical assembly of short dipole magnets of alternating polarity (see figure 2.1). This assembly leads to a transversal oscillation of passing electrons with a frequency depending on the undulator period λ_u. Taking the length contraction of the undulator period, caused by the relativistic movement, and the relativistic Doppler shift into account, the equation for the wavelength of the emitted radiation is:

$$\lambda = \frac{\lambda_u}{2\gamma^2}\left(1 + \frac{K^2}{2}\right),\tag{2.1}$$

containing the Lorentz factor γ and undulator parameter K, which is amongst other factors dependent on the gap between the magnetic poles (for more details see [106]).

Since a FEL obtains its special radiation properties from the energy exchange of the radiation field and the relativistic electron bunch, it has to be maximized. On the one hand, this leads to the demand of a preferably large interaction region between the electron beam and the field, i.e. a pointing that is as parallel as possible. On the other hand, the energy transfer is proportional to the scalar product between the velocity vector of the electrons and the field vector of the radiation field

$$\frac{dE_e}{dt} = -e\vec{v}_e \cdot \vec{E}.\tag{2.2}$$

The energy conversion vanishes for all other directions than the transversal component of the velocity vector v_e. Electrons are massive particles and due to the sine-like trajectory, forced by the undulator, do not move along a straight line. As a result of that, a phase shift between the electrons and the radiation field is induced. A phase shift per period is called slip. If the slip corresponds to a multiple of the undulator period, the phase between the transversal velocity of the electron bunch and the radiation field at the points of the maximum energy conversion remains constant and the energy transfer is optimized[3]. For

---

[2]At relativistic energies, the parallel electric currents induce attractive magnetic forces counteracting the Coulomb repulsion.

[3]Strictly speaking, the energy transfer in this case is zero, since exactly the same number of particles are gaining energy as dispersing energy. Hence, a wavelength marginally larger than the one given for the resonance condition in equation 2.1 is chosen. Second order effects can then be accounted for the energy transfer to the radiation field.

the phase condition for optimal energy transfer from the electron bunch to the radiation field also equation 2.1 is unfolding. (see ref. [106])
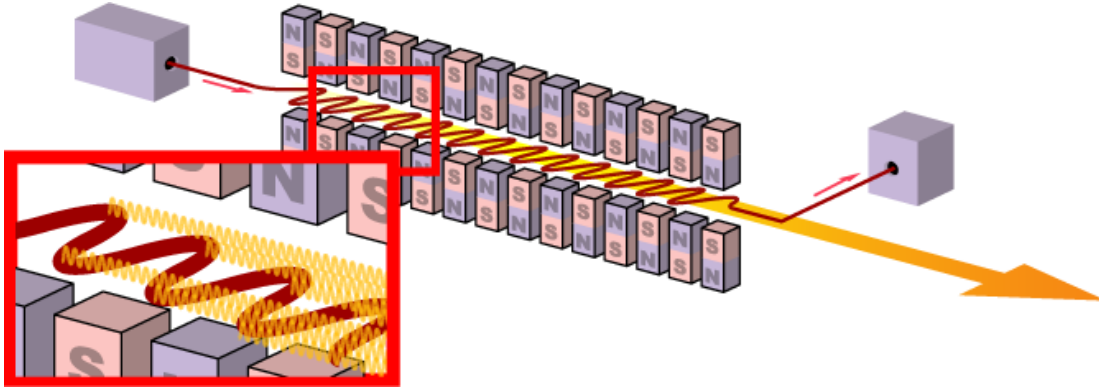

Figure 2.1: Schematic picture of the FEL with the undulator, which has a length of 30 m and a magnified picture showing the oscillation. The amplitude of the transversal oscillation is of the order of several microns. (Picture taken from Wikipedia)

2.1.3 The SASE mechanism

The basic principle for the self-amplified spontaneous emission (SASE) mechanism is that the intrinsic wavelength of the undulator radiation and the wavelength of the optimum of the energy transfer are equal. Unlike in an optical laser amplifier this is a desired effect in an undulator. This concept goes back to the work of J. Madey [107] and it describes the self amplification of spontaneously generated radiation in an undulator. By applying this concept so called single-pass-FELs became possible, which avoid two basic problems with the construction of earlier FELs. Firstly, there are no mirrors with a reflectivity in the XUV-region that is high enough. This is at least complicating if not circumventing the setup of a resonator. Secondly, there were no adequate light sources from which photons could act as seed for the continuing amplification[4]. Instead, the noise from the first part of the undulator is used as a seed, using the fact that only wavelengths are amplified, which are near the intrinsic wavelength of the undulator radiation. The resulting field is modulating the electron bunch in the course of the undulator in the longitudinal direction (see picture 2.2), because the electrons dispersing energy to the field are more deflected than those gaining energy. As a result of this, the electrons accumulate around the points in the electron bunch where the energy transfer in equation 2.2 is at its maximum. This density modulation in the longitudinal direction leads to an enhancement of the field, because the radiation fields of the single electrons do not interfere pairwise destructively as it would for a uniform spatial distribution. As a result of the increasing field, the compression of the electrons at the points of the maximum in the energy transfer becomes stronger. These

---

[4]For this purpose, nowadays high harmonics of optical lasers could be used, which had major improvements during the last years [108].

forming segments of the electron bunch are called micro bunches. This self-energizing effect leads to an exponential increase of the intensity until it saturates [109].
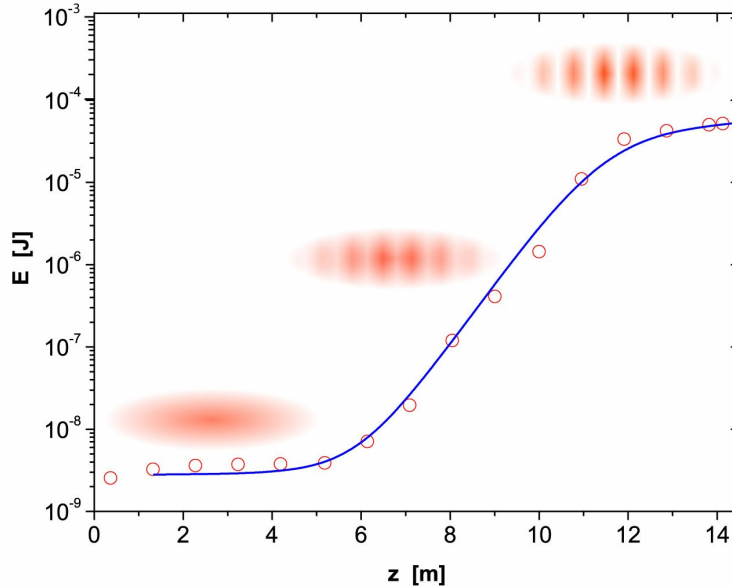

Figure 2.2: Formation of the spatial modulation as a function of the undulator length. The homogeneous electron packet enters the undulator, becomes modulated and reaches saturation. In reality there are typically several thousand charge maxima. (Pricture from [110])

If the latitude of the single micro bunches becomes smaller than the wavelength of the emitted radiation, then they act as a single radiating particle with a multiple electrical charge. This is the reason why in the formula for the emitted power, due to this spatially coherent radiation, the number of the electrons of the micro bunch, N_e, can be found as an additional factor,

$$P_\gamma\left(N_e\right) \propto N_e e^2 \gamma^4 \dot{v}_t^2 \longrightarrow P_\gamma\left(N_e\right) \propto \left(N_e e\right)^2 \gamma^4 \dot{v}_t^2 = N_e^2 e^2 \gamma^4 \dot{v}_t^2 \tag{2.3}$$

where $\dot{v}_t$ is the transversal speed of the electrons caused by the undulator. Another significant parameter is the gain length L_G of the undulator. Therefore the length in which the intensity rises by the factor e is:

$$L_G = \frac{\lambda_u}{2\sqrt{3}\pi\rho}, \tag{2.4}$$

with the FEL-parameter $\rho \propto \frac{\sqrt[3]{n_e}}{\gamma}$, with dependencies on the particle density of the electron bunch, n_e, and the Lorentz factor, γ. To achieve the shortest possible gain length and therefore undulator length at a given particle energy, large particle densities and respectively current densities on the order of several thousand ampere per bunch, are required.

At the same time, the overlap between the radiation field and the electron bunch has to be sufficiently even, meaning that the beam emittance may not be too large, also for large particle energies and a long undulator. If the overlap is not sufficiently even, the energy transfer would be insufficient. Additionally, to reach the point of saturation, the energy spread of the electron beam has to be very low, in the region of 0.01% [111]. These conditions (derivation see [109]) can currently, for wavelengths in the XUV region, only be fulfilled by a linear accelerator.

2.1.4 Comparison FLASH - SCSS
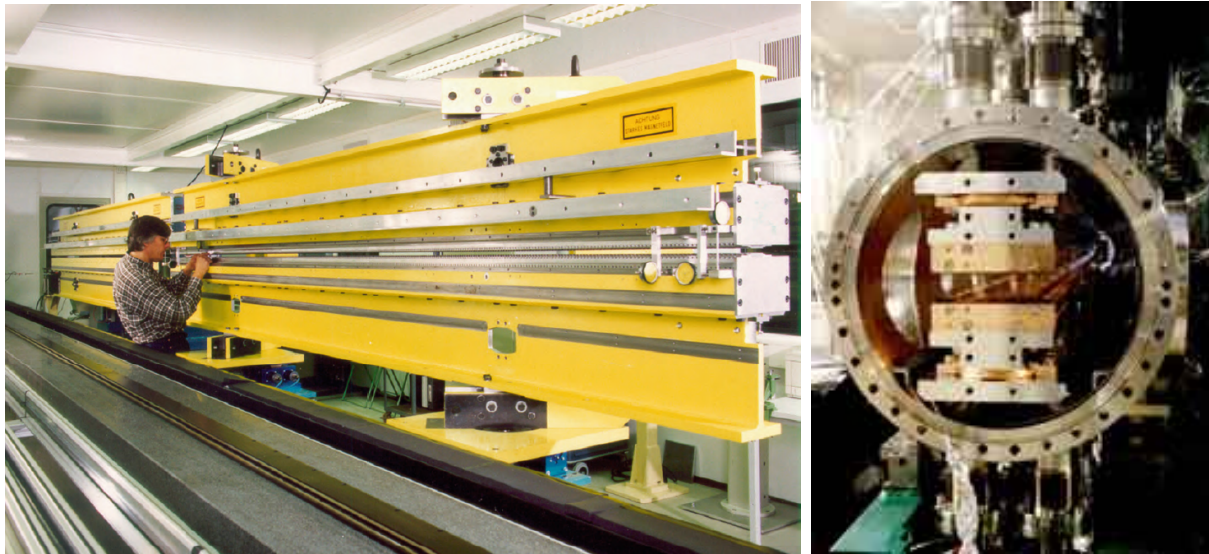
(a) Undulator FLASH (b) In-vacuum undulator SCSS

Figure 2.3: Undulators of FLASH (a) and SCSS (b). SCSS has an "in-vacuum undulator" that allows a band gap of 3.7 mm and an undulator period of 15 mm to be produced. The undulator of FLASH has a gap of 12 mm and a period of 27 mm. The shorter period allows a lower electron beam energy for the same wavelength. Pictures taken from [110, 112].

The main difference between FLASH and SCSS lies in the compactness of the later one. Whereas SCSS is shorter than 100 m, FLASH has a total length of 315 m. To achieve this at SCSS a low emittance beam injector is used consisting of a single crystal thermionic cathode. This has the advantages of requiring less maintenance than a laser driven cathode and with significantly lower emission, the collimation much easier. The electron accelerator is also different. While the superconducting accelerator at FLASH is working in the L-band at a frequency of 1.3 GHz, a new accelerator scheme in the C-band with a frequency of 5.7 GHz is used at SCSS. The four-fold acceleration frequency results in a gradient of 35 MV/m at SCSS in comparison to 20 MV/m at FLASH despite the super-conduction. Another difference that contributes to the shortness of SCSS, is the in-vacuum undulator

which is more compact than the undulator used at FLASH (see fig. 2.3). This leads to a smaller undulator gap of 3.7 mm at SCSS in comparison to 12 mm at FLASH. As a result an undulator period of 15 mm can be realized, whereas at FLASH it is 27 mm, this results in a shorter wavelength at the given electron energy and less electron energy to achieve a given photon energy. For further reading please refer to [110, 113].

	FLASH	SCSS
Wavelength [nm]	6.8 - 47	50 / 61
Pulse energy [μJ]	10 - 100	10
Bandwith [%]	1	1

2.2   The Reaction Microscope

Reaction microscopes can be used to perform kinematically complete experiments. That means that it is possible to measure the momentum components of all particles involved in the collision process in their final state. In the past years, the method was successfully used in numerous experiments, including studies of electron collision ionization, ionization and capture processes in atom ion collisions, single photon ionization and multi-photon strong field ionization and it turned out to be a reliable technique (for reviews see [81, 114, 115]).

A reaction microscope consists of the combination of a COLTRIMS (COLd Target Recoil Ion Momentum Spectrometer), which is used to determine the momentum of the ionized target and an electron spectrometer, that offers the possibility to measure the momentum of one or several low energetic electrons over a solid angle of 4π.
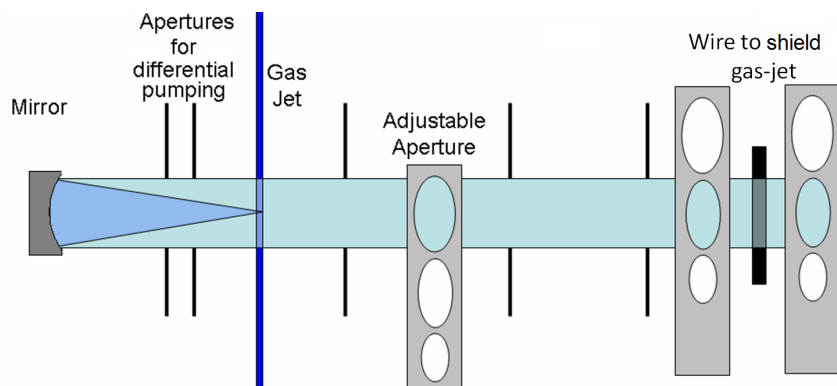
Figure 2.4: Schematic illustration of the setup used at FLASH. The adjustable apertures are used to cut the beam and to block stray light. The wire is applied to put a shadow on the jet in order to ionize only with the focused beam. The spherical split mirror is required to focus the FEL beam into the jet and to split the pulse in two equal parts to introduce a delay between them. In addition, a variety of apertures are inserted for differential pumping.

In the following chapter, a short introduction of the generation of the target, the mode

of operation of the spectrometer and the detector system is given. A detailed description of the techniques used can be found in [81–84].

2.2.1 Design and mode of operation

2.2.1.1 The gas target

To perform high resolution momentum spectroscopy a cold target is a precondition as the maximum resolution achievable is limited by the thermal momentum distribution of the target molecules. The momenta of the measured target fragments are in the region of a few atomic units (1 a.u. $= 1.995 \cdot 10^{-24}$ kg m/s, see appendix 8). If one wants to measure for example a helium atom with a momentum resolution of 0.1 a.u., than the kinetic energy has to be determined with a resolution of 0.02 meV, which corresponds to a target temperature of 150 mK. For comparison, the momentum of oxygen molecules in the jet is more than 13 a.u.. An additional technical precondition for experiments of this kind is a target beam that is well localized and colliminated. One reason for that is that the ultrahigh-vacuum (UHV) in the reaction chamber must not be affected by the target beam to avoid residual gas leading to background in the measurement. Another reason is that a large overlap between the laser and the target beam would lead to a large reaction volume, which would lead to more focal intensity averaging on the one hand and affect the maximum momentum resolution on the other (see ref. [116]). A supersonic gas jet, as it is used in a reaction microscope, fulfills these conditions. The functional principle of such a gas jet is based on a supersonic expansion in which the target gas flows from a reservoir with the backing pressure, p_0, through a small nozzle into an expansion chamber under lower pressure, p_{exp}. When the ratio p_0/p_{exp} is smaller than two (details see [117]), the gas will expand adiabatically behind the nozzle into the first differential pumping stage and a region with a length of a few centimeters is being formed, where the atoms are faster than the local speed of sound. This area is called the *zone-of-silence*. In the ideal case, which can only be fulfilled by rare gases, the free enthalpy $H = 5/2k_BT_0$ (k_B the Bolzmann constant and T_0 the temperature of the gas before the expansion), which is the sum of the thermal energy and the work that is stored in the gas pressure per atom, becomes completely transformed into directed kinetic energy. That way, the momentum of a target particle of the mass, m, is:

$$p_{jet} = \sqrt{5k_BT_0m}. \tag{2.5}$$

These ideal conditions cannot be reached in reality, because the particles of the gas can scatter among each other and with the residual gas. The achievable temperature, T, of the expanding gas is defined by the speed ratio

$$S = \frac{v_{jet}}{v_{therm}} = \sqrt{\frac{5T_0}{2T}}, \tag{2.6}$$

thus the ratio between the directed velocity, v_{jet}, and the thermal velocity, v_{therm}, of the gas jet. The speed ratio is dependent on the used gas, the temperature before the expansion,

and the product $d \cdot p_0$ between the diameter of the nozzle and the backing pressure. When using a helium jet with a nozzle diameter of $d = 30 \mu m$ and a backing pressure of $p_0 = 15 bar$, a speed ratio of $S \approx 30$ results (see [117]). If the gas has a temperature of $T_0 = 300 \mathrm{K}$ before the expansion, the resulting target temperature is, according to equation 2.6, $T = 0.83 \, \mathrm{K}$ corresponding to a momentum spread of $\delta P \approx 0.24 \, \mathrm{a.u.}$.

To realize a cold, well localized target from the expanding gas, a particle beam is clipped out of the zone of silence by a cone-like aperture with a sharp edge, the *skimmer* (see figure 2.5). For this work a differential pumping stage with a second skimmer, which is pumped separately, is located between the expansion and the reaction chamber. Thereby it is guaranteed that the vacuum in the reaction chamber does not become perturbed by the operation of the jet. When the jet is operating, the pressure in the expansion chamber is $p_{exp} \approx 10^{-3} \, \mathrm{mbar}$. In the second stage the pressure is between 10^{-6} and $10^{-5} \, \mathrm{mbar}$ and in the reaction chamber it is between 10^{-12} and $10^{-9} \, \mathrm{mbar}$. After passing the reaction chamber, the jet is terminated in an additional differential pumping stage. The pressure in the reaction chamber corresponds to a particle density of 10^7 to 10^4 per cubic centimeter when the jet is used. At a pressure of 1 bar it is $2.7 \cdot 10^{19}$ per cubic centimeter.
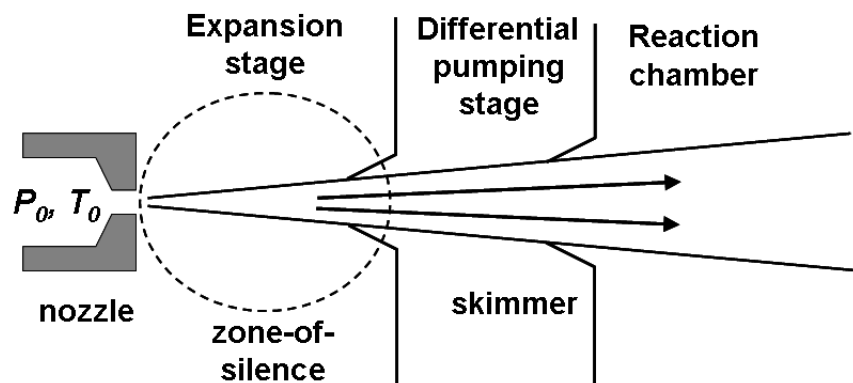

Figure 2.5: Design of a supersonic gas jet. For further information, see text.

By using the skimmers, the temperature of the jet is reduced additionally, because particles with a larger transversal momentum are suppressed. The momentum distribution of the target is then determined by the geometry and the velocity of the jet. With a distance of 3 cm between the nozzle and the second skimmer, a skimmer diameter of 0.6 mm and a directional momentum of 5.9 a.u. are given for helium (from equation 2.5), the momentum width perpendicular to the beam is $\Delta P \approx 0.12 \, \mathrm{a.u.}$.

In principle, even lower temperatures are accessible with this technique if the target gas is pre-cooled in the reservoir prior to the expansion. This approach of pre-cooling was used at specific experiments that were performed at FLASH and at SCSS.

2.2.1.2   The Spectrometer

The purpose of the spectrometer of the reaction microscope is to guide the ions and electrons onto the detectors in a way that allows the momenta to be determined. The design and the mode of operation of such a spectrometer is illustrated in figure 2.6. In the middle of the spectrometer the target beam and the projectile beam, in our case either an IR laser or an XUV beam from a FEL, cross over and the charged target fragments are produced. These fragments, electrons and ions, carry information about the reaction in form of their momenta. Along the spectrometer axis coaxial arranged metal rings that are connected by a chain of resistors, which when voltage is applied, generate a homogeneous electric field. This field accelerates the fragments accordingly to their charge to the ion or electron detector. By using the point of incidence and the time-of-flight from the point of the interaction to the detector the tree momentum vector components can be calculated (details see section 2.2.2). For the determination of the time-of-flight a trigger signal is required, which is associated with the time of the interaction. In the experiments that are described here either an IR photodiode detecting a reflection from a pair of glass wedges, or the voltage signal that occurs when an intense XUV pulse hits a dielectric mirror are used as the trigger signal.

In case of the ions, the dependence of the time-of-flight on the mass charge ratio of the particle can be used to separate the ion species. For this it is necessary that the time-of-flight of the ion species differ significantly. This is equivalent with the usually very well fulfilled precondition that the energy, ions gain in the electric field, is larger than the energy they obtain from the reaction itself. Furthermore, the solid angle detected depends only on the acceleration voltage and the size of the detector.
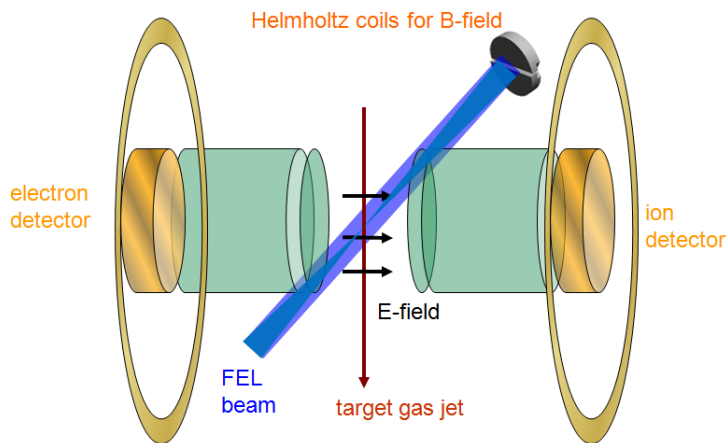

Figure 2.6: Schematic layout of a reaction microscope. The spectrometer is illustrated in green. The reaction volume has a relevant extension only in the direction of y due to the small focus of the laser of approximately 15 μm, which is determined by the jet diameter of up to 1 mm.

For the measurement of the electrons the electric field itself would lead to a "rather

low" solid angle acceptance, except if the acceleration voltage needed would be so high that the momentum resolution of the ions would suffer (see section 2.2.3). Therefore the electric field is superimposed with a weak magnetic field (order of magnitude 10 Gauss) produced by a pair of Helmholtz coils, which forces the electrons on a helix shaped trajectory, to assure that all of the electrons, up to a given transversal energy, hit the detector. Due to the much higher mass of the ions they are only mildly affected by the magnetic field.

To compensate the effect of an expanded interaction zone on the momentum resolution, usually a field free drift zone follows the acceleration part [116]. The length of the drift zone is defined by the temporary focusing condition [116]. Because a tightly focused laser was used for these experiments, such a drift zone was not necessary and was therefore omitted.

2.2.1.3   The detector system

To measure the time-of-flight as well as the position where the charged particle hits the detector a micro channel plate (MCP) with a delay line anode was used. A MCP consists of a glass plate with a thickness of approximately 1 mm. This glass panel is perforated by capillaries with a diameter of 10 - 100 μm. The front and reverse of the panel is coated with a well conducting material, so that two equipotential surfaces are formed. Between these two surfaces a high voltage of several kV is applied. The primary particle hitting the MCP releases secondary electrons that are subsequently accelerated by the field and in turn trigger secondary electrons. The electron cloud leaving the capillary is still spatially and temporarily constricted, which gives rise to a good temporal and spatial resolution.

The capillaries are slightly tilted against the surface normal (see figure 2.7). This serves two purposes. Firstly the electron will hit the wall of the capillary more easily to produce secondary electrons if it is not parallel to the acceleration direction. Secondly ions which become accelerated in the other direction due to the different sign of their charge, will hit the capillary surface after a short acceleration length and are not able to knock out other ions. Additionally these are not able to exit the channel plate towards the spectrometer. The described ions are produced by rest gas ionization by electrons. At this exact point in time, t_{MCP}, when the multiplicated electrons leave the MCP, a voltage drop can be measured via the decoupling electronics at the channel plate. By using this time and the time of the trigger signal, $t_{trigger}$, (see section 2.2.1.2) the time-of-flight, t_{ToF}, of the primary particle hitting the MCP can be calculated:

$$t_{ToF} = t_{MCP} - t_{trigger}. \tag{2.7}$$

To retrieve were the primary particle hits the MCP, the exit point of the electron cloud is determined. This is done by using a delay line anode, which consists of long wires that are wound around a ceramics holder. In these wires a voltage signal is induced by the passing electrons. This signal then travels from the point of origin to the ends of the wire, were it is read out. For each direction there are always two sets of wires which are wrapped in a way that does not allow that they have contact and they are also isolated against earth. Between these wires a small voltage is applied, which results in the fact that

one wire attracts the electrons more than the other. The second wire serves as a reference, which allows the suppression of the intrinsic noise of the voltage measurement by using the differential signal.
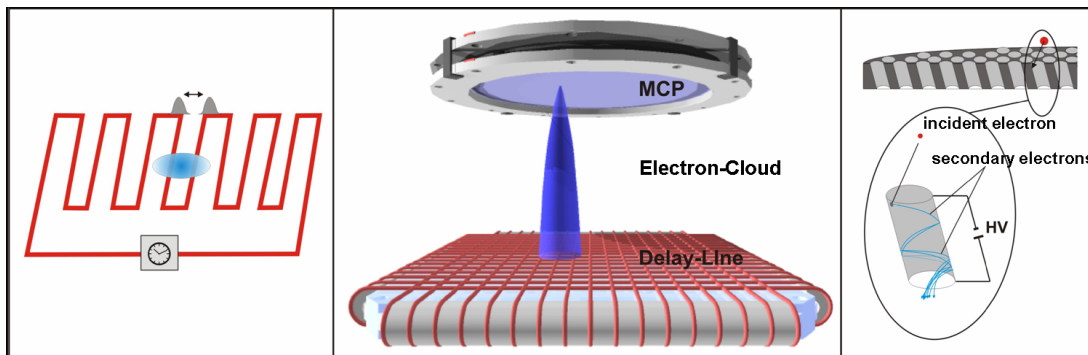

Figure 2.7: Schematic diagram of the mode of operation of the detector. Right: Multiplication of an incident particle in a capillary of the channel plate. Middle: The emerging electron cloud initiates a voltage signal in the delay-line anode, which spreads to both ends of the wire. Left: The composition of the arrival times results in the spatial information. From [118]

Due to the fact that the propagation velocity in the wire is constant, the difference between the arrival times of the two signals at the ends of each wire can be used to calculate the coordinate of the electron cloud's point of impact:

$$x \propto (t_{x1} - t_{MCP}) - (t_{x2} - t_{MCP}). \tag{2.8}$$

Here t_{x1} and t_{x2} stand for the arrival times of the voltage signal at the two ends of the wire in x direction. The calculation of the y coordinate is done correspondingly. The conversion of the coordinate from a time into a spatial scale is carried out by a constant factor. This factor can be calculated using the size of the detector and the time the signal needs to propagate through the complete wire.

If the temporal distance between two incident particles is longer than the time the signals need in order to reach to the ends of the wires, the location and the time of incidence can be determined. If the delay between two events is shorter than this, then it is likely that two errors may have occurred. Either, the delay line signals of different particles arrive at the ends of the wires in an alternating order, or two signals of different particles can be so close together time-wise, that they cannot be separated by the data acquisition system. To determine the correct time-of-flight and location of incidence, the five signals (one MCP and four delay line signals) belonging together have to be found. For this, we can draw on the fact that the sum of the time the signals need to reach the end of the wires in the delay line is always the same. For the x direction it can be asserted the following way:

$$t_{sum} = (t_{x1} - t_{MCP}) + (t_{x2} - t_{MCP}) = const. \tag{2.9}$$

Based on a MCP signal, the corresponding delay line signals can be found by checking the time sum. The goal of this procedure is to prevent false assignments and therefore every signal is only used once. If the signals of two or more particles cannot be separated, then for only for one of these all required signals can be found. The other particle is considered lost.

2.2.2 Computation of the momenta

In addition to the measured spatial information and the time-of-flight, the precise dimensions of the spectrometer, the voltage applied to the spectrometer and for the electrons the strength of the magnetic field are needed to reconstruct the momenta of the fragments. The formulas needed for a spectrometer without a drift zone are presented in this section. They are separated in formulas for ions and electrons and for longitudinal (along the spectrometer axis) and transversal (perpendicular to the spectrometer axis) momentum components. For a spectrometer with a drift zone the reader may refer to [116].

2.2.2.1 Ions longitudinal

An ion which is produced in the interaction point gains a momentum $p_\parallel$ and therefore an energy $E_\parallel = p^2/2m$ by the reaction. The electric field is applied in direction of the time-of-flight and leads to an acceleration in the longitudinal direction. When the coordinate system is chosen as in illustration 2.6 the spectrometer axis is along the z axis and the ion is born at the origin. The acceleration is:

$$\ddot{z} = \frac{qU}{ma},\tag{2.10}$$

where a is the length of the acceleration and U stands for the potential between the interaction point and the end of the acceleration. Integrating twice with respect to time results in position $z(t)$. If now $z(t)$ is replaced with the end of the acceleration, it follows from the above for the time-of-flight of an ion from the interaction point to the detector:

$$t_{+/-}\left(E_\parallel\right) = f \cdot \sqrt{m} \cdot \frac{2a}{\sqrt{E_\parallel + qU} \pm \sqrt{E_\parallel}} \qquad \text{with } f = 791.9 \frac{\text{ns}}{\text{cm}}\sqrt{\frac{\text{eV}}{\text{amu}}},\tag{2.11}$$

where the "+" stands for ions that are flying after the initial reaction towards the detector and the "-" correspondingly for ions that are flying away. The constant factor f originates from the transformation of the units and it is chosen so the mass m of the ion is inserted in atomic mass units (1 amu $= \frac{1}{12}m^{12}C$). Accordingly the energies $E_\parallel$ and qU in eV and the acceleration length a have to be given in cm.

It is a good approximation that the energy that is gained in the electric field qU is much larger than the primary energy $E_\parallel$, because of this, the time-of-flight can be developed in

a Taylor series around $E_\parallel$. This way, the time difference to ions with $E_\parallel = 0$ can be approximated as:

$$\Delta t = t\left(E_\parallel\right) - t\left(E_\parallel = 0\right) \approx \left[\frac{dt\left(E_\parallel\right)}{dE_\parallel} \cdot \frac{dE_\parallel}{dp_\parallel}\right]_{p_\parallel=0} \cdot p_\parallel. \tag{2.12}$$

With the help of equation 2.11 for the longitudinal momentum in atomic units it is unfolding (see [115]):

$$p_\parallel = \left(8.04 \cdot 10^{-3} \frac{a.u. \cdot cm}{eV \cdot ns}\right) \cdot \frac{qU}{a} \cdot \Delta t. \tag{2.13}$$

By means of this equation the advantage of the previous analysis is clear. For the calculation of the longitudinal momentum $p_\parallel$ only the time difference between ions carrying momentum and ions with longitudinal momentum $p_\parallel = 0$ is needed, which can be easily obtained from the mean value of the temporal distribution for the corresponding ion species (for example see fig. 2.8 for the example O^+ ions from O_2). The low accuracy in the absolute measurement of the time does not affect the achievable resolution. The low accuracy comes from the fact that the run time of the signals and their delay in the electronic modules are not exactly known.
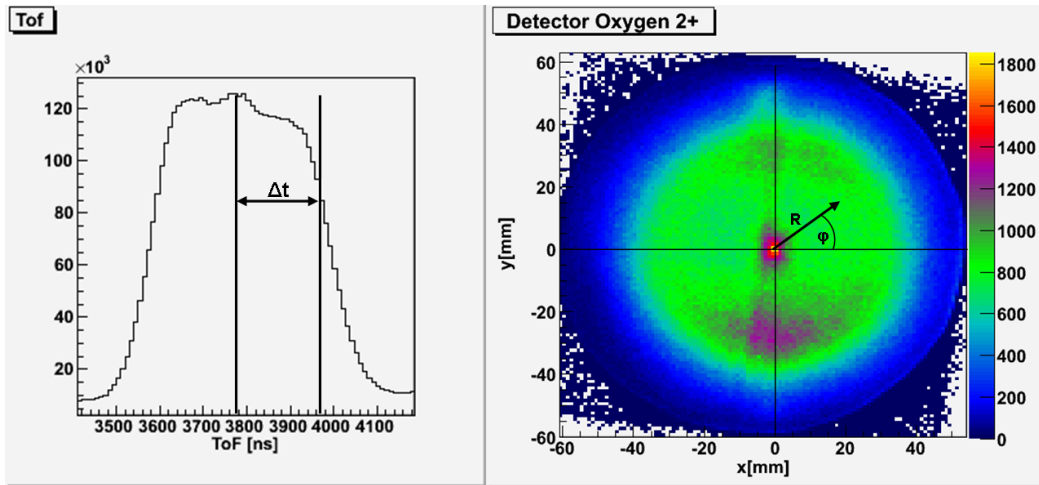
Figure 2.8: Left: Time of flight spectrum of O^+ ions. Illustrated is the evaluation of the time difference Δt which is needed for the determination of the momentum along the time-of-flight axis. The time-of-flight axis (3500-4100 ns) displayed does not correspond to the absolute time-of-flight but to the time relative to the last trigger from the FEL bunch. Right: spatial picture of the O^+ ions, where the plotted parameters R and φ correspond to the computation of the momenta.

2.2.2.2   Ions transversal

In the transversal direction there is no acceleration. Therefore, the traveled distance in this direction with respect to the reaction point is depending on the original energy in transversal direction $E_\perp$ and the time-of-flight to the detector. Due to symmetry reasons the image of the reaction point coincides with the center of mass of the distribution on the detector. The distance R to the center of the distribution in the detector plane results from:

$$R = \frac{1}{f} \cdot \frac{\sqrt{E_\perp}}{M} \cdot t_{tof}. \tag{2.14}$$

If in equation 2.14 the absolute time-of-flight is replaced by the mean time-of-flight $t(E_\parallel)$ from equation 2.11, the momentum in the transversal direction becomes:

$$p_\perp = \left(11.6\frac{\text{a.u.}}{\text{amu eV}}\right) \cdot \frac{R}{2a} \cdot \sqrt{qU \cdot m}. \tag{2.15}$$

The substitution of $t(E_\parallel)$ by the mean time-of-flight follows the same reasons as in the last section. Additionally, the azimuthally direction angle φ in the detector plane can be determined using the two independent x and y coordinates on the detector. With this direction angle and the absolute value of the momentum $p_\perp$ the momentum in the detector plane can be displayed in polar coordinates.

2.2.2.3   Electrons transversal

Due to their lower mass, electrons are much more deflected by the magnetic field B than the ions. The magnetic field that is applied in the longitudinal direction, forces the electrons onto cyclotron orbits with the frequency $\omega_c = e\,B/m$ in the transversal plane. The calculation of the momentum components is again in polar coordinates $(p_\perp, \varphi)$.

Starting from the reaction point the electrons start their cyclotron motion with the starting momentum $p_\perp$ that has to be determined. The radius r of the cyclotron orbit is:

$$r = \frac{p_\perp}{eB}. \tag{2.16}$$

Unfortunately, the cyclotron radius cannot be observed in the experiment. Therefore it has to be identified indirectly from the distance R between the point of incidence and the image of the interaction point on the detector. This image coincides, due to symmetry reasons, with the center of mass in the detector picture. The point of incidence depends on the rotation angle traveled in the time-of-flight t_{tof}:

$$\alpha = \omega_c t = \frac{eB}{m} t_{tof}. \tag{2.17}$$

With the help of the formula that is known from geometry for the chord [119] in dependence of the radius r and the rotation angle α follows:

$$\left| \sin \left(\frac{\alpha}{2} \right) \right| = \frac{R}{2r} \quad \Rightarrow \quad r = \frac{R}{2 \left| \sin \left(\frac{\omega_c t}{2} \right) \right|}. \tag{2.18}$$

By inserting equation 2.16 and 2.17 into the initial transversal momentum in atomic units unfolds:

$$p_\perp = \left(8.04 \cdot 10^{-3} \frac{\text{a.u.}}{\text{mm Gauss}} \right) \cdot \frac{R\,B}{2 \left| \sin \left(\frac{\omega_c t}{2} \right) \right|}. \tag{2.19}$$
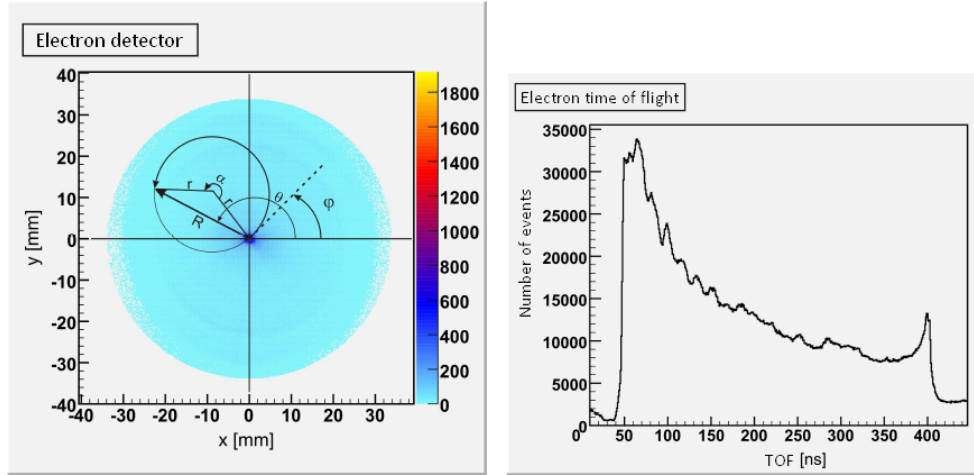

Figure 2.9: Spatial and time-of-flight spectrum of electrons ionized from neon at a photon energy of 44 eV. The values drawn into the spatial spectrum (left) are related to the momentum calculation as described in the text. (Picture taken from [120].)

In order to determine the direction besides the absolute value of the transversal momentum, the emission angle φ is needed in relation to an arbitrary reference axis in the detector plane. To this end, the angle θ, which is enclosed by the position R on the detector and the reference axis (see fig. 2.9) is measured. From this angle θ the angle α, which is covered in the time-of-flight, is subtracted or added, depending on the direction of the magnetic field, and the result is:

$$\varphi = \theta \pm \alpha = \arctan \left(\frac{y}{x} \right) \pm \frac{\omega_c t}{2}, \tag{2.20}$$

where the sign of the angle α is specified by the direction of rotation in the detector plane that is induced by the magnetic field. The x axis of the detector is chosen as the reference axis for the angle θ.

It has to be kept in mind that electrons with a time-of-flight corresponding to a multiple integer of the cyclotron period $2\pi/\omega_c$ are, independent of their initial momentum,

mapped onto the image of the interaction point on the detector. For these electrons all the transversal momentum resolution is lost.

For the absolute value as well as for the angle of the momentum of the electron the absolute time-of-flight is needed, which can be determined by the periodicity of the electron motion. These electrons with time-of-flights matching a multiple of the cyclotron period are mapped onto the image of the interaction point on the detector. If, for example, R is plotted versus the time-of-flight, the cyclotron period can be revealed by means of the points with minimal transversal latitude, so called "wiggles". Because an electron with zero time-of-flight has started at the interaction point, this point in time has to coincide with a "wiggle". So if the time-of-flight is known with the accuracy of one cyclotron period, then the absolute time-of-flight can be determined with a precision of the measurement of the cyclotron frequency. With typical cyclotron frequencies in the order of 30 ns this precondition can easily be fulfilled.

2.2.2.4   Electrons longitudinal

The magnetic field does not affect the longitudinal electron motion in the chosen geometry. Hence, only the time-of-flight is required for the computation of the longitudinal momentum. The approximation that the energy gained in the electric field is much larger than the energy obtained in the reaction is not valid in this case. Therefore equation 2.11 is solved for $E_\parallel$ and for the momentum in atomic units unfolds:

$$p_\parallel = \left(0.457 \cdot \frac{\text{a.u. ns}}{\text{mm}}\right) \frac{a}{t} - \left(80.4 \cdot 10^{-3} \frac{\text{a.u. mm}}{\text{ns eV}}\right) \frac{qU}{a} t_e, \qquad (2.21)$$

where a is again the acceleration length and t_e stands for the time-of-flight of the electron.

2.2.3   Resolution and acceptance of the spectrometer

The resolution is mainly determined by the target temperature and also the uncertainty of the spatial and temporal measurement. Those uncertainties arise because of the spatial resolution, the reaction volume and the temporal resolution of the applied data acquisition system. Additionally, inhomogeneous electric and magnetic fields can influence the resolution, but this can be neglected in this instance.

Depending on the particle species and the direction, the resolution is dominated by different factors. For example the target temperature is nearly insignificant for electrons whereas it is the major contribution to the error in the ion momenta measurement. Therefore and in order to give greater clarity, the following sections are split into sections for particle species and momentum components.

2.2.3.1 Ions

With equations 2.13 and 2.19 from section 2.2.2 the following terms for the quadratic error in longitudinal and horizontal direction can be conveyed:

$$\Delta p_{\parallel}^2 = \left(\left(8.04 \cdot 10^{-3} \frac{\text{cm a.u.}}{\text{eV ns}} \right) \frac{qU}{a} \right)^2 \Delta t^2 + \Delta p_{therm}^2, \tag{2.22}$$

$$\Delta p_{\perp}^2 = \left(\left(11.6 \frac{\text{a.u.}}{\sqrt{\text{amu eV}}} \right) \frac{\sqrt{qU \cdot m}}{2a} \right)^2 \Delta R^2 + \Delta p_{therm}^2. \tag{2.23}$$

Here Δt and ΔR are the uncertainties in the measurement of the time and the point of incidence. They are determined by the temporal resolution of the data acquisition system and the extension of the reaction volume and the spatial resolution of the detector. The thermal momentum spread, Δp_{therm}, is the error induced by the finite target temperature. The target temperature is, as mentioned in chapter 2.2.1.1, depending on the backing pressure, diameter of the nozzle and the temperature of the gas in front of the nozzle. Target temperatures employed were of roughly two Kelvin [36] which led to a mean kinetic energy of 0.26 meV, corresponding to a mean momentum of $\Delta p_{x,therm} \approx 1.05$ a.u. for oxygen and $\Delta p_{x,therm} \approx 0.98$ a.u. for nitrogen. This is only valid for the expansion direction of the jet, which corresponds in our coordinate system to the x direction of the transversal plane. Perpendicular to the expansion direction, the width of the distribution of the target is determined by the skimmers and apertures. In this plane the momentum width is given by solely geometrical considerations using the jet velocity [5] and the size of the skimmers and the apertures. Considering only the first two skimmers, which have a fixed geometry, results in $\Delta p_{x,y,therm} \approx 0.156$ a.u. for oxygen and $\Delta p_{x,y,therm} \approx 0.146$ a.u. for nitrogen.

The minimal resolutions achievable (in atomic units), where errors for the spatial and temporal measurement of $\Delta R = 0.5$ mm and $\Delta t = 1$ ns, respectively, have been considered, are:

	Δp_x	Δp_y	Δp_z
O_2	1.146	0.204	0.156
N_2	1.011	0.191	0.146

In the experiment, the momentum resolution of the ions can be estimated on the basis of the sum of ion and electron momenta of a single ionization event. If the momentum of the photon is neglected, due to momentum conservation, the sum of electron and ion momenta of the single ionization is equal to zero. If it is presumed that the momentum resolution of the electrons is considerably better than for the ions, the width of the sum distribution is a direct measure of the latter. In figure 2.10 this is displayed for nitrogen.

The values obtained in this way are in line with the calculated values from above, only in the y direction do the values deviate strongly. This can be explained by the jet diameter

---

[5]The jet velocity results from $p_{jet} = \sqrt{5 k_B T_0 m}$, where k_B is the Boltzmann constant and T_0 is the temperature of the gas prior to the expansion [116].

of roughly one millimeter, because the y direction is the propagation direction of the FEL beam. This leads to an extended reaction volume in this direction.

Additionally, the angular resolution in the transversal plane can be written as:

$$\Delta\varphi = \frac{1}{p_\perp^2}\sqrt{(p_x \cdot \Delta p_y)^2 + (p_y \cdot \Delta p_x)^2}. \tag{2.24}$$

In this experiment the angular resolution was between $10°/p_\perp$ and $58°/p_\perp$ for nitrogen and between $11°/p_\perp$ and $66°/p_\perp$ for oxygen. For the first value it is assumed that the momentum vector shows in x direction for the second value in y direction.
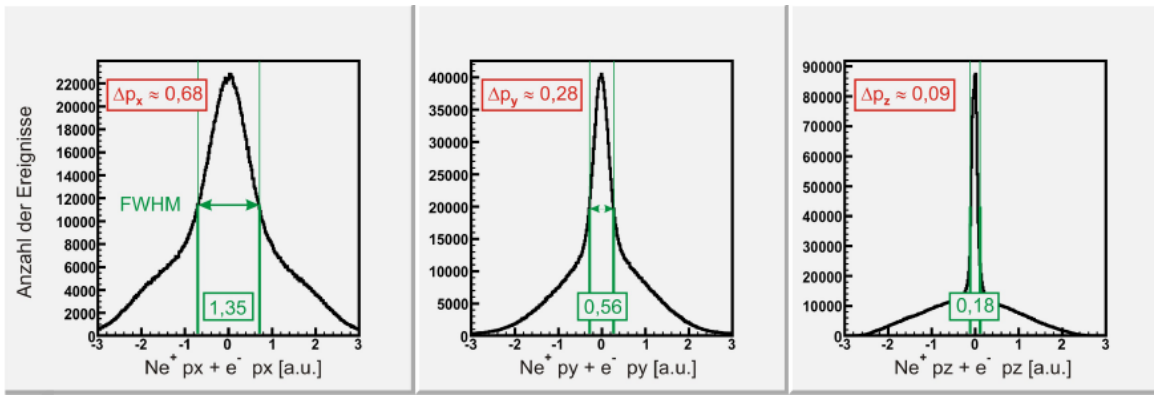

Figure 2.10: Sum of the momenta of electrons and ions in atomic units of the single ionization of neon subdivided in the three spatial directions. From the values the full width half maximum (FWHM) of the sum, the momentum resolution of the ions with $\delta p \approx \text{FWHM}/2$ can be estimated. (Picture taken from [120])

The solid angle acceptance of the spectrometer depends on the extraction voltage and the ion species detected. In the longitudinal direction an ion would get lost, if it would have enough starting energy to overcome the spectrometer potential and hit the electron detector. As mentioned above usually $qU \gg E_\parallel$ is valid, and therefore the acceptance in the longitudinal direction is not limited. In the transversal direction the ions which satisfy $R_\perp > R_{Det}$ are lost. For an applied extraction voltage of 40 V these are ions with $p_\perp > 160$ a.u. for nitrogen and $p_\perp > 140$ a.u. for oxygen. If the spectrometer voltage is chosen sufficiently high, this does not occur.

2.2.3.2 Electrons

First, the resolution of the electron spectrometer is determined by the uncertainty in the position and time measurement. The target temperature is negligible, as the released energy in the reaction is much larger than the thermal energy of the target. In contrast to ions, it is impossible for electrons to specify a value of the resolution for all three directions. Due to the magnetic field, the resolution depends on the starting momentum and on the

time-of-flight. This is expressed in the errors of the momenta and the azimuthal angle:

$$\Delta p_\perp = \left(\frac{8.04 \cdot 10^{-3} B}{2 \left|\sin\left(\frac{\omega_c t}{2}\right)\right|}\right) \sqrt{\Delta R^2 + \left(\frac{R \, \omega_c \, \Delta t}{2 \tan\left(\frac{\omega_c t}{2}\right)}\right)^2}, \tag{2.25}$$

$$\Delta\varphi = \sqrt{\left(\frac{\Delta R}{R}\right)^2 + \left(\frac{\omega_c}{2}\Delta t\right)^2}, \tag{2.26}$$

$$\Delta p_\| = \left(\left(0.457 \cdot \frac{\text{a.u. ns}}{\text{mm}}\right)\frac{a}{t^2} - \left(80.4 \cdot 10^{-3}\frac{\text{a.u. mm}}{\text{ns eV}}\right)\frac{qU}{a}\right) \cdot \Delta t. \tag{2.27}$$

The following tendencies are evident:

- In the longitudinal direction the resolution increases with larger times of flight.

- In the transversal direction the resolution is behaving periodically with the cyclotron frequency.

- For times of flight corresponding to an integer multiple of the cyclotron period (the so called "wiggles") the transversal momentum resolution vanishes.

Additionally, a detailed analysis shows that the resolution of the azimuthal angle gets better with increasing transversal momentum, whereas the resolution of the transversal momentum itself, (as well as the energy resolution) decreases with larger values [116]. The acceptance of the electron spectrometer is limited mainly by three factors. First, in the longitudinal direction by the voltage that is applied to the spectrometer. If the kinetic energy of the longitudinal movement away from the electron detector is large enough to hit the ion detector, it is lost. From this the following condition for the momentum in longitudinal direction emerges:

$$p_\| < -\sqrt{eU/13.6 \cdot \text{a.u./eV}}. \tag{2.28}$$

Second, the acceptance in the transversal direction is constricted by the size, R_{Det}, of the electron detector. This determines a fixed value for the magnetic field for which the maximum transversal electron momentum is detected at any time-of-flight. The associated condition is:

$$p_\perp < \left(4.02 \cdot 10^{-3}\frac{\text{a.u.}}{\text{mm Gauss}}\right) R_{Det} \cdot B. \tag{2.29}$$

Third, the so called dead time of the data acquisition system. It is the time period, during which two electrons that hit the detector shortly after another cannot be distinguished. The dead times of the types of detectors which were used during this work were between 10 ns and 20 ns.

2.3   The split-mirror setup

To realize XUV-XUV pump probe measurements a split mirror setup was developed. Such an arrangement has the advantage that the intensity on each mirror can be chosen freely. The functional requirements for such a setup are challenging, due to of the geometry of the spectrometer and because of the very high vacuum requirements in the main chamber, which is below 10^{-11} mbar. Therefore differential pumping was required. Because of the design of the reaction microscopes, the focal length could not be shorter than 500 mm in the experiment at FLASH and 600 mm at SCSS. The focal width was about 10 μm, which means that for overlapping the two foci an accuracy of at least 1 μm was necessary. This translates to an angular accuracy of 2 μrad. Therefore the edge of the mirror has to be positioned correctly within 20 nm. Additionally, the complete beam has to be within the target gas jet, which has in extreme cases, a diameter of 50 μm. Therefore, the tip and tilt for the upper mirror and the delay stage on which the lower one is sitting have to be moved with a precision below 5 μm to hit the jet at the point of the highest density.
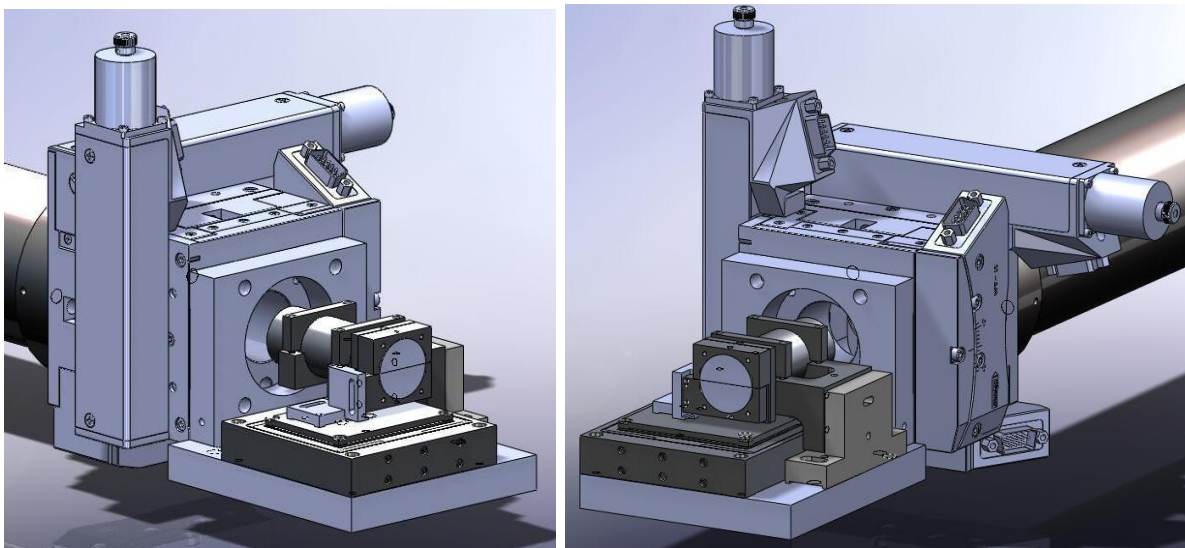

Figure 2.11: Technical drawing of the complete mirror holder. The goniometers for the vertical and the horizontal movement can clearly be seen. The horizontal plate with the devices for the delay and the spatial overlap can easily be removed to change the mirrors and for other adjustments. The top mirror can be tipped and tilted with a precision of 0.5 μm in the focal plane to achieve an overlap between the two foci. The lower mirror is sitting on a delay stage that allows to drive delays up to $\pm$ 2.6 ps with a resolution of 4 as.

Furthermore this complete device has to be be able to be shifted along the laser propagation axis to align the focus within the target. For that the alignment is only required to be one tenth of a mm to be successful. Additionally, the incoming beam is required to hit the mirror centrally. To achieve this, the mirror setup is mounted on a three axis manipulator. As knowledge about these parameters was sparse prior to the experiment,

extensive tests with a preliminary device using IR lasers had to be carried out in Heidelberg and the FEL in Hamburg. We also found that closed loop actuators were crucial for a reliable working setup. Learning from extensive tests contributed to building a very successful device (see 2.11) that was used at FLASH in Hamburg. The success of the setup was the reason that it was requested to be used by Prof. Kiyoshi Ueda's group at Tohoku University in Sendai for its use within a collaboration at SCSS in Harima, Japan.

2.3.1 The XUV-pump XUV-probe setup

In addition to the accuracy requirements of the optical system the opto-mechanics had to be integrated into a system that had to meet the following requirements:

- UHV compatibility down to a pressure in the order of 10^{-10} mbar

- vibrational engineering to prevent oscillations of the mirrors

- good accessibility of the mirrors to exchange them within short time periods if a wavelength change is to be undertaken

- easy and precise pre-adjustment

- an imaging system for the spatial and temporal overlap that can be used autonomously (see 2.3.1.1)

- the mirror surface had to be electrically isolated from the ground and connected to the outside to act as a Faraday cup. This way a trigger signal for the measurement was obtained [121].

The gap between the two mirrors is parallel to the jet. This had been designed this way intentionally because it was experienced that the incoming light had to be blocked from the jet to avoid too many events from the incoming unfocused light. This is done by a wire inserted into the beam (see figure 2.4) Also, the friction afflicted designs of usual mirror mounts are not working reliably at such a high vacuum, as they tend to jerk. To avoid this, we eliminated friction bearings in the setup.

For the movement of both mirror halves we applied a set of two different goniometers (WT-85 and WT-100 manufactured by *MICOS*, see ref. [122]) mounted orthogonally onto each other. This setup creates a common center of rotation and was designed to have the pivot point for all axes within the mirror surface to prevent any deviation. They also have a smooth and quiet motion, even under vacuum and they have a resolution better then 3 μm in the focal plane, with a total travel range of 10°.

For the overlap between the foci we chose the S-325 piezo tip/tilt platform from *Physikinstrumente* [123]. It does not have any moving parts and has a frictionless, flexure guiding system. It has a resolution of 0.1 μrad translating in a resolution of 0.5 μm in the focal plane. The upper half mirror is mounted on the tip/tilt platform to overlay its focal point with the other mirror half sitting on the delay stage. The total range in the focal plane is approximately ± 4 mm at a focal length of 500 mm.
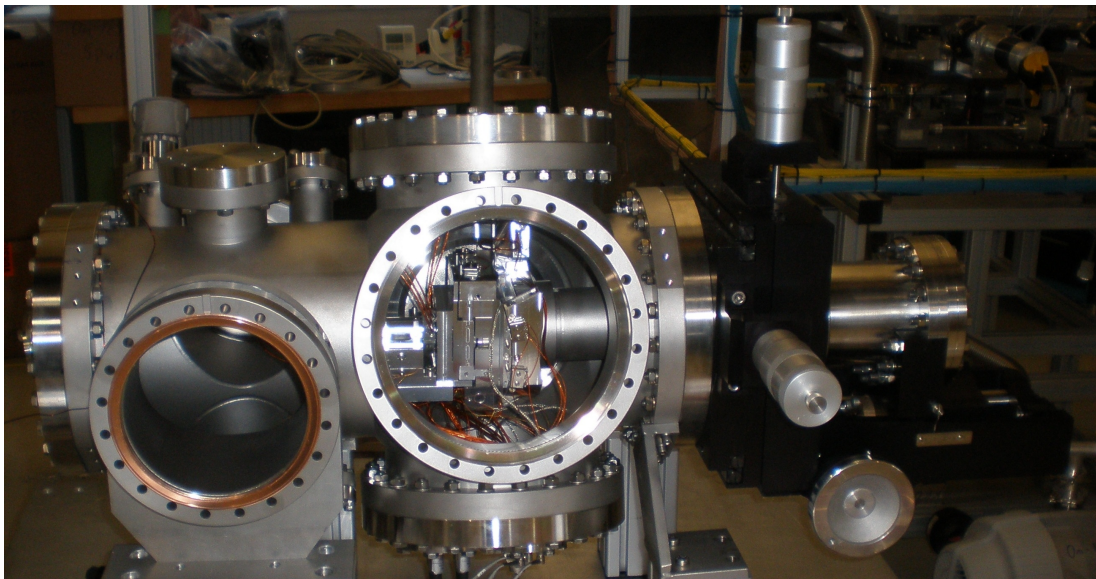
Figure 2.12: Picture of the complete mirror chamber including the 3D manipulator and the mirror setup. The CF200 double cross is twisted against the rest of the chamber because otherwise the goniometers would not fit into it. The mirror setup is sitting on a tube which is connected to the movable flange of a manipulator, to allow 3D positioning of the mirror.

To adjust the delay between the pump and the probe pulse a piezo driven guiding system with a closed loop capacitive encoder [124] is implemented. It is the P-628 piezo stage built by *Physikinstrumente*, with a resolution of 0.5 nm. This corresponds to a delay resolution of approximately 4 as. With a pulse length of more than 10 fs this is more than sufficient. The total travel range is 800 μm. We usually put the point of zero delay into the middle of the delay range, which leads to the ability to drive delays of about ± 2.6 ps. For autocorrelation measurements we usually applied only ± 100 fs delays and for experiments on molecules we used up to ± 500 fs delays.

2.3.1.1   The imaging system

The imaging system can by driven by two different lasers. The first one is the beamline laser of the FEL, a HeNe laser which is collinear to the FEL beam, the other is a diode laser build in our user experiment. With the beamline laser the spatial overlap can be checked and also it can be made sure that the mirror is hit on the right spot to illuminate both mirror halves equally. Also we have to use it to pre-align the position of the whole mirror to be sure that the reflected beam transits the spectrometer and the main chamber without clipping. The temporal overlap cannot be checked with the HeNe. The diode laser has two advantages: Firstly, it has a relatively broad spectrum which leads to a short coherence length. This means that only for a distance of about 10 μm around the point of zero delay an interference pattern is visible. This way we can determine the point of zero time delay within a few microns and minimize the alignment-time with the XUV beam.
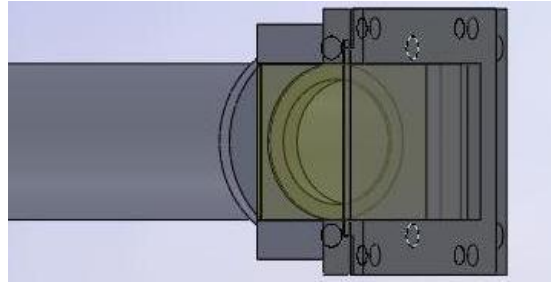
Figure 2.13: Schematic drawing of the reflector holder of the imaging system. The three different possibilities of imaging can be seen. The YAG crystal (yellow) converts the XUV radiation into visible light, so the beam profile can be checked. Secondly, the glass plate is used for the imaging using the HeNe beamline laser. It is used to pre-align the position and direction of the mirror, as well as the spatial and temporal overlap.

For the imaging of the foci with a camera, a glass plate (see fig. 2.13), which is sitting on a linear manipulator, can be driven into the beam. The glass plate is used with the beamline laser in a way that the incoming HeNe passes through it and hits the mirror. The back reflected beam from the mirror is reflected by the same glass plate and leaves the vacuum chamber through a window and shines on a camera. Then the two spots of the half-mirrors or their interference pattern are inspected (see fig. 2.14). The interference pattern can be used to align the overlap in the horizontal plane. To use the diode laser it is shone on the glass plate so that the reflection hits the split mirror in the center. Then the reflections of the two mirrors are guided out of the vacuum chamber by the glass plate. There they are observed by a CCD camera. The interference pattern can also be used to adjust the horizontal alignment very precisely (down to 50 μm). The interference stripes (see fig. 2.14) have to be precisely horizontal. Using the camera one can see that the two beams are parallel in the horizontal plane. The vertical pre-alignment depends strongly on the divergence of the laser and since the divergence of the diode laser and the FEL are different, the vertical pre-alignment is not necessarily accurate.
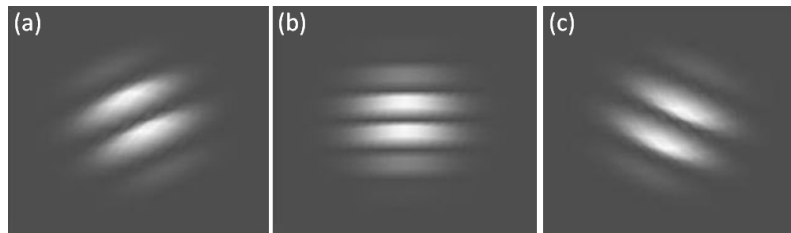
Figure 2.14: Illustrated are interference patterns for different positions near the spatial and temporal overlap. Due to the geometry of the "interferometer" (the symmetry axis is horizontal), lines are visible. (a) If the movable half-mirror is shifted to the left, the lines will be tilted to the left. (c) Same as (a), if the mirror is shifted to the right. (b) If the horizontal position is correct, the interference fringes are perfectly horizontal.

Chapter 3

Pulse characterization at FELs

It is crucial for the understanding of the experimental results outlined in this thesis, to elaborate on the temporal pulse shapes of free electron lasers (FELs) operating in the Self-Amplified Spontaneous Emission (SASE) mode. The FEL pulse emerges from shot noise resulting in significant fluctuations in the pulse shape from shot to shot. This can be seen in the extensive variability of single-shot spectra [125, 126]. For non-linear matter - light interactions, the temporal and spectral shape of the pulse is a fundamental parameter and certain pulse-shape properties must be known or assumed for meaningful analytical or computational modeling of FEL - matter interaction [127].

The characterization of the XUV pulses of a FEL is not trivial. Possible experiments are for example, streaking measurements with an IR laser or terahertz radiation but a jitter between those pulses and the FEL pulse is immanent and therefore other techniques are required to characterize those pulses. An autocorrelation measurement of the XUV pulses is challenging and requires a XUV-pump XUV-probe setup, which is a cutting edge technology. We were the first to do such characterization of the FEL pulses of SCSS in Japan and only the second team at FLASH in Hamburg.

3.1   Autocorrelation

If a very short laser pulse with a pulse duration on the order of some fs has to be measured, all electronic devices are much too slow to measure the temporal pulse shape. A way to overcome this limitation is to use the pulse itself for its characterization. In this technique, a non-linear signal, e.g. a non-linear ionization process or the production of second harmonic radiation of an optical frequency in a crystal, is observed as a function of time delay that is introduced between two equal splits of the pulse. It can be described as:

$$\Psi_{II}(\tau) = \int_{-\infty}^{\infty} I(t)I(t-\tau)dt \ / \ \int_{-\infty}^{\infty} I(t)^2 dt, \qquad (3.1)$$

where $I(t)$ is the temporal intensity distribution of the pulse and τ, is the delay between the two pulses. The resulting function, $\Psi_{II}(\tau)$, is the observable and in our case detected by the nonlinear ionization of an atom or a molecule.

Unfortunately, the autocorrelation function is not unambiguous, because the chirp of the pulse cannot be measured. This means, that an autocorrelation measurement does not fully characterize a pulse. This can only be done e.g. by a SPIDER (Spectral Phase Interferometry for Direct Electric-field Reconstruction) [128] measurement, which is, up to this point, not possible in the XUV regime.

If a Gaussian shaped laser pulse is assumed, the FWHM of the autocorrelation trace and the pulse width are linked by $\tau_{FWHM} = \sqrt{2} \cdot \tau_{pulse}$. Where τ is the width of the pulse or of the autocorrelation trace.

Autocorrelation traces were measured with the split mirror setup described in section 2.3, using a reaction microscope, introduced in section 2.2, for detection. The XUV beam was focused into the target jet and the ion yield was measured while the delay is altered continuously. This leads to an intensity autocorrelation. The repetition rate of the FEL was between 300 and 500 shots per second at FLASH and 60 shots per second at SCSS. With the single event detection scheme, this translates, depending on the target, to between three hours acquisition time for the argon measurements and up to 22 hours for the nitrogen data.

3.2   Pulse structures of a FEL

As mentioned in the introduction, the FEL pulse emerges from shot noise and has therefore a chaotic structure. Earlier measurements [38, 129] showed a multi-peak structure with two to four narrow intensity spikes with a width of approximately 10 fs within a structure of some tens up to some hundred fs. The sharp peak can be described as the coherence time of the FEL-pulse. In the first characterization of the XUV pulses of FLASH performed by Mitzner *et al.*, they found that the visibility of an interference pattern was only given for a delay up to ± 6 fs and concluded that the coherence time of FLASH was 6 fs (see ref. [125]). Due to their short coherence time compared to the overall pulse length, these pulses have a very different behavior in an autocorrelation measurement than the ones derived from an IR femtosecond laser system.
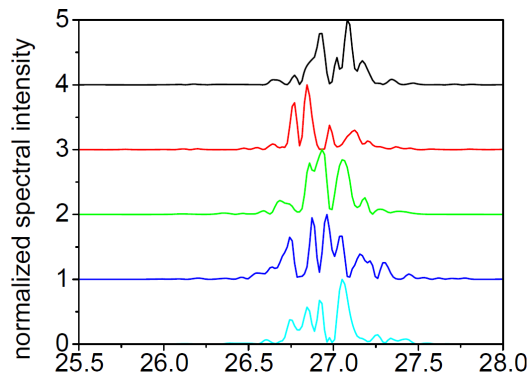

Figure 3.1: Numerical results for spectral characteristics of single-shot spectra using an assumed FEL pulse duration of 25 fs.(picture taken from [130]).

Using the recently published partial coherence method (PCM) by Pfeifer *et al.* it was possible to reproduce the single shot spectra and single shot pulse shapes of the pulses of FELs (see ref. [130]) by generating statistically fluctuating, partially coherent individual FEL pulses from the measured average frequency spectrum and the average pulse duration. This way it was possible to generate a top down method for the simulations of the experimental conditions without a priori knowledge of the precise accelerator and undulator conditions. This is necessary since these conditions vary due to thermal drifts and resulting readjustments of the machine.

While the average spectrum of a measurement-run at FLASH looks relatively Gaussian shaped, measurements of single shot spectra show that the spectra of the pulses consist of several incoherent peaks (see ref. [125]). These spectra could be simulated within a very good agreement, as can be seen in figure 3.1.

In figure 3.2, different pulse shapes are simulated from the modeled spectrum and it is shown that they lead to different autocorrelation traces. The sharp peak around zero results from spikes in the pulse structure whereas the total pulse length is visible in the width of the broader Gaussian-shaped structure below the peak. In the literature this shape of an autocorrelation trace caused by spikes in the temporal structure is sometimes called *German helmet effect*. As we found out during our last beam time at FLASH, the broader structure can be controlled by the length of the electron bunch.
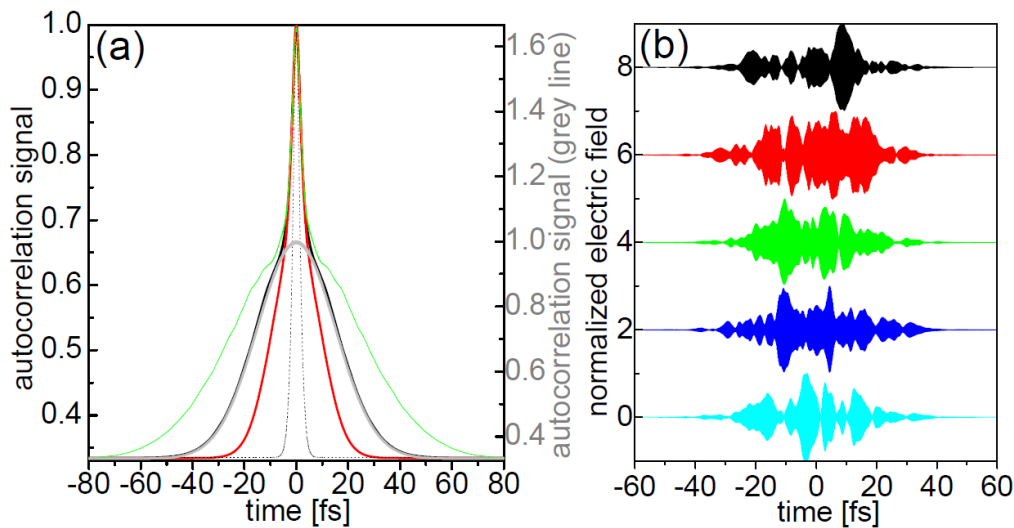
Figure 3.2: Temporal properties of pulse shapes obtained by a simulation based on measured spectra. a) Calculated average autocorrelation traces. Different FEL pulse durations (FWHM) are assumed: 15 fs (red line), 25 fs (black line) and 40 fs (green line); more than 1000 pulse shapes are calculated and averaged over. For comparison, the autocorrelation for a bandwidth-limited pulse of 25 fs duration centered at around 27 nm wavelength is shown (grey line), as well as a bandwidth limited pulse width. b) Single-shot temporal pulse profiles simulated with the same spectrum (picture taken from [130]).

3.3   Results and Discussion

Autocorrelation measurements were performed at two different free electron lasers. At SCSS it was the first time that such a measurement was accomplished. The autocorrelation trace pictured in figure 3.3 was measured in helium at a photon energy of 20 eV. This means that 2 photons have to be absorbed simultaneously to overcome the ionization potential of 24.5 eV. This is leading to a very clear second order autocorrelation measurement. Unfortunately the contrast between the peak and the background is not as good as a perfect autocorrelation would let expect. This has two causes. One is the not perfect overlap geometry with a split mirror, where the delayed pulse is not only moving along the laser propagation axis but also slightly up and down. The other reason is that even if the probability to ionize sequentially is very small it is larger than zero. This results in a background level of events at all delays and in some cases like, in figure 3.5, the first reason can cause that the background at positive and negative delay is not even the same. Nevertheless this does not affect the significance of the measurements.
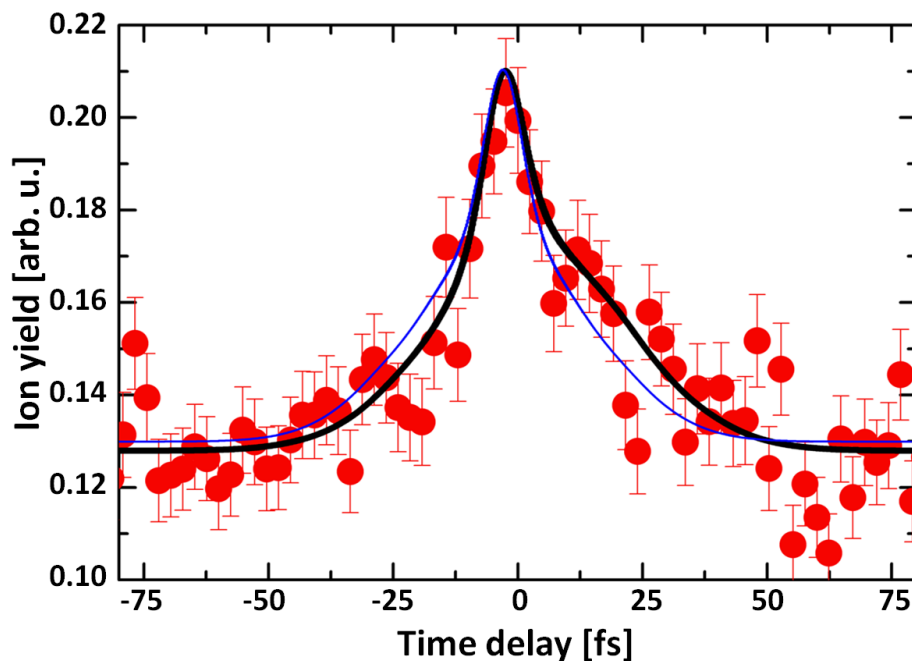
Figure 3.3: Autocorrelation trace measured with a photon energy of 20 eV in the single ionization of helium at SCSS. Black line: PCM result for identical pulse replicas normalized to the same maximum value as the experiment. Blue line: PCM result including pulse-front tilt (see text). Picture taken from [131]

The autocorrelation trace is pictured in figure 3.3 in the red data points. Additionally the result of a PCM simulation that assumed a Gaussian shaped FEL pulse with a temporal width of 28.3 fs is plotted in blue. For a better comparison a constant background is added and the y-axis is scaled to fit the experimental data. Even though reasonable agreement is

obtained, the experimental autocorrelation spectrum shows a significant asymmetry with respect to time zero that is not explainable with the model calculation discussed above. An autocorrelation trace has to be symmetric and therefore this can only be explained when he two replicas of the pulse differ significantly. The incoming beam with a diameter of 10 mm is cut by the split mirror horizontally. This directly implies that the FEL pulse shape changes along the vertical beam cross-section what can be either explained by a spatial chirp, which can be neglected for a non bandwidth-limited FEL pulse, or by a pulse front tilt. Such a pulse front tilt is induced when the electron beam in the undulator and the undulator-axis are not parallel.

If now a pulse front tilt is added to the PCM via a simple model (black line in fig. 3.3), the simulation is in excellent agreement with the experimental data for an envelope offset time [1] of τ=2.9 fs and an average FEL pulse duration of 28.3 fs (FWHM). Conversion of the envelope offset time into a pulse-front tilt angle leads to a value of $\sim 0.02°$. At a beam diameter of 10 mm this translates to an offset of 3.5 μm of the wave fronts, this apparently small effect results into a significant broadening of the pulse-width by $2\tau \sim 5.8$ fs in the focus. This is about 20% of the total pulse duration.
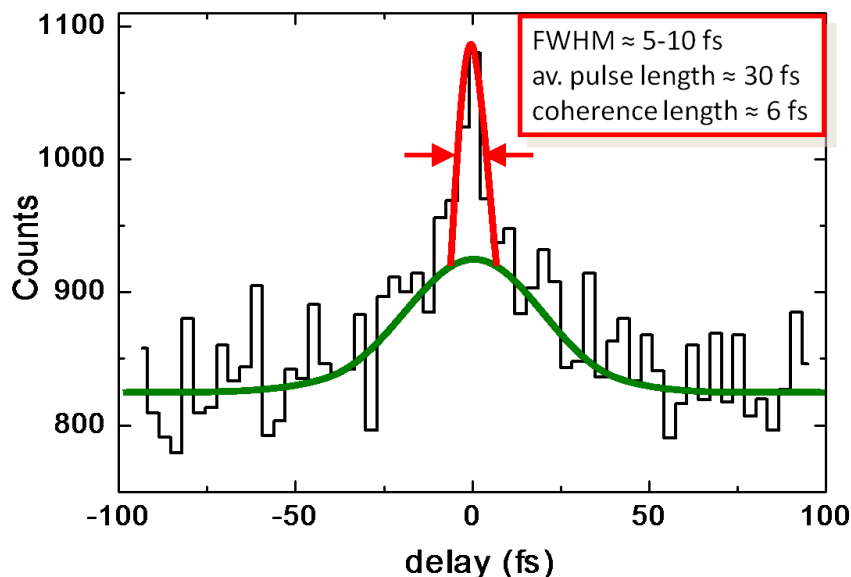

Figure 3.4: The result of an autocorrelation measurement in nitrogen with a photon energy of 46 eV is illustrated. The doubly charged atomic ions are plotted. A clear peak with a width of 5 to 10 fs is visible, whilst the average pulse length is 30 fs.

Before the shutdown and remodeling of FLASH we were able to measure autocorrelation traces in oxygen and nitrogen at photon energies of 46 eV and 38 eV. At these levels of photon energy, an autocorrelation in rare gases was not possible because of resonant states

---

[1]The light pulse can be described in the lab-system as a disk with a diameter of 10 mm and an length of 10 μm. Then a pulse front tilt can be understood as a tilt of this disk against the flight path. The envelope offset τ is the defined as the time delay between the upper edge of the disk and lower one.

present in the ionization, which resulted in efficient sequential double ionization. A clear autocorrelation measurement requires at least direct two-photon ionization for the last step, without long living intermediate states.
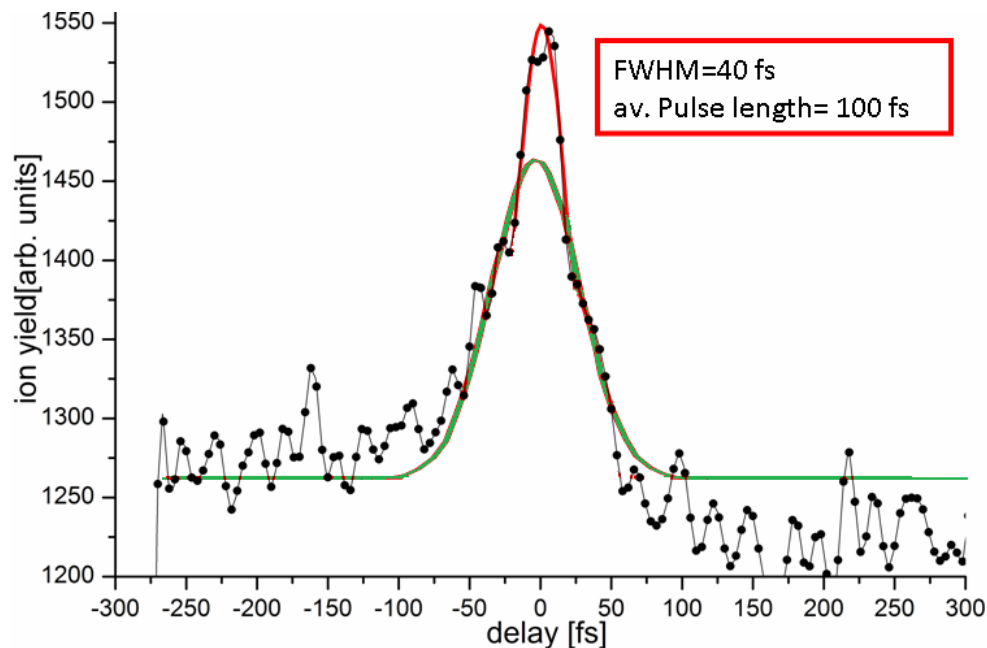

Figure 3.5: Measurement of the pulse structure taken in 2009 of the double charged oxygen atoms at a KER between 30 and 60 eV recorded with a photon energy of 38 eV. Two temporal structures are visible. The shorter one has a width of approximately 25 fs, whereas the longer one is 100 fs.

In the first measurement (see figure 3.4), recorded with a photon energy of 46 eV, a clear temporal structure with a width as small as 10 fs is visible. This short temporal structure can be explained by the spikes in the pulse, called coherence time by Mitzner *et al.* [125], in association with the high energy that is needed for this channel. This way, the low energy base of the pulse cannot contribute but the large intensity of the spike together with the lower and broader base is forming the broader sub-structure and is showing the average pulse length. When this result is now compared to the same autocorrelation trace measured with a photon energy of 38 eV one year later, one can see significant differences (cf. figure 3.5). The broader sub-structure is significantly longer with a width of 100 fs and the sharper one has nearly three times the width with approximately 25 fs. This shows that at different settings of the accelerator strikingly different pulse structures are immanent. Concluding, in order to understand the dynamics in the measurement, the characterization of the pulse is crucial and it must not be assumed to have the same conditions from measurement to measurement.

Before the remodeling of FLASH, the electron accelerator produced a very sharp peak in the temporal electron distribution. This led to the short XUV pulses described above. Since the remodeling in 2010, the length of the electron bunch is tunable to gain larger
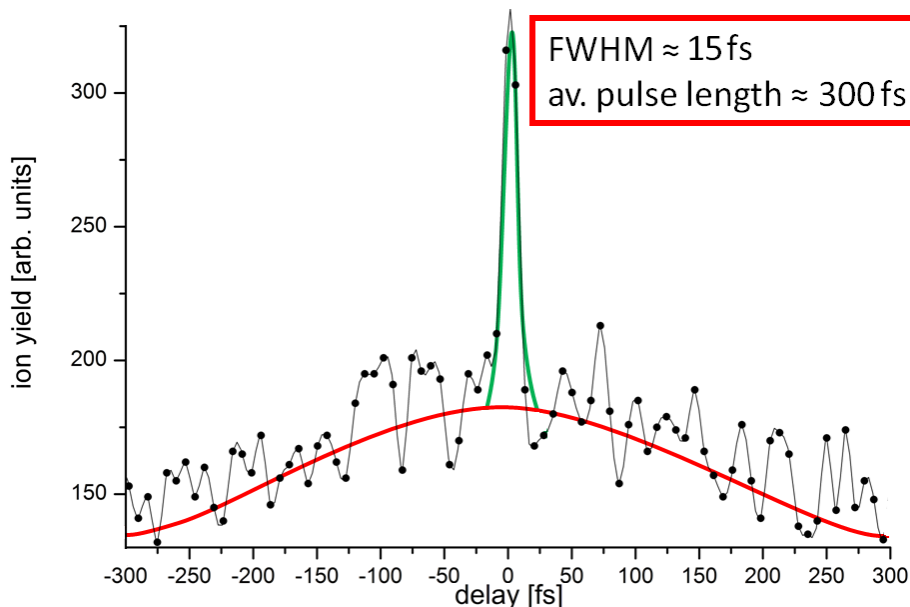
Figure 3.6: Autocorrelation trace of the fourfold ionization of argon with a photon energy of 28 eV. A narrow peak with a width of 15 fs that is sitting on a very broad structure with a width of approximately 300 fs is visible.

photon fluxes with a long pulse for spectroscopy experiments. But in our first beamtime in Oct. 2010 it was significantly longer than in previous beam times. The remodeling improved the photon flux by putting more electrons into the bunches, but with standard parameters only 500 fs pulses were achieved, instead of 30 fs before the remodeling.

After the remodeling in measurements with a photon energy of 28 eV, autocorrelation measurements were possible in argon. In the fourfold ionization of argon, the last two photons have to be absorbed in a non sequential way at this wavelength. This leads to a very clear autocorrelation trace with a good signal to background ratio (cp. figure 3.6). It is visible that the two temporal structures differ more than in the autocorrelation traces shown before. While a sharp peak with a width of about 15 fs is visible, the longer structure has a FWHM of approximately 300 fs. This demonstrates the necessity to shorten the pulse durations, which were achievable right after the remodeling of FLASH.

In the course of the beam time, it was possible to compress the FEL pulses. This was accomplished by reducing the bunch charge feed into the accelerator and therefore into the undulator. On one hand this reduced the photon flux but in parallel it was possible to reduce the length of the electron bunch. By reducing the bunch charge from 0.4 nC down to 0.1 nC it was achieved to reduce the FEL pulse length down to 70 fs (see figure 3.7. Further work will be necessary to reach short pulse durations again at FLASH.
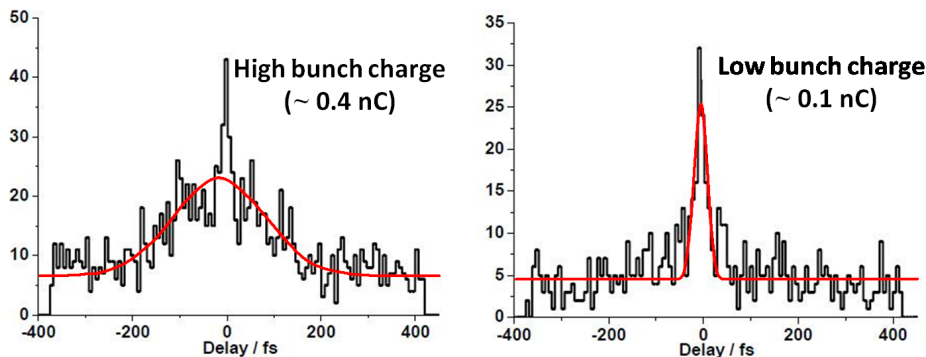
Figure 3.7: Effects of bunch charge variation on the FEL pulse measured in the fourfold ionization of argon. A lower bunch charge clearly reduces the pulse length. This can be seen in the substructure below the sharp coherence spike which is much narrower than measured with the higher bunch charge of 0.4 nC.

3.4   Conclusion

In this chapter it was shown, that the XUV-pump XUV-probe experiment allows to characterize the temporal profile and the coherence length of the FEL pulses. A temporal structure with short spikes indicating the coherence length was revealed using calculations. We furthermore studied the pulse duration as a function of the accelerator settings and found an anticorrelation between the bunch charge and the pulse duration. The results presented here have important consequences for any time-dependent measurement at FELs since the here identified pulse-front distortion may occur at any VUV and X-ray SASE FEL and, moreover, might be expected to depend on the actual settings of the machine.

Chapter 4

XUV pump - XUV probe experiments on femtosecond nuclear wavepacket dynamics in O_2 and N_2

Although ultrafast nuclear wavepacket dynamics in diatomic molecules were explored with strong few-cycle IR laser pulses [85, 87, 88, 95, 132], employing ultra-short XUV pulses may provide a different insight into the dynamics of chemical reactions. While the ionization and excitation of molecules in IR laser fields is typically a process involving many photons, XUV radiation can reduce the ionization and excitation to a single-photon transition. Therefore XUV-pump XUV-probe studies may give insight into the dynamics of molecules under different conditions and provide data, where the dynamics is unperturbed from strong field effects.

In this chapter exemplary measurements for the homonuclear molecules N_2 and O_2 together with classical simulations of the nuclear dynamics are discussed. First the classical simulations are explained. Second, the experimental results are shown together with the simulations. The latter section of the results is split into one part for nitrogen molecules and another for oxygen molecules.

4.1 Classical simulations of nuclear dynamics following XUV photoionization

One-dimensional simulations of the dynamics of bound and dissociative ionic states of diatomic molecules were performed using a self-written C++ program. In the simulations the nuclei were assumed as point-like and the evolution in the potential is calculated classically. The potential curves for this approach were taken from the literature [102, 133–137]. The mass considered in the nuclear motion is the reduced mass $m_{red} = \frac{m_1 \cdot m_2}{m_1 + m_2}$. When homonuclear molecules such as N_2 or O_2 are considered, the reduced mass is simply $m_{red} = \frac{1}{2} m_a$, where m_a is the mass of an atom of the homonuclear molecule.

The dynamic calculation assumes a Franck-Condon transition from the ground state of
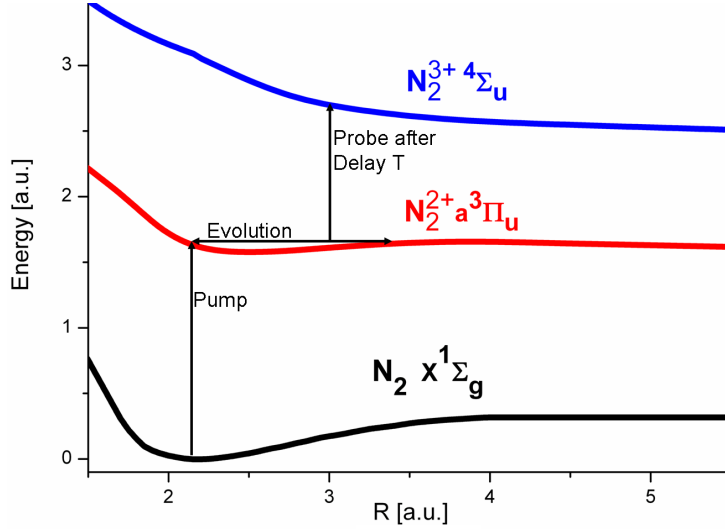
Figure 4.1: Scheme of the classical simulations. The simulation is started at the ground state internuclear distance in the ionic state assuming a Franck-Condon transition (in this example a N_2^{2+} state is populated in the XUV ionization of N_2 via the pump pulse). The nuclear dynamics evolves in this state for the delay time T. At time T, a second transition (induced by the XUV probe pulse) populates an energetically higher ionic state (here the N_2^{3+} state). The successive dynamics occurs on this final state and results in charged fragments with a kinetic energy release (KER) that depends on T.

the molecule into an ionic state as the first step (see Fig. 4.1). During this transition the internuclear distance remains constant and equals the equilibrium distance in the ground state. For the evolution in the populated ionic state, the force, $F(R)$, between the nuclei is calculated via the gradient of the potential V:

$$F(R) = -\frac{d}{dR}V_{pump}(R). \tag{4.1}$$

To consider the temporal evolution in this state, the velocity, $v(T)$, is calculated via,

$$v(T) = \int_T^0 \frac{F(R)}{m_{red}}dt. \tag{4.2}$$

Now the internuclear distance $R(T)$ at a given time T can be calculated via the integral,

$$R(T) = \int_T^0 v(t)dt. \tag{4.3}$$

For the numerical calculations, the integral was substituted by a sum over discrete steps in time, Δt, which were chosen as 10 a.u. corresponding to ≈ 240 as. In extensive tests with different step sizes Δt it was found, that this step size gives accurate results and further decrease of the step size does not improve the final results. Furthermore, for test

potentials, which allowed an analytical integration of eq. 4.3, a perfect agreement between the analytical and numerical simulations was found.

When $R(t)$ is known, the kinetic energy release (KER), that is the observable in the experiment, can be calculated for a given delay. The KER is the sum of the energy gained during the evolution in the first state populated after the XUV pump pulse and the energy gained in the second state populated after the interaction with the XUV probe pulse. A dissociation limit of 50 a.u. was assumed. The KER is calculated as:

$$\text{KER}(T) = \left(\hat{V}_{pump}(R(0)) - \hat{V}_{pump}(R(T)) \right) + \left(\hat{V}_{probe}(R(T)) - \hat{V}_{probe}(R(\infty)) \right). \qquad (4.4)$$

KER spectra as a function of delay could be calculated for the evolution in bound and dissociative states. [1]

4.2   Experimental data and modeling

The data presented here was measured at the free-electron-laser FLASH at a photon energy of 46 ± 0.5 eV and a pulse duration of $\sim$30 fs. The intensity in the focus was on the order of $10^{13} - 10^{14}$ W/cm^2. By implementing the split mirror setup (see chapter 2.3) at beam line 3 (BL3) of FLASH, we were able to perform the first XUV-pump XUV-probe experiments on molecules at sufficiently high XUV-photon fluxes to observe transitions involving two or more photons.

The results shown here may be seen as proof-of-principle experiments on the tracing of nuclear wavepacket dynamics in molecules in the absence of significant external field effects on the molecular potentials (such as eg. Stark-shifts). Further experiments performed under similar conditions, beyond the ones shown in this chapter, are the investigation of wavepacket dynamics in deuterium (see section 6) and the investigation of the dynamics in more complex molecules such as C_2H_2 (see [98]) and C_2H_4, which are not part of this thesis.

However the simulations were limited by the available potential curves. For the investigations on large delays up to 300 fs, the potentials had to be known up to distances of at least 50 a.u.. Those used here were taken from [102, 133–137].

First the results of the measurements on N_2 are presented for different ion species in coincidence where clear structures are visible. In non-coincident data, the molecular behavior cannot be observed in a clean way. There the dissociative contributions in KER vs. delay spectra are discussed. For the dissociative states a Coulomb potential was assumed. In the following the same is done with the results from the oxygen measurements.

Two different pathways are important in the pump-probe experiments. When a molecule is dissociating, the internuclear distance is small at short delay and increasing steadily. When these molecules are then probed at different delays, fragment ions can be observed that shows a decreasing KER with growing delay. This behavior is caused by the antiproportional R-dependence of the Coulomb-potential. A bound movement in contrast will,

---

[1]Note that even if the pump pulse populates a bound ionic state, the probe pulse typically leads to the dissociation of the molecule via highly charged repulsive ionic states.

due to the missing temporal resolution of the long pulses, show itself in a band in the KER versus delay spectra of a certain width where the upper energy can be understood as the inner turning point and the lower edge as the outer one. If fragment ions are produced already by the pump pulse and their energy is not further influenced by the probe pulse, a discrete horizontal line in the KER versus delay spectra can be observed. We will refer to these states as the "non-probed states".

For the singly charged oxygen fragments also bound states are discussed. Unfortunately it was not possible to reproduce these features in most of the spectra, because for higher ionized states no potential curves were available.

4.2.1 Dissociative states of nitrogen

4.2.1.1 Experimental results

Three different charge states for the final molecular state are discussed here: the doubly, triply and fourfold ionized molecule. Fragment coincidences of even higher ionized molecules were detected, but only with very poor statistics. The three dimensional momentum information of the two ions, needed for the determination of the KER is detected. Since the momentum of the electrons is very small compared to those one of the two ions, they can be neglected.

In figure 4.2 the coincident measurement of singly charged ions emerging from N_2^{2+} (a), coincidence between singly and doubly charged ions from N_2^{3+} (b) and between doubly charged ions from N_2^{4+} (c) are displayed. All of them share a well pronounced narrow dissociation curve at small KERs. The visibility is best in 4.2(a) where no other significant traces of dissociating molecules can be seen. Three broad bands emerging from bound states on the one hand and non-probed N_2^{2+} states on the other can be observed. They have different widths and are centered around KERs of 6.5 eV, 11 eV and 15 eV.

In 4.2(b) the mentioned dissociative curve can also be clearly seen. With a similar slope, the lower edge of the broad structure between 9 eV and 35 eV is likely formed by a bunch of states leading to similar KERs. Therefore the curve is smeared out and only a slight maximum in counts is visible. This dissociative curve with centre energy of about 9 eV at a delay of 300 fs unifies with the broad structure emerging from bound states towards larger energies. In this broad structure, unlike in the single charged ion coincidences, no substructures are visible. This can most likely be explained by the smearing of the states due to the involvement of more than one photon in the transition, since the photon energy does have a relatively large distribution. Also the population of non-probed states of N_2^{3+} is very unlikely since three photons would have to be absorbed in a non-sequential way.

The spectrum with the highest probing state charge with sufficient statistics is the one with coincident doubly charged ions emerging from a symmetric Coulomb explosion of the fourfold ionized nitrogen molecule (N_2^{4+}). It can be seen in figure 4.2(c). Here the lower dissociative band can be observed like in the other KER-vs.-delay-spectra, but the separation from the lower edge of the broad structure at 8 eV is not as pronounced as in the other spectra. But still it can be distinguished from the edge which is showing a
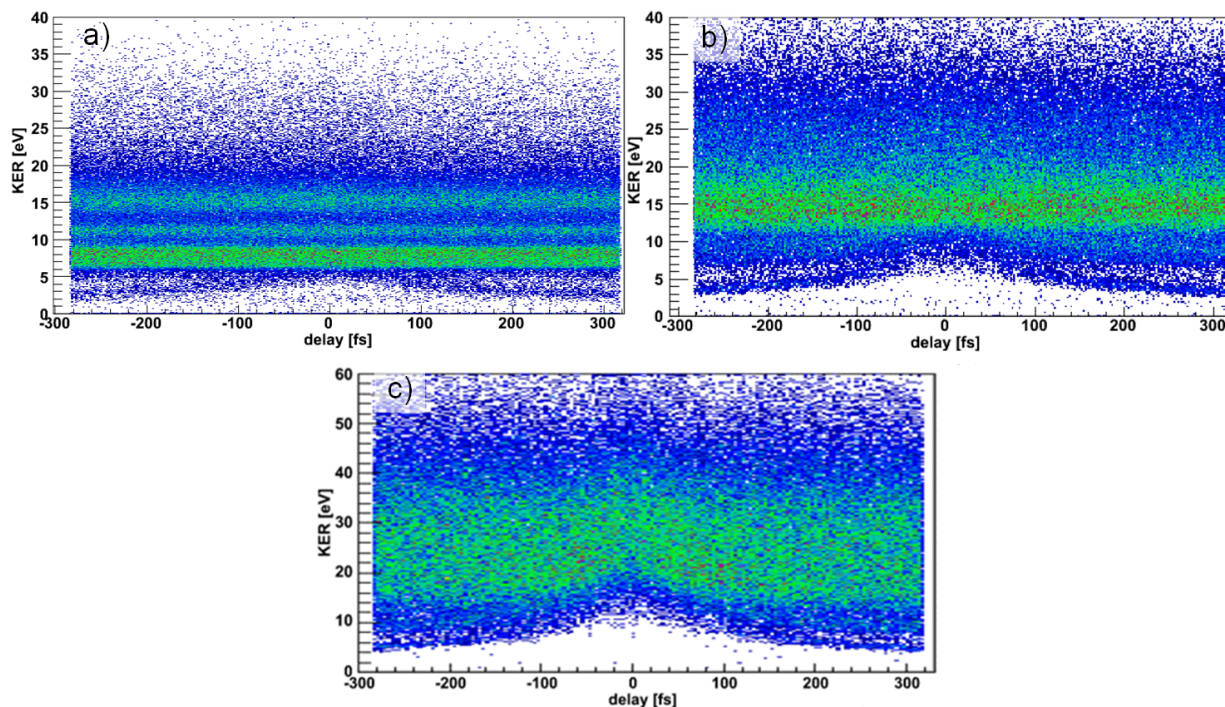
Figure 4.2: KER vs. delay spectra of in coincidence detected nitrogen ions measured at a photon energy of 46 eV. (a) N^+-N^+ coincidences; (b)N^+-N^{2+} coincidences; (c)N^{2+}-N^{2+} coincidences. The dissociative contributions mainly at low energies and some broad, time independent, events indicate contributions from non-probed states and from bound oscillating molecules can be seen.

very clear dissociative behavior. Similar to the spectra with singly and doubly charged coincidences no substructures are visible in the broad structure from 18 eV to 40 eV. A projection to the delay axis in the high energy part between 40 eV and 60 eV results in an autocorrelation trace similar to figure 3.4 in section 3.

4.2.1.2 Modeling and discussion

The results of the simulation of the dissociation of the molecules are illustrated in figure 4.4. In section (a) the modeling of the singly charged ion coincidences emerging from N_2^+ states as probe states can be seen. The single lower dissociative curve emerging from population and propagation in $N_2^+ 2^2\Sigma_g$ below the lower edge is nicely reproducing the separated dissociative curve at lower energies. The straight lines come from non-probed molecules and therefore have no delay dependence except at very small delays and therefore internuclear distances, where the Coulomb-potential is deviating significantly from the real potential curves. They contribute to the large distribution described in 4.2.1.1 between 4 eV and 9 eV. For the two bands with larger energies no potentials were found. The slopes and energies are fitting perfectly to the experimental results.
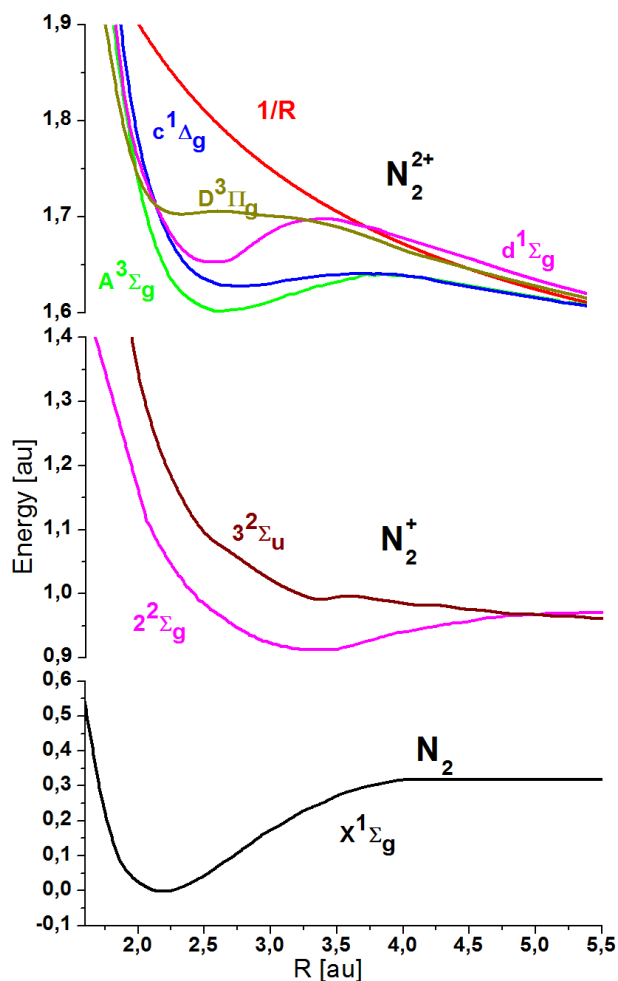
Figure 4.3: Potential curves of the observed N$_2$-states. Potentials taken from [102, 133, 136].

Except for the non-probed states the same structure can be seen in figure 4.4(b) and (c). It is interesting, that N$_2^+$2$^2\Sigma_g$ is always the separated dissociative curve with a KER lower than the rest of the distribution, while all the other pump states contribute to the lower edge of the broad band. The higher energies observed in this band could not be reproduced. It can be assumed, that these events come from bound states of the singly and doubly charged molecule. These could not be simulated, because of the absence of accurate potential curves for the higher ionized probing states as mentioned before.

4.2.2   Dissociative states of oxygen

4.2.2.1   Experimental results

Like in the discussion of the nitrogen results, three different charge states of the final state of the molecule are discussed. All of them are measured as a coincidence measurement and
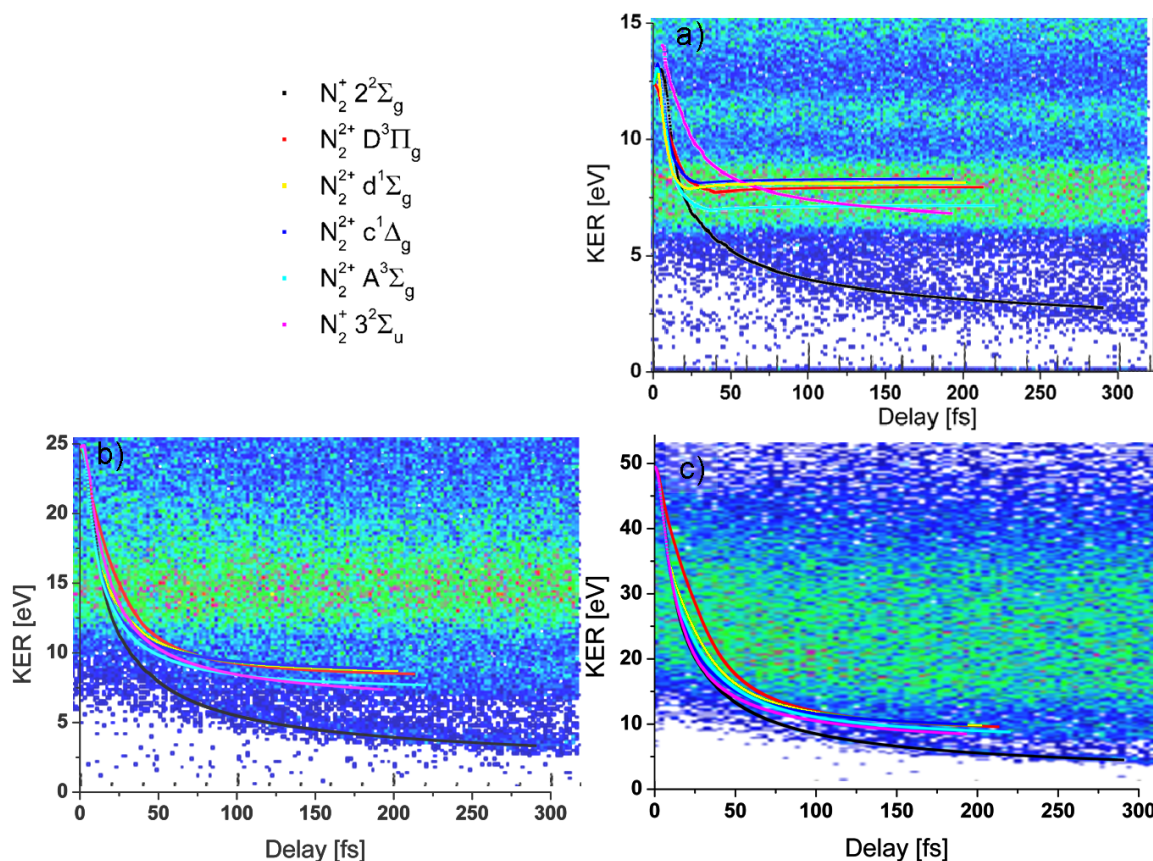
Figure 4.4: KER vs. delay spectra of in coincidence detected nitrogen ions measured with a photon energy of 46 eV. (a) N^+-N^+ coincidences; (b)N^+-N^{2+} coincidences; (c)N^{2+}-N^{2+} coincidences. The dissociative contributions mainly at low energies and some broad, time independent contributions emerging from non-probed molecular states are visible.

the KER is displayed as a function of delay.

In figure 4.5(a), the spectrum of singly charged coincidences emerging from O_2^+ is displayed. From this spectrum the data for the autoionization process described in chapter 5 was extracted. The spectral region in which the autoionization was found is located between 1 eV and 2.5 eV. At small delays the depletion is visible without further data processing. The large distribution of events between 5 eV and 15 eV emerges from bound O_2^+ states and from non-probed doubly charged molecular states. No dissociative features are visible in this spectrum.

In the unsymmetrical dissociation into doubly and singly charged ions out of the O_2^{3+} molecule in figure 4.5(b), again a broad distribution emerging from the probing of bound states is visible. At the bottom of the broad structure dissociative contributions can be seen. At small or no delay, the lowest energies measured are 5 eV while at a delay of 300 fs the observed events carry a KER down to 2 eV. The behavior of the lower part of the KER-vs.-delay spectrum can be explained by the probing of dissociative states of the
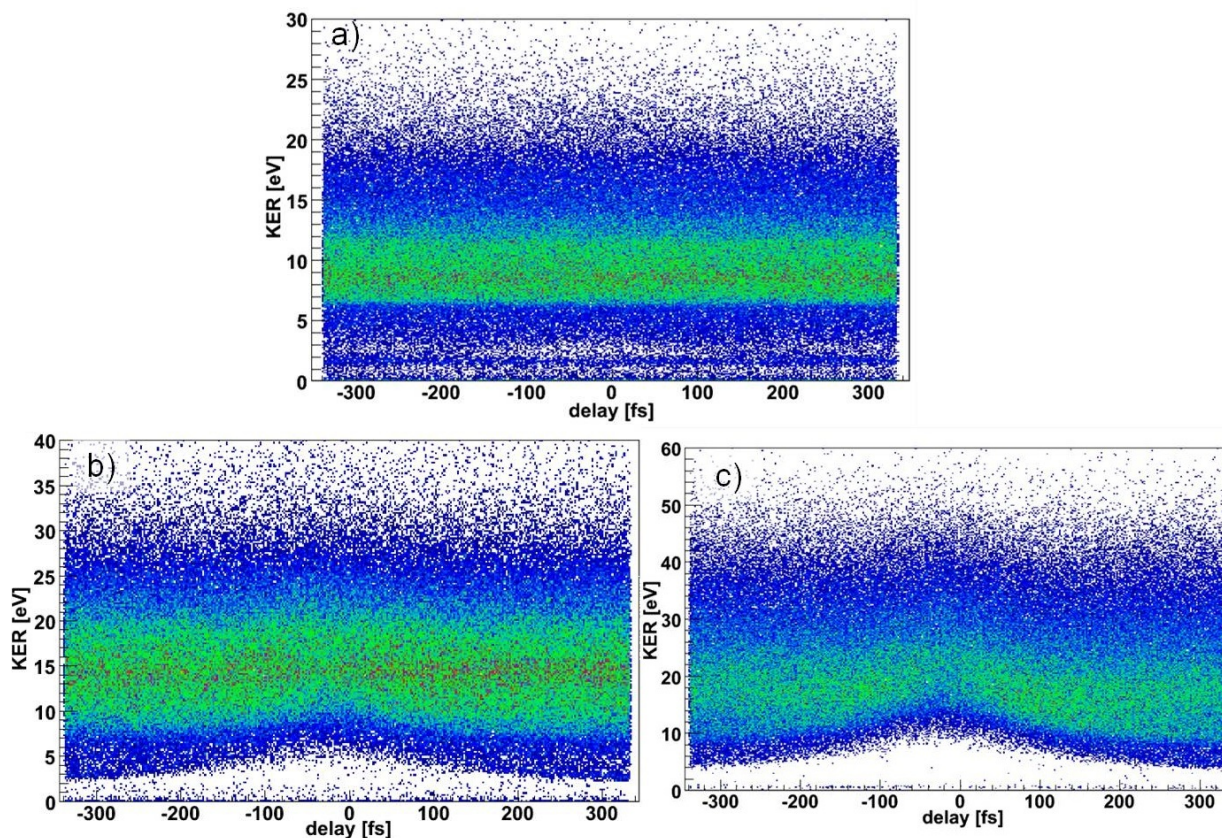
Figure 4.5: KER vs. delay spectra of in coincidence detected oxygen ions measured with a photon energy of 46 eV. (a) O$^+$-O$^+$ coincidences; (b)O$^+$-O^{2+} coincidences; (c)O^{2+}-O^{2+} coincidences. Qualitatively, the data is similar to the data recorded for N$_2$.

molecule.

In figure 4.5(c) the delay dependence of the KER in the Coulomb explosion of the fourfold ionized oxygen molecule is displayed. The main feature visible is a broad distribution of events with KERs between 5 eV and 40 eV. This large width of 35 eV can be explained by the slope of the O$_2^{4+}$ potential at small internuclear distances which is much larger than the slope of lower charge states. This leads to a large spreading of the kinetic energy. The lower edge of the broad contribution shows a dissociative behavior. Like in the doubly charged coincidences of nitrogen, an autocorrelation trace can be observed in the projection of the high energy events , which was already explained in chapter 3.

4.2.2.2 Modeling and discussion

For the singly charged coincidences no dissociative curves were visible. Therefore the bound oscillating states and non-probed O$_2^{2+}$ states are displayed in figure 4.7(a). It can be seen that the lower boundary of the broad structure in figure 4.5(a) at 7 eV can be simulated by the non-probed O$_2^{2+}W^3\Delta_u$ state. The upper boundary of this distribution at about 11
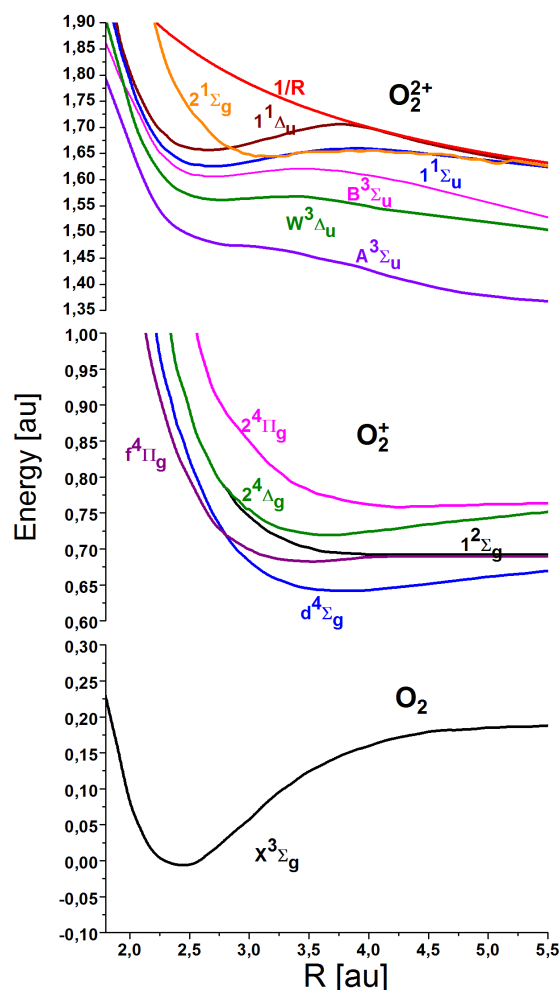
Figure 4.6: Potential curves of the relevant states for oxygen. Potentials taken from [102, 134, 135, 137].

eV can be described by the oscillation movement of three different O_2^{2+} states which get probed without further ionization into the 1/r Coulomb-potential. Unfortunately these bound states are not very accurate because of the probe potential that overestimates the KER at small probe distances. This effect is getting stronger in the higher charge states making it impossible to obtain even plausible results. If however real probe potentials for the triple fold and fourfold ionized molecule would be available, these simulations would also be possible.

In the modeling of the KER vs. delay spectrum of the coincidences between singly and doubly charged ions in figure 4.4(b) and the double coincidences between doubly charged ions in figure 4.7(c) only the lower edge of the broad distribution could be modeled. The most significant feature is that the lowest and slightly separated dissociative band in 4.5(b) could not be reproduced. In contrast, for the fourfold ionized molecule the lower boundary is met in a very accurate way.

Legend: b, c

· O$_2^+$ 1$^1\Sigma_g$

· O$_2^{2+}$ A$^3\Sigma_u$

· O$_2^+$ f$^4\Sigma_g$

· O$_2^+$ d$^4\Sigma_g$

· O$_2^+$ 2$^4\Pi_g$

· O$_2^+$ 2$^4\Delta_g$

Legend: a

· O$_2^{2+}$ W$^3\Delta_u$

· O$_2^{2+}$ B$^3\Sigma_u$

· O$_2^{2+}$ 2$^3\Sigma_g$

· O$_2^{2+}$ 1$^1\Sigma_u$

· O$_2^{2+}$ 1$^1\Delta_u$
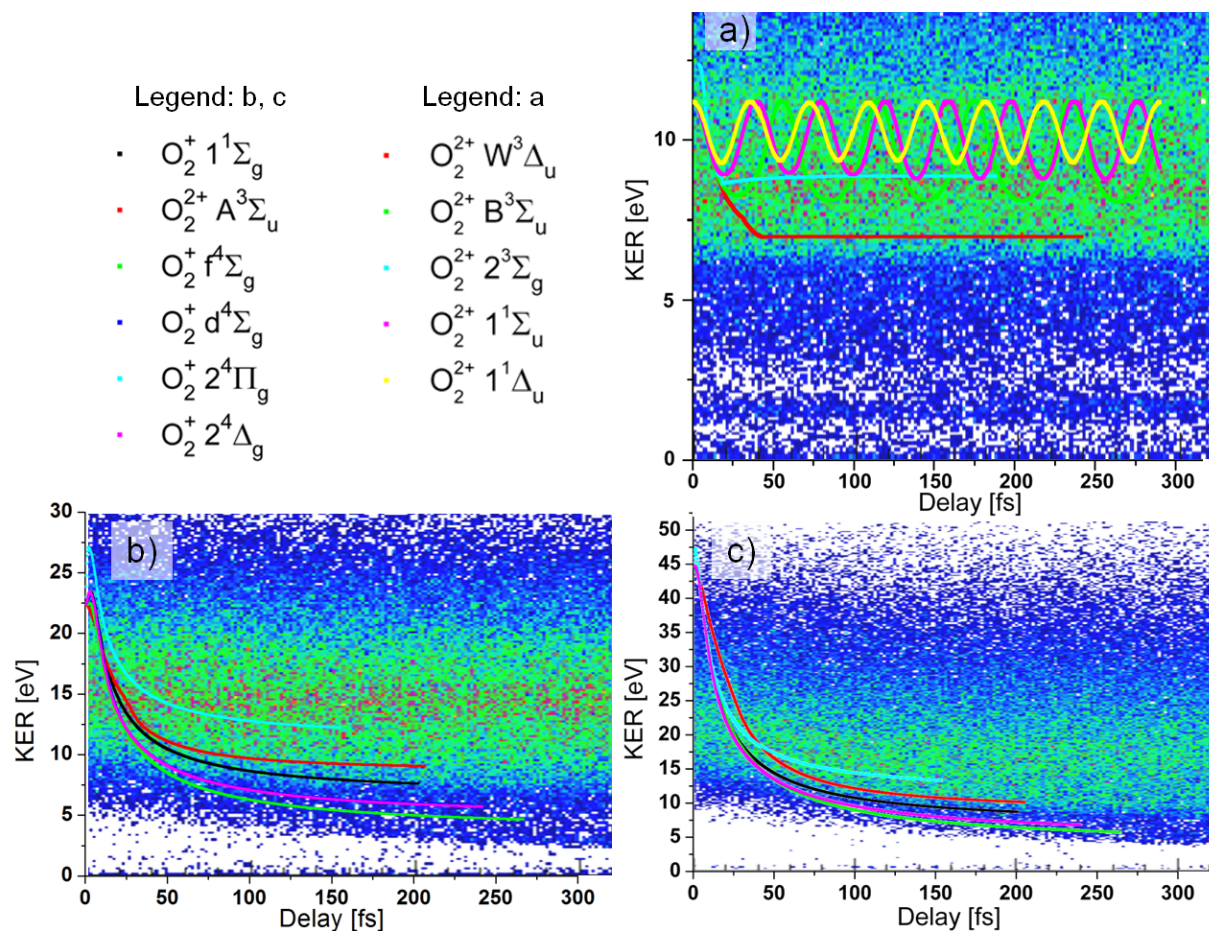
Figure 4.7: Simulated KER vs. delay spectra of in coincidence detected oxygen ions measured with a photon energy of 46 eV. (a) N$^+$-N$^+$; (b)N$^+$-N^{2+}; (c)N^{2+}-N^{2+}. Clear to see are the dissociative contributions mainly at low energies and some broad non time dependent contributions emerging from non-probed states and from bound oscillating molecules. Those can be identified by comparison to the calculations. Unfortunately the oscillatory behavior from the theoretical prediction displayed in (a) could not be traced in the measured data.

4.3 Conclusion

As shown in this chapter it is possible to reproduce the KER vs. delay spectra obtained in the XUV pump XUV probe experiments. With the appropriate backup on the theoretical side, it is possible to examine the dynamics of molecules in the most defined way. In this method the transitions between the states are one photon transitions and due to the absence of strong electric fields the potentials are practically unperturbed.

It was demonstrated that the dissociative contributions of the nitrogen and oxygen spectra can be simulated in good agreement. For the bound vibrational contributions this was not possible due to the lack of appropriate potential curves for triply and doubly

charged molecules. With additional experiments and more sophisticated simulations, that include modeling of the molecules to obtain potential curves, it would be possible to achieve a match between experiment and theory.

Chapter 5

Transient XUV depletion following fs XUV ionization of oxygen.

The XUV and X-ray ionization of an atom or molecule can lead to highly excited ionic states which subsequently decay or autoionize. In particular for molecules, autoionization is an important electronic many-body problem [138]. Even if first described by Maria Göpert-Mayer in 1931 (see ref. [1]), the description of such highly excited states of molecules embedded in electronic continua is difficult due to the mixing of the states. The wavefunction cannot be described in the Born-Oppenheimer representation. The formation and decay dynamics of inner-valence excited states and multiply excited states, i.e. the superexcited states in the inner-valence range, are not yet well understood and are an important subject for experimental and theoretical studies. So far, most studies on superexcited molecular ions have been performed in the frequency domain and real-time studies on the coupled electronic and nuclear dynamics of inner-valence excited ionic species have been sparse [70, 139]. Knowledge of the dynamics of superexcited states in the inner-valence range is needed also in other fields such as astrophysics, plasma physics and radiation chemistry since they play critical intermediate roles in a wide range of reactions [140].

5.1   The autoionization of molecular oxygen

The autoionization of molecular oxygen after XUV excitation was studied spectroscopically by Bolognesi *et al.* [141]. These authors investigated the single photon double ionization of O_2 for excitation energies between 32.5 eV and 41 eV, covering the range from the lowest $O^+ + O^+$ dissociation limit up to above the energy level of the ground state of O_2^{2+} [102]. According to Bolognesi *et al.*, the autoionization mechanism is best described by a two-step process, where first a near-zero-energy electron and an excited O_2^{+*} ion are produced, which subsequently dissociates into ionic and excited neutral oxygen fragments [141]. The autoionization of the latter finally yields double ionization with very distinct electron kinetic energies (with the main contributions at about 0.5 eV electron energy). Sandhu *et al.* recently performed a first time-resolved experiment, where the autoionization

of O_2 after XUV photoionization was monitored with femtosecond time-resolution [70]. They found that the autoionization follows a complex multi-step process and is prevented until large internuclear distances (ca. 30 Å) in the dissociation of the excited oxygen molecular ion are reached. The dynamics at early delay times and smaller internuclear distances, however, was obscured from observation in these studies as the laser-induced depletion of the superexcited state at the probe wavelength of 800 nm was energetically only feasible at large delays [70]. Shorter probe wavelengths in the VUV-XUV region are required in order to monitor the dynamics of superexcited molecular states all the way from their generation to their dissociation and decay. Of particular interest are the regions, where the molecular orbitals converge to atomic orbitals (as recently studied for the XUV-induced dissociation of ground state Br_2^+ [142]). There the internuclear-distance dependent transition from inner-valence excited states to the continuum states change significantly and therefore prevent the XUV-ionization of the excited oxygen molecule at large internuclear-distance were the autoionization takes place (see figure 5.1).
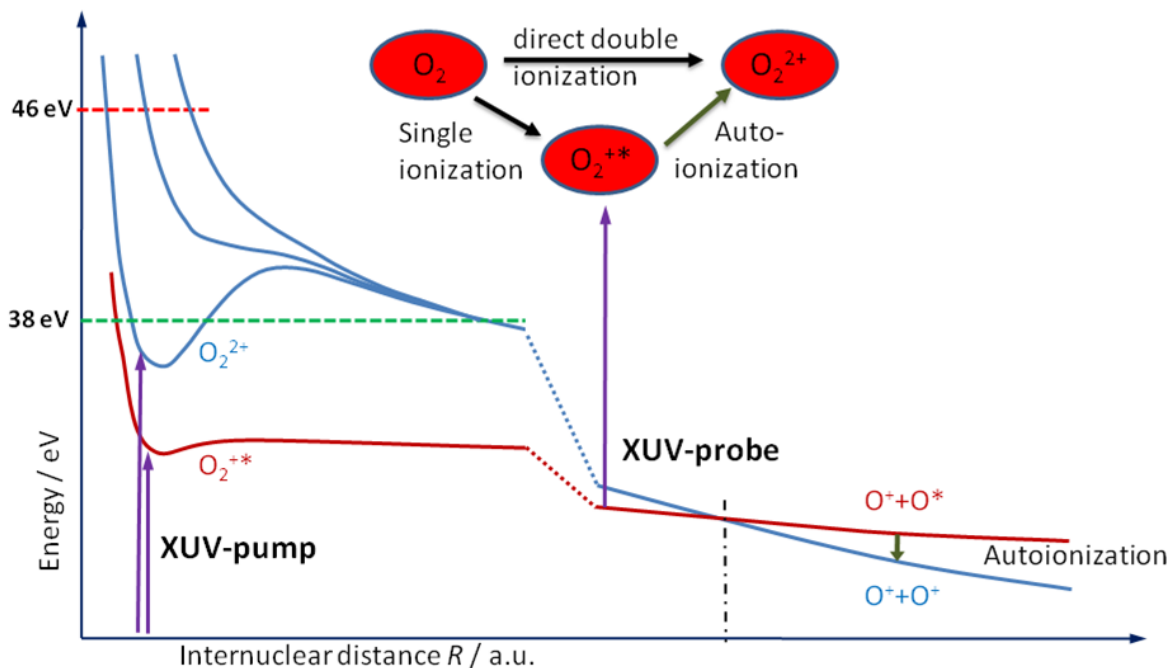
Figure 5.1: Schematics of the relevant potential energy curves of the molecular oxygen cation and dication in the XUV ionization of O_2 at 38 eV and 46 eV. The XUV pump-pulse populates either an inner-valence excited state or bound (for 38 eV) or dissociating (for 46 eV) states of the dication. The time-delayed XUV probe-pulse depletes population from the autoionizing inner-valence excited state.

5.2 Experimental results

To examine the transient XUV depletion following femtosecond XUV ionization of oxygen two experiments at FLASH were performed utilizing different XUV photon energies. The photon energies for the experiments were 38 eV for the one and 46 eV for the other. The FEL pulse was parted into a pump and a probe pulse with the split mirror setup described in section 2.3. These two pulses were then focused into a supersonic gas target and the ion fragments carrying the information about the reaction dynamics were detected with a reaction microscope as described in section 2.2.
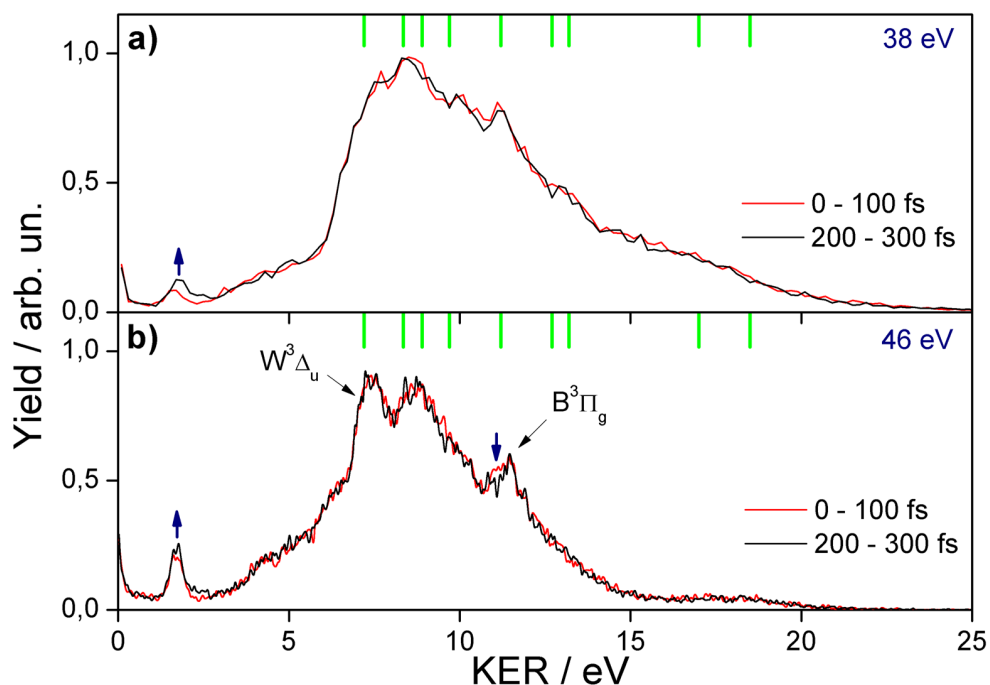

Figure 5.2: KER (kinetic energy release) spectra of coincident O^+ ions recorded after the ionization of O_2 at 38 eV (a) and 46 eV (b). The spectra were integrated over short and large delay ranges as indicated in the legends. KER contributions associated with the dissociation via O_2^{2+} states are indicated by the green bars, which are based on the peaks in the experimental data by Lundqvist *et al.* (from left to right: $W^3\Delta_u$, $B^3\Sigma_u^-$, $1^1\Delta_u^-$, $1^1\Delta_u$, $B^3\Pi_g$, $1^1\Pi_g$, $C^3\Pi_u$) [5]. Arrows mark significant changes with XUV pump - XUV probe delay time.

As seen in figure 5.1 two processes compete in the double ionization of molecular oxygen. When the KER spectrum is examined within two different delay windows (cf. figure 5.2), between 0 fs and 100 fs and between 200 fs and 300 fs, only very small differences can be identified. The most pronounced change, which is visible for both excitation energies, is the rise of the ion yield between 1 eV and 2.3 eV. As indicated in the figure, the large contribution between 5 eV and 15 eV consists of the peaks of multiple direct double ionization pathways and shows no large delay dependence. Some of the peaks are quite

prominent in the measurement with 46 eV, however, the peaks are washed out with the smaller photon energy of 38 eV. This may be explained by the energy needed to reach the states contributing here. With a photon energy of 46 eV the doubly charged states can be accessed by one photon, while at least two photons are required with 38 eV.

In the contribution of the KER spectrum between 5 and 15 eV a small delay dependence at about 11 eV is visible for an excitation energy of 46 eV. This contribution can be assigned to the $^3B\Pi_g$ state of O_2^{2+}. The delay dependence of the contribution between 6 and 16 eV is compared to the dynamics of the small peak around 2 eV in figure 5.3. An exponential fit is made to the dynamics between 6 and 16 eV and revealed a decay with a time constant of (158 ± 57) fs. The exponential fit of the ion yield with a KER between 1 eV and 2.3 eV shows a time constant of (159 ± 46) fs. These results are in a perfect agreement. Sandhu *et al.* found a decay time of "below 300 fs". It was defined as finding no significant contribution of low energy electrons from the autoionizing state. With a time constant of 158 fs as seen in figure 5.3 after 300 fs 85 % are decayed. This is in perfect agreement with the findings of Sandhu *et al.* [70]. Unfortunately, no dynamic changes for the O^+ ion yield from the $^3B\Pi_g$ state of O_2^{2+} were observed at a photon energy of 38 eV (see fig. 5.2).
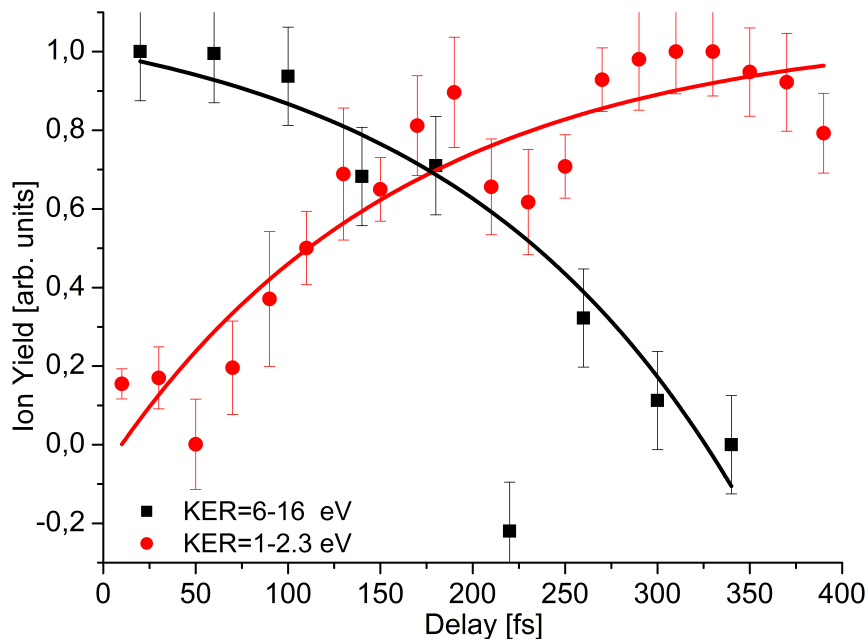
Figure 5.3: Comparison of the dynamics observed for coincident O^+ ions at a photon energy of 46 eV within two different KER regions that are indicated in the legend. The solid lines are exponential fits to the KER data. Both show a time constant of 158 fs in an exponential fit to the data.

The peak at 2 eV is assigned to an autoionizing excited state of O_2^+ based on the arguments below. A peak at a similar energy has been observed in earlier non time-resolved XUV studies on O_2. Johnsson *et al.* performed studies at FLASH at 44.45 eV and similar intensities using velocity-map imaging [143]. A peak at 1.93 eV in their studies

was assigned to the channel:

$$O_2 + h\nu_{\mathrm{XUV}} \to O_2^{+*} + e^- \to O^+ + O^* + e^- \tag{5.1}$$
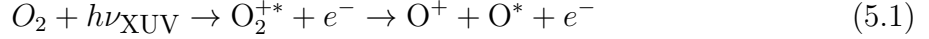
with a subsequent autoionization step yielding a second O^+ ion:

$$O^* \to O^+ + 2 \cdot e^- \tag{5.2}$$

The O_2^{+*} state was identified as the $c^4\Sigma_u^-$ state by these authors [143]. Lu *et al.* performed synchrotron ionization studies on O_2 with undispersed XUV light (up to a maximum of 60 eV) and identified a peak in the O^+ spectrum at 1.82 eV, which they also ascribed to an autoionization channel [144]. Lu *et al.* identified two O_2^+ states, the $c^4\Sigma_u^-$ and the $B^2\Sigma_g^-$ states, to be responsible for a contribution at this KER [144]. Based on the earlier work described above, we assign the contribution at around 2 eV in the coincident O^+ spectrum to an autoionization channel. In order to identify the autoionizing O_2^{+*} state and perform dynamic simulations on the superexcited state, calculations of the respective autoionizing states in collaboration with Mathias Nest and Armin Scrinzi are attempted. These calculations have, however, not converged yet, such that they could not be included in this thesis.
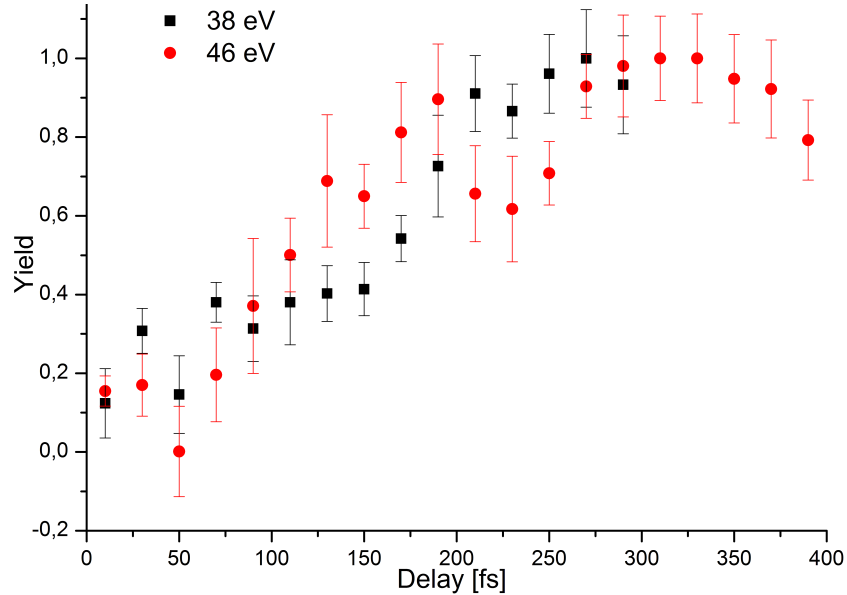
Figure 5.4: XUV depletion dynamics observed for coincident O^+ ions at KERs between 1 and 2.3 eV after femtosecond XUV ionization of O_2 at 38 eV and 46 eV. The pump and probe wavelengths are identical.

When the delay dependence of the autoionization peak of the two different measurements at photon energies of 38 eV and 46 eV are compared, after subtraction of a background (which is likely due to direct double ionization as it significantly increases with 46 eV) the curves look similar (cf. figure 5.4).

5.3   Conclusion

In this chapter, the transient XUV depletion dynamics of O_2 following XUV photoionization was studied using a pump-probe approach. The analysis of the experimental results indicates that the autoionization dynamics of a superexcited molecular ion has been measured. Further theoretical analysis is needed to understand the data in detail and attempt a simulation of the experimental traces recorded for photon energies of 38 eV and 46 eV. This autoionization process of oxygen is interesting for the understanding of such processes in the ionosphere of the earth where high energetic photons are absorbed by oxygen and nitrogen molecules. To understand and model these processes, these first measurements may serve as a reference to test theoretical predictions of the inner valence ionization of oxygen molecules and autoionization processes. But unfortunately the modeling for complex molecules as oxygen is still a challenging task.

Chapter 6

Two-photon double ionization of deuterium

The interaction of two photons with two electrons of an atom or molecule resulting in ionization two-photon double ionization (TPDI) is among the most fundamental nonlinear processes in atomic [28, 34, 37, 52, 55–57, 145, 146] and molecular [45, 147–149] physics. One can consider the TPDI as a benchmark process to test nonlinear theories and to investigate electron-electron correlations in atoms and the coupling between electronic and nuclear motion in molecules beyond the Born-Oppenheimer approximation (BOA).

Initiated by experiments that recently became possible using intense high harmonic radiation (see, e.g., [28, 57, 147]) or ultra-bright, free electron laser (FEL) sources like the Free Electron Laser in Hamburg (FLASH) (see, e.g., [34, 37]) and also motivated by the problems with the prediction of the helium double ionization, theoretical interest in TPDI has grown significantly (see. e.g., [52, 55, 56, 145] and references therein). Even recent publications [148, 149] employ the fixed nuclei approximation, due to the extreme computational requirements.

6.1 Tracing direct and sequential two-photon double ionization in the XUV regime with femtosecond pulses.

In the scheme illustrated in figure 6.1, the two different basic TPDI pathways that have been discussed in the literature for the D_2 molecule can be seen. In the "sequential ionization" (SI) the photons (purple arrows) are assumed to be absorbed in two steps via an intermediate stationary state of the ion (assumed to be the $1s\sigma_g$ ground state of D_2^+). In a later measurement they were traced in time as indicated by the horizontal arrow (see section 6.2). For direct or "non-sequential ionization" (NSI) both photons are absorbed simultaneously through a virtual intermediate state as denoted by the left vertical arrows. Although great theoretical efforts were made, questions on the direct ionization of the two

helium electrons by two photons remain unclear. Even on the level of total cross sections the debate has not been settled [145].
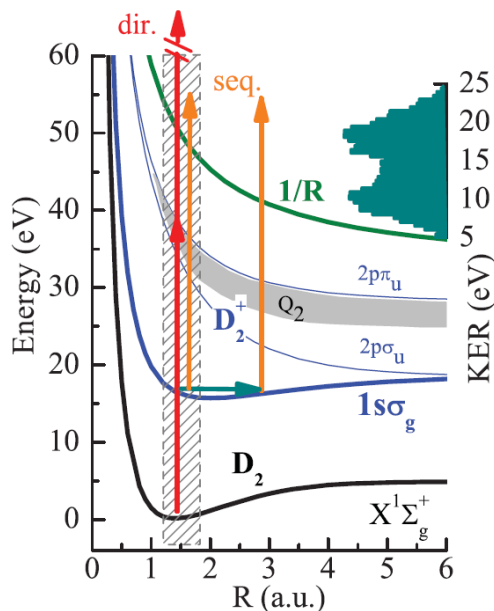

Figure 6.1: Illustration of the dominant dissociative pathways for single and double ionization of D_2 and experimental KER (Kinetic Energy Release) spectrum for coincident $D^+ + D^+$ fragments created by TPDI via direct and sequential pathways. Depending on the time (horizontal arrow) when the second photon is absorbed after single ionization, the repulsive $1/R$ curve is populated at different R, leading to time-dependent KERs and allowing for the separation of SI and NSI pathways. The solid gray band indicates doubly excited states Q2 in Σ and Π symmetries. The Franck-Condon regime is indicated as a vertical shaded band. (Figure taken from ref. [91])

Since either the statistical significance was weak or, for experiments performed at FLASH, the intensity of the XUV pulse is uncertain due to the random time structure of the pulses (see section 3), such a measurement was not performed before. Additionally, in cases where both processes, SI and NSI, are energetically possible, it was not feasible to distinguish them.

To understand the various one-photon absorption processes measurements were performed at FLASH with a reaction microscope as described in section 2.2 using $\sim$30 fs pulses with a peak intensity of $I \cong 10^{13} - 10^{14}$ W/cm^2 and a photon energy of 38 ± 0.5 eV. The KER spectrum for non-coincident D^+ atoms, emerging from dissociative channels of D_2^+, is shown in figure 6.2 together with theoretical ab initio results using the time-dependent method of [150]. Only fragments emitted perpendicular to the polarization axis ($\Theta = 90° \pm 5°$) are displayed. In good agreement with the calculations and previous measurements for one-photon single ionization [151, 152] all relevant fragmentation paths like ground-state dissociation (maximum at $E_{KER} = 0$), dissociation via the $2p\pi_u$ channel
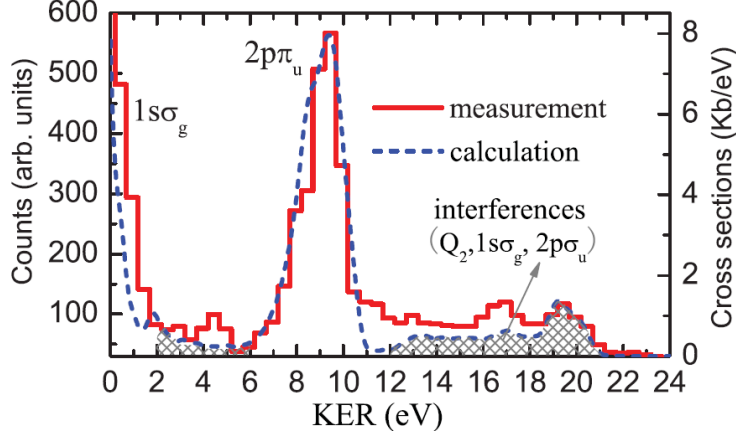
Figure 6.2: KER spectrum of non-coincident D^+ fragments taken under an emission angle of $90° \pm 5°$ with respect to the light polarization axis (i.e., for final Π symmetry). (Picture out of ref. [91])

($E_{KER} \approx 9$ eV), and contributions and interferences involving the decay of doubly excited (Q2) states [153], are very well resolved (figure 6.2). Theory and experiment showed that the D_2^+ $1s\sigma_g$ ground state is occupied with a probability of 95 %. For the calculations of our collaborators from the University of Madrid, an exclusive occupation if this state was assumed for the first ionization step.

The total SI probability P_{SI}^{KER} to a specific KER was calculated as a sum over products of one-electron probabilities $P_{SI}^{KER} = \Sigma_\nu P_1^\nu \cdot P_2^{\nu, \, KER}$ associated with the two steps (1) $D_2(\nu_i = 0) \rightarrow D_2^+(\nu) + e$ and (2) $D_2^+(\nu) \rightarrow D^+ + D^+ + e$, where, in the BOA,

$$P_1^\nu \propto \left| \int \langle \Psi_i^{D_2}(r, R) | D | \Psi_{el}^{D_2^+ (1s\sigma_g)+e}(r, R) \rangle_r \times \chi_{\nu_i=0}^{D_2}(R) \chi_\nu^{D_2^+ (1s\sigma_g)}(R) \, dR \right|^2$$

$$P_2^{\nu, KER} \propto \left| \int \langle \Psi_{el}^{D_2^+ (1s\sigma_g)+e}(r, R) | D | \Psi_{el'}^{D^+ + D^+ + e}(r, R) \rangle_r \times \chi_\nu^{D_2^+ (1s\sigma_g)}(R) \chi_{KER}^{D^+ + D^+}(R) \, dR \right|^2$$

(6.1)

D is the transition operator for one-photon absorption, $\Psi_i^{D_2}$ is the initial electronic state of D_2, $\Psi_{el}^{D_2^+ (1s\sigma)+e}$ is the electronic continuum state of D_2^+ produced after the absorption of the first photon, $\Psi_{el}^{D^+ + D^+ + e}$ is the electronic continuum state after the absorption of the second photon; $\chi_{\nu_i=0}^{D_2}$, $\chi_\nu^{D_2^+ (1s\sigma_g)}$, and $\chi_{KER}^{D^+ + D^+}$ are the associated vibrational (dissociative) states; r denotes all electronic coordinates and integration over those is indicated using the usual bracket notation. Integration with respect to the internuclear distance R is explicitly indicated. In this model it is assumes that the two electrons are emitted independently from each other and, consequently, that the time between the two ionization events is infinite (which is reasonable since the pulse duration is larger than a round-trip time of any vibrational wave packet that might be created in the first step). In order to obtain

deeper insight into the process these expressions have been evaluated by either assuming that the dipole matrix elements do not change with R (what will later be called the Franck-Condon approximation, FCA) or taking explicitly into account their R dependence (the non-FCA).

Similarly, one could also calculate the NSI probability as

$$P_{\mathrm{NSI}}^{\mathrm{KER}} \left| \int \langle \Psi_i^{\mathrm{D_2}}(r,R)|D^{(2)}|\Psi_{el'}^{\mathrm{D^+ + D^+ + 2e}}(r,R)\rangle_r \times \chi_{\nu_i=0}^{\mathrm{D_2}}(R)\chi_{\mathrm{KER}}^{\mathrm{D^+ + D^+}}(R) \ dR \right|^2 \qquad (6.2)$$

where $D^{(2)}$ is the transition operator for the two-photon absorption. Since evaluation of the R dependence of the integral involving the latter operator is prohibitively expensive [149], this probability has been exclusively evaluated within the FCA. Since the calculations do not provide the absolute values of the SI and NSI probabilities, the total probability has been obtained by fitting $aP_{\mathrm{SI}}^{\mathrm{KER}} + bP_{\mathrm{SI}}^{\mathrm{KER}}$ (where the ratio a/b represents one effective free parameter independent of the KER) to the experimental KER spectra in 6.3. In doing so it is assumed that the SI and NSI processes do not interfere.
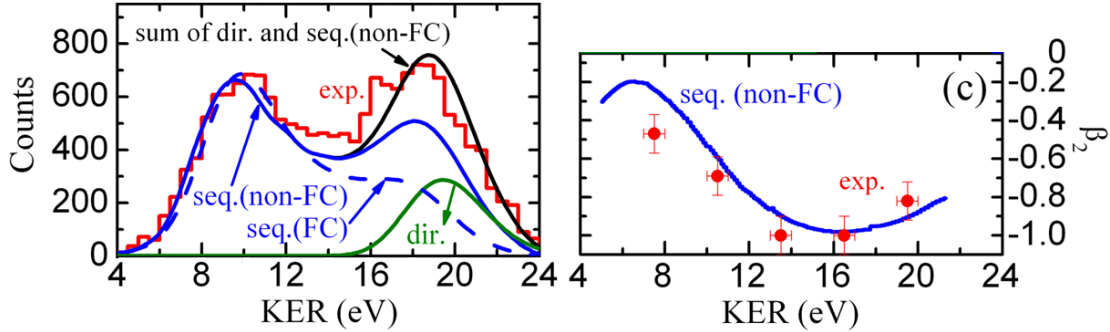
Figure 6.3: FIAD and KER spectra for coincident $\mathrm{D^+ + D^+}$ fragments. Left: Experimental KER spectrum compared to calculations in the non-FCA and FCA; Right: Experimental and theoretical β_2 values as a function of the KER.

Two clear peaks are visible in the experimental data, one at high KERs between about 16 and 24 eV and a low-energy part extending from $\sim$5 to $\sim$15 eV. As illustrated in figure 6.1, this KER range corresponds to internuclear distances R between $\sim$1.3 a.u., the minimum value within the FC regime, and $R \sim$6 a.u., which can only be reached via ground-state dissociation of the $1s\sigma_g$ states. As discussed before, effects $<$5% were neglected that might be due to excitation into the Q_2 band as well as to the $2p\pi_u$ and the $2p\sigma_u$ states. Also plotted in figure 6.3 right are the results of our model calculations for the non-FC approximation (i.e., by taking realistic R-dependent ionization probabilities into account as well as for the FCA, assuming constant ionization cross sections as a function of R). It can be seen in figure 6.3 that neither the SI nor the NSI, when considered separately, can reproduce the observed peaks and their relative heights. For the intensities used in the experiment, the correct relative heights can only be obtained if both processes

contribute in the high-energy region of the KER spectrum, irrespective of whether they interfere or not. In both the non-FC and FC approximations, the sequential ionization contributes strongly to the low-energy part, displaying a clear peak that largely coincides with the experimental one. Some differences between the two calculations are visible at higher KERs, where the flux obtained within the non-FCA is slightly larger and located at somewhat higher energies than for the FCA. On the basis of the calculations and by inspecting the contributions of different vibrational levels to the spectra (not shown here) an interpretation of our observations is straightforward. It was found that the largest contribution to SI originates from the $\nu = 2$ state followed by those with $\nu = 1$ and $\nu = 3$, just reflecting the initial distribution after the absorption of the first photon. The slightly different KER position of the low-energy maximum in the two calculations indicates small differences in the population of vibrational states due to the R-dependent ionization probability in the non-FCA.

Thus, the calculations lead to a straightforward interpretation of the low-energy peak: a set of vibrational levels are excited on the $1s\sigma_g$ potential curve of the D_2^+ molecule after absorption of the first photon. Sequentially, if infinite time in the calculations is assumed, a second photon is absorbed, projecting the corresponding R distribution onto the repulsive $1/R$ potential curve such that the two maxima simply represent the inner and outer turning points of the corresponding vibrational states where the time-averaged density distribution of the states is largest. Since ionization at small R is less likely (because the FC overlap between intermediate and final vibrational states is smaller near the inner classical turning point), the maximum at the high-energy part of the KER spectrum is slightly lower. As the length of the FEL pulse is estimated to be about 30 fs and a wave packet launched in the FC regime would travel to the outer turning point within about 10-12 fs, the time-independent approach, under the assumption that all R on the $1s\sigma_g$ surface are equally populated, seems to be well justified.

It is very obvious that sequential ionization alone cannot explain the experimental high-energy peak in the KER spectrum. To explain this contribution at $E_{KER} = 18.5$ eV, direct TPDI, where the nuclear wave packet has not moved significantly, is needed in both model calculations [dash-dotted line in figure 6.3 right]. This provides clear evidence that experimentally both the direct and the sequential TPDI channels simultaneously can be observed. Also between both pathways can be distinguished through an indirect temporal measurement exploiting the femtosecond nuclear motion. In particular, fragments with low KERs can only be created via the sequential absorption of two photons projecting the D_2^+ vibrational states created by the first photon onto the repulsive $1/R$ curve at large internuclear distances.

Several aspects have to be considered when the results of the model and the experiment are compared: (i) The present calculations add the contributions of both channels incoherently, thus possible interference between both channels is neglected. Similar interference effects were recently predicted to occur in three EUV-photon absorption processes [154]. (ii) The experimental pulse duration is limited to about two round trips of the vibrational wave packet that is launched by the absorption of the first photon such that time-dependent effects, not yet implemented into the calculations, might occur. (iii) Additional experimen-

tal effects cannot be excluded due to the essentially unknown pulse structure of the FEL, which could change even during a single experimental campaign. Measuring the KER distributions in two different beam times always two peaks were found, but with different relative weights, most likely due to the different actual pulse durations and peak intensities achieved.

Also the fragment-ion angular distribution was examined. These can be characterized by a multipole expansion, in terms of Legendre polynomials, $\frac{d\sigma}{d\Omega} = \frac{\sigma_0}{4\pi}[1+\Sigma_{i=1,...,n}\beta_{2i}P_{2i}(cos\theta)]$, where n is the number of absorbed photons, β_{2i} are the asymmetry parameters and $\cos(\theta)$ is the fragment's emission angle relative to the light polarization axis. FIADs for the co-incident $D^+ + D^+$ fragments have been extracted at selected KERs by integrating events within ± 1.5 eV around the respective central value. The corresponding experimental β_2 values from fits together with calculations are presented in figure 6.3, right. The latter have been obtained within the sequential model by assuming a random orientation of the $D_2^+(\nu)$ produced after the first ionization step, that is, $\beta_2 = \Sigma_\nu P_1^\nu \beta_2(\nu)/\Sigma_\nu P_1^\nu$,where $\beta_2(\nu)$ is the asymmetry parameter of D_2^+ in the vibrational states ν. Good agreement between theory and experiment is found. Surprisingly, the agreement is also good at high KER where direct ionization, not taken into account in the present calculations, significantly contributes.

6.2   Investigating two-photon double ionization of deuterium by XUV-pump-XUV-probe experiments

The realization of a femtosecond XUV-pump-XUV-probe scheme opens a new chapter in ultrafast science by exploiting the huge flux of about 10^{12} photons/pulse of FLASH. We trace in real time the femtosecond nuclear wave-packet dynamics in a prototype system, the $1s\sigma_g$ ground state of D_2^+, populated with about 95% by absorption of one photon (38 eV) from the pump pulse as depicted in figure 6.1. The dynamics is captured by the time-delayed XUV probe pulse which "sequentially" ionizes D_2^+ and results in its Coulomb explosion with the kinetic energy release of the fragments, both measured in the reaction microscope, and is proportional to the inverse of the internuclear distance at the instant of the second ionization. The experimental conditions were about the same as before.

The dominant fragmentation pathways for direct and sequential TPDI of D_2 are illustrated in figure 6.1 and both are expected to contribute with comparable amplitude in each individual pulse (pump as well as probe) to the total double-ionization yield at the present intensities. In the case of sequential ionization a nuclear wave-packet in $D_2^+(1s\sigma_g)$ is launched due to ionization by the first photon and then, either within the same pulse or induced by the time-delayed replica, projected onto the repulsive $D^+ + D^+$ Coulomb potential after absorption of the second photon. According to the reflection principle, and neglecting the bound-state nuclear kinetic energies, the R-dependent shape of the wave-packet is converted into KER that is released in the Coulomb explosion of the deuterons. Accordingly, the KER spectrum carries information about the time delay between the two

subsequent photoabsorption events or, turning it around, information about the actual shape of the molecular wave-packet at the instant of the second ionization step. Considering the fact that D_2^+ may get ionized at any R, ranging from the inner up to the outer classical turning point of the wave-packet in the $D_2^+(1s\sigma_g)$ potential, the corresponding KER values are between 6 and 20 eV. In the case of direct TPDI, where the molecule is promoted directly from the neutral ground state into the double-ionization continuum by instantaneous absorption of two photons via intermediate virtual states, the observed KER spectrum exhibits a peak at 18 eV, corresponding to the equilibrium internuclear distance R_e of neutral D_2. This interpretation is in agreement with the single excitation pulse measurement shown in section 6.1.
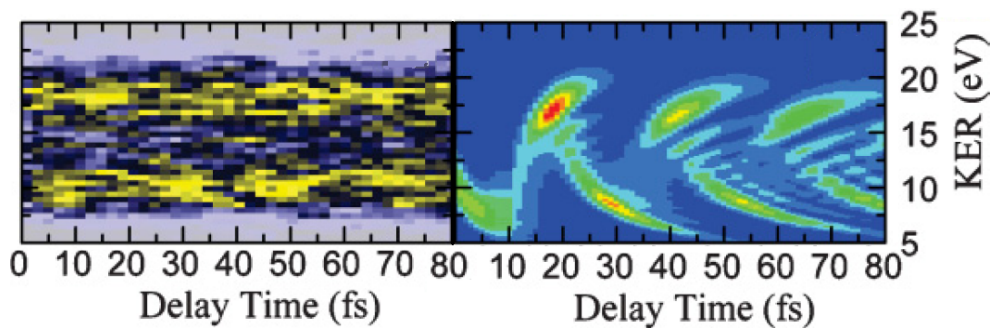

Figure 6.4: Left: Density plot for the experimental KER spectrum of coincident D^+ + D^+ fragments as a function of delay time up to 80 fs. Right: The same as left, but for theoretical results. (figure from [97])

The KER spectrum measured with the pump-probe setup is shown in figure 6.4 on the left as a function of the time delay between both FEL pulses. Two pronounced horizontal bands around $E_{KER} \cong 18$ and 10 eV are observed which can be attributed to ionization of D_2^+ at the inner or outer classical turning points, respectively. Since the absorption of one photon from the pump pulse launches a D_2^+ nuclear wave-packet, which is then probed during the time-delayed probe pulse by further ionization, a time-dependent oscillatory behavior for the KER distribution is expected. The result of a projection of the two-dimensional data in figure 6.4 over the low KER band (from 6 to 12 eV) onto the time axis is shown in the lower part of figure 6.5. The periodic maxima occur whenever the probe pulse meets the vibrating molecule at large R. Consequently, by varying the delay time the D_2^+ vibrational wave-packet as well as sequential double ionization is probed at different instants of time. A less pronounced, barely visible oscillation is observed in the high KER band for a projection of all events with 15 eV $< E_{KER} <$ 21 eV (see upper part of figure 6.5). To some extent this is expected because at small R, therefore high KER, the contribution from the direct double-ionization process is largest and the corresponding probability does not oscillate with delay time because no vibrational wave-packet is launched in the $1s\sigma_g$ state. Thus, among other reasons, it might be the larger time-independent background that dilutes the expected oscillations in the high KER range.

In general, the oscillation (amplitude $\sim$20 counts) occurs on top of a significant back-
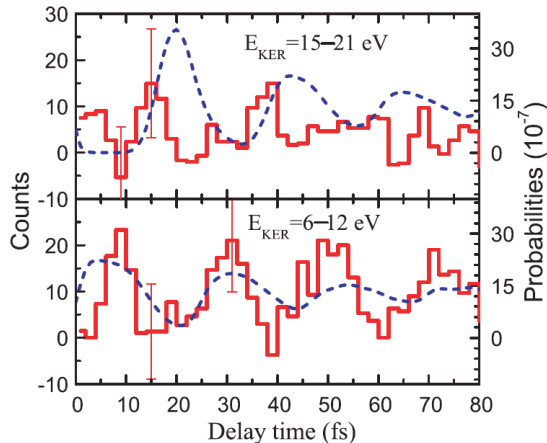
Figure 6.5: Pump-probe delay-time dependence of ion yields in different KER regimes as indicated in the figure, after proper background subtraction, as described in the text. Dashed lines: theoretical ionization probabilities (right ordinate) for the corresponding KER ranges. (figure from [97])

ground of about 100 counts (already subtracted in figure 6.5), consisting essentially of three contributions. (i) The FEL pump pulse is strong enough to generate direct as well as sequential TPDI at high KER. At the same time the pulse duration is long enough, $\sim$30 fs, to produce one-pulse sequential TPDI contributions at low KER as well. (ii) The same is true for the probe pulse alone, even though this contribution should be negligibly small for an ideal overlap between both pulses since the pump pulse will ionize all molecules in its focus with a probability close to unity. (iii) Because the full width at half maximum (FWHM) of the envelope of many individual self-amplified spontaneous emission (SASE) pulses has been estimated (and measured [125]) to be $\sim$30 fs, which means longer than the round-trip time of the D_2^+ wave-packet, a pump-probe experiment should deliver a mostly flat, time-independent behavior.

The question why the $\sim$20 fs motion of nuclear wave-packets can be mapped at all, even observing structures as sharp as $\sim$7 fs, can be answered in light of several recent measurements (see ref. [125, 126] and also section 3) on the single-shot characteristics and the coherence length of the SASE pulses, showing that they contain single spikes as short as <7 fs (limited by the experimental resolution). Nonlinear autocorrelation measurements for multiple ionization with our split-mirror setup, where the same pulse is used for pump and probe and, thus, the width of the most prominent peak of the spiky internal pulse structure sets the limit for the achievable time resolution, deliver signals shorter than 7 fs (see section 3).

In light of these results, the KER for sequential double ionization of D_2 as a function of the pump-probe delay time was calculated by solving the time-dependent Schrödinger equation (TDSE) separately for the two ionization steps using 10-fs-cosine square-shaped XUV pulses. Single ionization by the pump pulse ($D_2 \Rightarrow D_2^+$) is treated essentially without

approximations by including all electronic and vibrational (dissociative) degrees of freedom (see, e.g., [155] and references therein). In particular, the electron-electron interaction is included. The time integration is stopped just at the end of the pump pulse and the resulting nuclear wave-packet, freely propagated in time until the onset of the probe pulse, serves as a starting point for the calculation of the second ionization step $(D_2^+ \Rightarrow D^+ + D^+)$, in which the presence of the first ejected electron is ignored. The corresponding one-electron TDSE is solved again essentially without approximations by using a method similar to that described in [156] (in particular, the R-dependent photoionization probability is taken into account). This model is expected to yield an appropriate description of sequential (pump-probe) double ionization. The delay-time-dependent KER spectrum calculated for 10^{12} W/cm^2 at 38 eV clearly shows the wave-packet motion over the whole KER range (see figure 6.4, right), closely resembling the temporal and spatial evolution of the $D_2^+(1s\sigma_g)$ vibrational wave-packet that is created after the pump pulse. Results obtained with slightly longer pulses, containing spikes such as those of the SASE pulses, are very similar. The fact that the oscillatory structure in the theoretical KER spectrum is considerably more pronounced than in the experiment is a result of the discussed single pulse-induced double-ionization processes that are not included in theory. At high KER in particular the direct TPDI gives rise to a time-independent background contribution.

In order to enable a quantitative comparison with theory, the background contributions were subtracted from the experimental data for low (6-12 eV) and high (15-21 eV) KER contributions by exploiting the time-dependent wave-packet motion. For times where the wave-packet is at the inner (about 16 fs and 38 fs) or outer (about 9 fs and 30 fs) turning point, respectively, the background contributions for the high- and low-energy KER parts can be generated separately and have been subtracted for the respective time-dependent traces shown in figure 6.5. Comparisons with the equivalent theoretical yields are in good agreement, thus demonstrating that the model has captured the essential physics. A Fourier analysis of the low-energy KER oscillations, where slightly better statistical significance could be achieved, showed a period of 22 ± 4 fs and 23.8 fs for experiment and theory, respectively, which is in very good agreement with the expected 22-fs oscillation period of a freely propagating nuclear wave-packet in $D_2^+(1s\sigma_g)$ [157].

The wave-packet motion might provide the key to unambiguously determine the cross section for direct TPDI in the future. Using slightly reduced photon energies ($\sim$30 eV) sequential TPDI is not allowed at small R (see figure 6.1). Then, any experimental observation of high KER events at times (e.g., at 30 fs) where the wave-packet is at large R, therefore small KER, must be entirely due to direct TPDI induced by the pump pulse and/or the probe pulse. The ratio of the integrated direct TPDI signal, the high KER events, to the sequential one, together with the theoretically available sequential TPDI probability, will allow to extract the direct TPDI cross section which is much more difficult to calculate and the subject of considerable interest for theory [69, 149]. This is true for not too intense pulses ($< 10^{13}$ W/cm^2) such that sequential three-photon processes do not significantly contribute. The method would profit from shorter pulses (< 10 fs) recently demonstrated at the Linac Coherent Light Source in the USA.

6.3   Conclusion

In summary, two-photon double ionization of D_2 at 38 eV photon energy has been explored by inspecting fragment angular distributions and kinetic energy releases in the $D^+ + D^+$ final channel. We demonstrate that the KER spectra encode the time in between the absorption of the two photons through the internal molecular dynamics, enabling us to distinguish between sequential and direct absorption pathways and therefore quantifying their relative contribution. Also the FIADs are inspected and show distinct differences for the SI and NSI, being in reasonable agreement with the theoretical prediction for sequential ionization.

Also a femtosecond XUV-pump XUV-probe experiment has been performed and time-dependent sequential two-photon double ionization has been explored. By measuring the KER via coincident $D^+ + D^+$ fragmentation detection, the $1s\sigma_g$ D_2^+ bound-state vibrational wave-packet, launched by ionization with the pump pulse, was imaged via its reflection on the Coulomb potential with the probe pulse. The motion of this wave-packet was traced with ¡10 fs time resolution. Comparison with sophisticated model calculations yields good overall agreement with the experimental delay-time-dependent KER spectrum and the observed vibrational period of 22 $\pm$4 fs.

Our XUV pump-probe scheme combined with many-particle imaging methods opens a variety of future possibilities: (i) Highly excited states, such as metastable dication states in N_2^{2+} or doubly excited D_2^{**}, can easily be reached within just one frequency-controlled XUV pump step. Moreover, light-induced conformational changes in molecules (e.g. isomerization) or investigations of the dynamics at conical intersections will become accessible. (ii) At high-enough photon energies, the nuclear wave-packet as a whole is projected from position (R) to momentum space allowing for its complete imaging, which is different from previous measurements with IR lasers where the wave-packet could not be traced at small R. (iii) Pump and probe steps are clean in the sense that they ideally involve one-photon absorption processes. (iv) Measuring the emitted electron in coincidence will allow time-dependent "imaging of molecules from within".

Chapter 7

Carrier-envelope-phase dependent experiments on atoms in strong near-infrared laser fields

The ionization mechanisms in the NIR differ strongly from the XUV ionization described in chapter 1.1. Especially when the intensity and therefore the strength of the fields are the same, the Keldysh parameter γ differs significantly. Therefore the ionization with NIR lasers has to be described in the field picture and cannot be handled in the photon picture as the XUV ionization.

In this chapter, measurements on the effects of the carrier-envelope phase (CEP) on the non-sequential double ionization (NSDI) of rare gas atoms are discussed. For this a stereo ATI (see section 7.2.2) for single-shot CEP-tagging has been implemented with a reaction microscope at the AS1 beamline in Garching. This allowed on the one hand longer acquisition times, as compared to CEP stabilization which always affects the stability of the laser system. On the other hand for measuring CEP-effects with a CEP stabilized laser system, the CEP is shifted by a pair of glass wedges by changing the dispersion of the beam path. This leads also to change of the pulse length and therefore of the peak intensity. This means the CEP and the peak intensity are correlated and as a result, the measurement of the CEP dependence of the ion yield is impaired. All this can be circumvented by measuring the random CEP of the laser system from shot to shot, together with the single-shot data acquisition of the reaction microscope allowing experiments with a detail that cannot be reached with other techniques.

The theory of the strong field ionization is introduced first. After that the setup used for the experiments is described before the experimental results are presented and discussed.

7.1   Mechanisms of the NIR ionization

7.1.1   Multi-Photon Single Ionization

The single photon single ionization has been presented in section 1.2. The multi-photon ionization, which is explained in the subsequent section, can be explained with the same description. Afterwards the ionization scheme of the tunneling ionization will be presented. The over-the-barrier ionization, that can be described classically, is introduced shortly in the end.

7.1.1.1   Above Threshold Ionization

The most striking consequences of multi-photon ionization are the discrete structures in electron spectra. While electrons with large energies where observed earlier, Agostini *et al.* [158] reported, for the first time, discrete electron energies which peak distances correlating exactly with the energy of a photon. This is yet another phenomenon that at first glance contradicts the intuition: An already ionized and therefore free electron absorbs further photons. In principle this process is forbidden by the momentum and energy conservation. But as long as the electron is not far away from the parent ion there is an interaction between them via the Coulomb field. This allows the absorption of further photons out of the light field and therefore the formation of discrete maxima in the energy spectrum of the photo electrons. Because more photons are absorbed than necessary to overbear the Coulomb threshold this process is called above threshold ionization (ATI) [159].
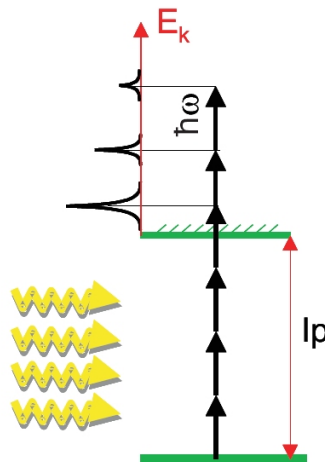

Figure 7.1: The principle of above threshold ionization. More photons are absorbed than necessary to overbear the ionization potential I_P. This leads to maxima in the electron spectrum with a distance of the photon energy $\hbar\omega$.

If the perturbation theory is applied to the ATI rates, with a simple extension of the

power law in formula 1.13, the absorption of s additional photons can be described.

$$w_n \propto I^{n+s}. \tag{7.1}$$

Accordingly it is expected, that the higher order ATI maxima vanish rapidly. But in the first experiments a discrepancy with the intensity dependence has become evident. This can be explained by the AC Stark shift of the bound states and the resulting channel closing [160]. Because the lowest states are nearly unaffected, a shift of the ionization potential of nearly U_P takes place. The ionized electron then carries the energy, E, given by:

$$E = (n + s)\,\hbar\omega - (I_P + U_P), \tag{7.2}$$

whereas I_P is standing for the unperturbed ionization potential. This leads to a blurring of the ATI peaks. In addition, in most experiments volume averaging, the integration over a wide intensity range in the focus, has to be taken into account and because of this the description is still not ideal.

7.1.1.2 Tunneling Ionization

In accordance to the correspondence principle [161], the laser field can be treated classically, if the number of the involved photons, and therefore the intensity, is high enough. This is given in good approximation for the case $\gamma \ll 1$. Because of this reason and because the magnetic field can be neglected (see section 7.1.2), the laser field can be described as a time-dependent electric field. This external electric field forms together with the Coulomb field of the atom a potential barrier. This barrier can be penetrated by the quantum mechanical effect of tunneling. The ionization rate through the potential barrier in a static field is growing exponentially with the field strength and has the form [162]:

$$w_{tunnel} \propto exp\left(-\frac{2\,(2I_P)^{3/2}}{3E}\right). \tag{7.3}$$

Because the height of the barrier scales with $I_P/E \propto I_P/\sqrt{I}$, equation 7.3 can be understood as the exponential decrease of the wave function under the barrier. This model is used in ADK theory that was postulated in 1986 by Ammosov, Delone and Krainov [163]. As one can see in figure 7.3, single ionization rates can be described very well (1), but the model deviates at lower intensities where the multi-photon ionization picture is valid.

Besides their different intensity dependence, multi-photon ionization and tunneling ionization show different dependencies of the wavelength, respectively frequency, of the light. While multi-photon ionization is enhanced if an atomic resonance is excited, the tunneling rate is basically independent from the frequency. In the tunneling regime the discrete structures in the ATI photoelectron spectra vanish and for the case of linear polarized light a continuous energy distribution is visible. It changes its characteristics at an energy of $2\,U_P$ considerably (see figure 7.2). Subsequently, a plateau can be observed that reaches up to approximately $10\,U_P$. From the distinct change in the characteristics at $2\,U_P$ the intensity can be determined by using formula 1.3.
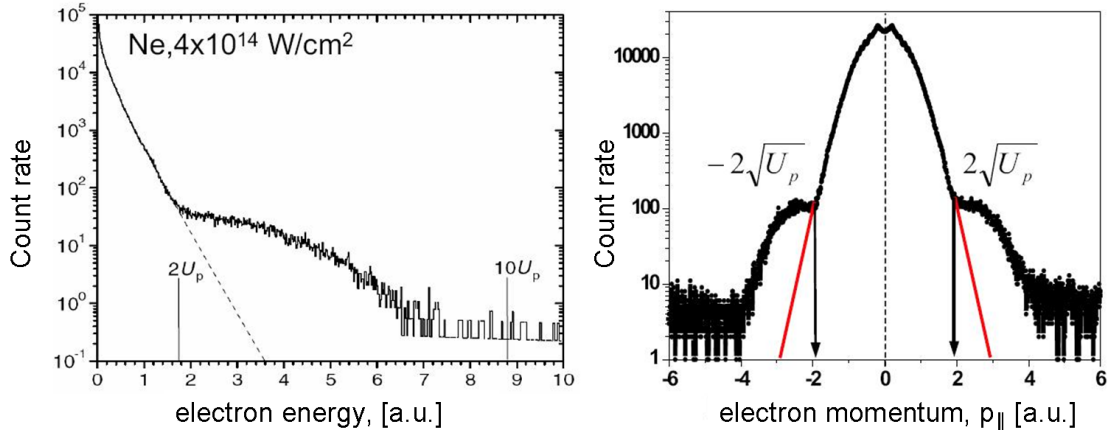
Figure 7.2: Electron kinetic energy spectrum (left) and momentum spectrum (right) along the polarization axis. The wavelength was 800 nm. The characteristic change in the slope at $2\,U_P$ and the plateau up $\approx 10U_P$ are clearly visible. (Picture taken from: [164])

7.1.1.3   Over-the-barrier Ionization

If the intensity is increased further, the region of the over barrier ionization is reached (see 1.1). In this case the maximum of the potential is as high or lower then the binding energy. This means that the electron can reach the continuum more or less unperturbed. In the experiments that are presented in this thesis such intensities were not used. Therefore the reader may refer to [165].

7.1.2   Charged particles in the laser field

In order to focus later on the mechanism of double ionization, first we have to go into the characteristics of charged particles in a laser field. Light can be described as an electromagnetic wave, with perpendicular magnetic and electric fields. An N-times charged particle interacts with this field through the Lorenz force:

$$\vec{F}_L = N \cdot e \left(\vec{E} + \vec{v} \times \vec{B} \right). \tag{7.4}$$

The force exerted by the magnetic field of the light is, as a consequence of the Maxwell equations, by the factor of $\frac{1}{c^2}$ smaller than that of the electric field. At the intensities that were used for the experiments that are described in this thesis, the velocity of the electrons is much smaller than the speed of light c, so the magnetic field can be neglected. We assume that our light is linearly polarized. Then the electric field has the following temporal shape:

$$\vec{E} = \vec{\varepsilon} E_0 \left(t \right) \cos \left(\omega t \right), \tag{7.5}$$

whereas the unit vector $\vec{\varepsilon}$ is in the direction of the polarization, $E_0(t)$ is the envelope of the laser pulse.
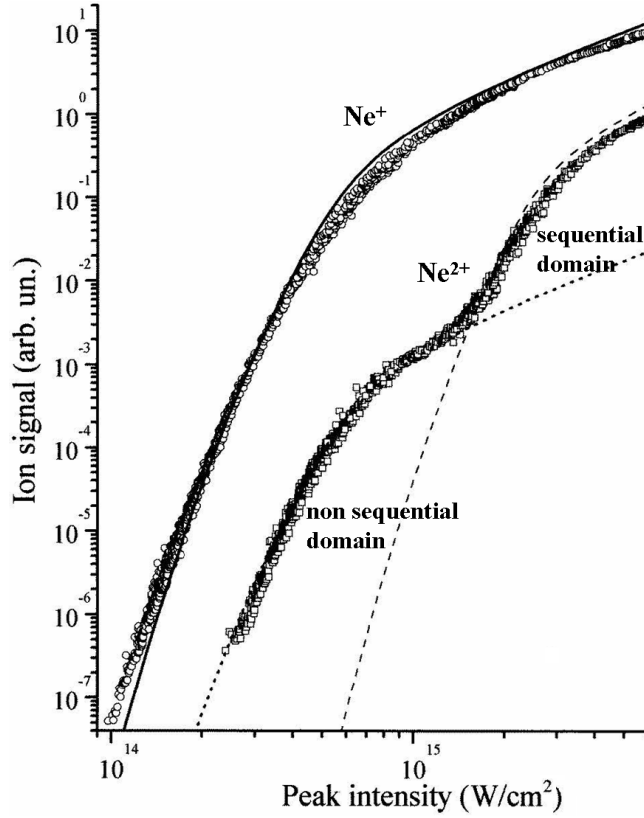
Figure 7.3: Single and double ionization rates of neon. The ADK theory describes the single ionization reasonably well. At low intensities the ion yield for the double ionization is many orders of magnitude larger than predicted by the ADK theory. The origin of the knee structure in the double ionization rates is explained in section 7.1.3. Picture taken from [16].

From this the following equations of motion result:

$$m\dot{v}_z = 0, \quad m\dot{v}_y = 0, \quad m\dot{v}_z = N \cdot eE_0(t)\cos(\omega t), \tag{7.6}$$

where the z axis is in the polarization direction.

7.1.2.1 Trajectories in the oscillating field

We assume that a particle with mass m at the position $z = 0$ at a time t_0 is put into the oscillating field $\vec{E}_0(t)$. Due to reasons that were explained in 7.1.1.2, we assume that this happens near the time of the maximum of the laser pulse's electric field. In an optical cycle of a many-cycle pulse the change in amplitude of the electric field is relatively small and will be neglected. This is crucial for the case in which the particle returns to its origin. By integration of the differential equation 7.6 the velocity and the position of the particle

that, due to the linear polarization, moves along the z axis, can be determined:

$$v_z\left(t\right) = \frac{Ne}{m\omega}E_0\left(t\right)\left(\underbrace{\sin\omega t}_{Oscillation} - \underbrace{\sin\omega t_0}_{Drift}\right) \tag{7.7}$$

$$\Rightarrow p_{Drift} = \frac{Ne}{\omega}E_0\left(t\right)\sin\omega t_0 \underbrace{=}_{\text{for }m=m_e} 2N\sqrt{U_P}\sin\omega t_0, \tag{7.8}$$

$$z\left(t\right) = \frac{Ne}{m\omega^2}E_0\left(t\right)\left(\cos\omega t_0 - \cos\omega t - \omega\left(t - t_0\right)\sin\omega t_0\right). \tag{7.9}$$

Whether the particles return to their origin and which momentum they are carrying depends on the phase of the electric field at the first ionization. We are first considering electrons. Their trajectories are decisive for the mechanism of the electron rescattering. This is the essential process in high harmonic generation (HHG), non-sequential double ionization (NSDI) and the high momentum electron from the single ionization with momenta between 2 and 10 U_P, in above-threshold-ionization (ATI). In figure 7.4 the trajectories $z(t)$ for three different starting conditions of the carrier envelope offset phase ωt_0 are displayed.
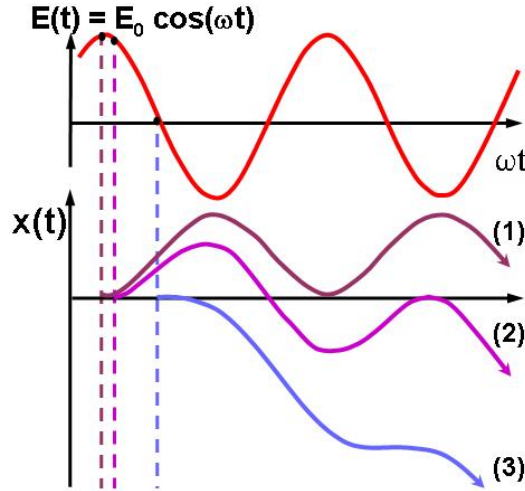

Figure 7.4: Trajectories of electrons in an oscillating electric field. Depending on the time at which the electrons tunnel out of the atom they obtain a different drift momentum. The electrons that reach the continuum at the zero crossing of the electric field, gain the maximum drift momentum of $2\sqrt{U_P}$. The maximum momentum of $3.17\sqrt{U_P}$ at the return to the ion inherit the electrons that are born at a $\omega t_0 = 17°$ into the field.

If the electron tunnels at the maximum of the field (1), it fulfills only an oscillatory motion and does not carry any momentum when it returns to the ion. But if the electron gets at the zero crossing of the electric field into the continuum (3), it gains the maximum drift momentum of $2\sqrt{U_P}$ and it does not return to the ion. In between there are cases where the electron carries a momentum when returning to the parent ion (2). The maximum energy that an electron can carry at such a collision is $3.17\,U_P$.

7.1.3 Double ionization

Multiply charged ions that are generated in the multi-photon ionization were first observed 1979 using the alkaline earth metal barium and strontium, which have two valence electrons in their outer electron shell [166]. Later in 1982 also doubly charged krypton ions were observed, that were ionized with 50 ps long Nd:YAG pulses with an intensity of $10^{13} - 10^{14}$ W/cm^2 [167]. The theoretical methods permitted at this time to calculate the total rates of the multiple ionization in the so called single active electron (SAE) approximation [168–171]. In the approximation the correlation between the electrons in an atom are considered only via an effective potential. This means that the ionization dynamics are determined only by the outermost electron, while the motion of all the other electrons is frozen. In the SAE approximation it is assumed that multiple ionization is a sequential process. Therefore the double ionization can be described in this picture as a two-step process:

$$
\begin{aligned}
A + n_1 \cdot \hbar\omega &\longrightarrow A^+ + e^- \\
A^+ + n_2 \cdot \hbar\omega &\longrightarrow A^{2+} + e^-,
\end{aligned}
\tag{7.10}
$$
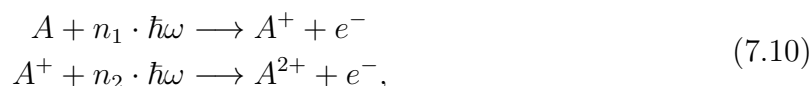
where n_1 and n_2 are the number of absorbed photons. With a new generation of lasers that united high power and stability, ultra short pulses in the order of some fs and high repetition rates were generated. With these it became possible to ionize atoms even higher and to determine the rates of the multiple ionization with a very high accuracy for all rare gases [164].

7.1.3.1 The Non-Sequential Double Ionization

It was observed that SAE based approaches do not describe double and multiple ionization at low and medium intensities. Even though the experimental intensity dependencies of the total rates of single ionization are in good agreement with ADK tunneling theory [163], the results of double ionization show, for certain intensity regions, an ion count rate several orders of magnitude larger than that predicted by theory [171]. A characteristic knee in the distribution of the ion count rate is visible, separating the intensity regions where sequential tunneling predicts the experimental results properly or fails to do so (see figure 7.3). The failure of the SAE approximation to predict the experimental rates indicates that two electrons are removed in a correlated manner out of the neutral atom instead of leaving it independently one after another. In 1983 it was suggested by A. l'Huillier *et al.* that there has to be a non-sequential mechanism to explain the large rates [172]. Only at high intensities, when single ionization is saturated, double ionization becomes sequential and can be described with the tunneling theory. If now the momentum distribution of the doubly charged ions is analyzed, different patterns are visible below and beyond the knee. In the sequential region a distribution is visible that is similar to the tunnel ionization in single ionization (cf. 7.2). In the region of lower intensities the momentum distribution of the double ionized atoms looks totally different. Multiple structures and broadenings are visible, that could not be explained in the beginning. The non-sequential double ionization

(NSDI) was first discovered in xenon [173], then in helium [171, 174, 175], the other rare gases [15, 176, 177] and meanwhile even in some molecules [177–179]. The effect of the NSDI is an evidence for the importance of the electron correlation in the interaction of intense laser pulses and atoms. The process follows the reaction equation:

$$A + n\hbar\omega \longrightarrow A^{2+} + e^- + e^- \tag{7.11}$$
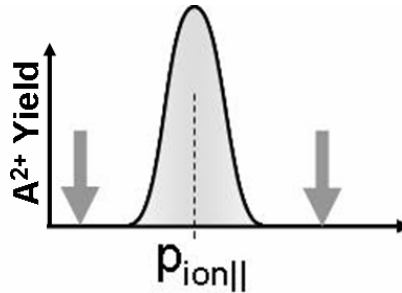

Figure 7.5: The distribution of the ion momenta parallel to the polarization axis shows in the regime of the sequential double ionization a narrow distribution with a maximum at $p_{ion\perp} = 0$. The arrows are positioned at $p_{ion\perp} = 4\sqrt{(U_P)}$.

7.1.3.1.1 Rescattering First indications for the mechanism of the NDSI were delivered by experiments about the dependence of the ionization rate on the polarization of the laser [15, 180]. It was shown, that the NSDI is suppressed if elliptically polarized light is used and the knee structure in the distribution of the ionization rate vanishes totally if circularly polarized light is applied. This effect can be explained very well by the rescattering model but not by other models that were suggested [16]. Additionally also other effects that are related with NSDI could be explained by the rescattering model. These are high harmonic generation (HHG) [14, 181], where the recombination of a returning electron with the parent ion leads to an emission of a high-energy photon with a short wavelength and the existence of the plateaus in the photoelectron spectra for the above-threshold ionization, where an elastic scattering of the returning electron with the parent ion takes place (cf. figure 7.2).

On the first sight the model of rescattering predicts a threshold for NSDI at critical laser intensity. If the energy that the electron gained in the electric field of the laser is not sufficient to ionize the ion another time, the distribution of the ratio between single and double ionization should change abruptly [182]. But this change was measured not as pronounced as expected [174, 183]. Despite numerous studies, a full understanding of the dynamics could not yet be reached.

The validity of the rescattering model for NSDI can not be solved finally by the measurement of the ionization rates. These measurements integrate over all kinetic energies and therefore take only the number of electrons or ions into account. They are not giving any insight into the dynamics of the ionization process and the correlation between
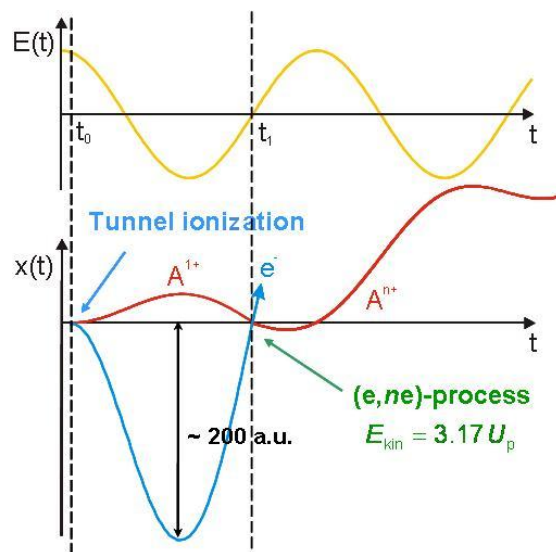
Figure 7.6: Rescattering mechanism: An electron is ionized by tunneling ionization and then accelerated first away from the ion by the electric field and then back. The electron carries an energy of up to 3.17 U_P and if this energy is large enough it can knock one or more electrons in an (e, ne) like process out of the ion.

the photo electrons. To shed more light onto the underlying physics, differential measurements such as photoelectron spectroscopy and measurements of the correlation between the energy and the angular distribution are necessary.

Important progress was achieved when the momenta of individual ions and electrons were measured. With the help of cold target recoil ion momentum spectroscopy (COLTRIMS) the momentum distributions of doubly charged helium and neon were measured [184, 185]. This lead to coincidence measurements, in which the momenta of the ion and all electrons, that are set free during the ionization process, are recorded with all degrees of freedom. On the basis of these measurements and with other high resolution experiments that explored the effects of different wavelengths and intensities [184, 186–188], the mechanisms of the rescattering for NSDI could be elucidated.

7.1.3.1.2 Collision ionization due to rescattering A clear indicator for the validity of the rescattering mechanism is the double hump structure in the ion momentum distribution parallel to the polarization axis, shown in figure 7.7. It is generated by the (e, ne) like scattering of the returning electron with the parent ion. The momentum of the returning electron depends on the time at which it was ionized (see section 7.1.2.1). If the second electron is born near the maximum of the electric field cycle, which is the case for tunneling ionization, the drift momentum of the double ionized atom is negligible. In contrast, the largest momentum $(p_\parallel^{max} = 4\sqrt{U_P})$ can be gained by the ion if the second electron is emitted exactly at the zero crossing of the field, which is close to the time where the most energetic recollision occurs. [184, 185, 189–193]. Therefore, recollision-induced dou-
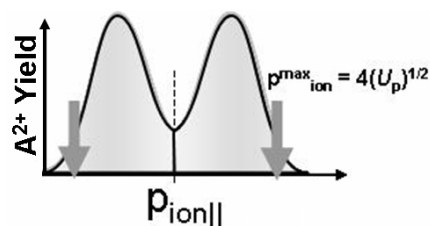
Figure 7.7: Ionization at a distinct time of the oscillating field of the laser pulse leads to a drift momentum. At the ionization time that leads to $p_{drift} = 0$ double ionization can not occur. This causes a double hump structure. Additionally a strong decrease of the double ionization rate at $p_{ion\parallel} = 4\sqrt{U_P}$ can be observed.

ble ionization produces electrons and thus, ions with large longitudinal momenta (since the momentum carried by the photons is negligible, recoil-ion momentum balances the momenta of all electrons) leading to characteristic double-hump structures in the ion momentum distributions. The maximum drift momentum which can be gained by an n-fold charged ion then is $p_{\parallel}^{max} = 2n\sqrt{U_P}$ and, as shown in [193], due to the typical recollision kinematics this value gives an upper classical limit for the most probable ion momenta in the final state.

7.1.3.1.3   Collision excitation due to rescattering   Another effect of the rescattering is a collision excitation by the returning electron followed by a tunneling ionization in the next field maximum. This is called RESI (recollision excitation with subsequent ionization). The mechanism is a three step process that is illustrated schematically in figure 7.8.
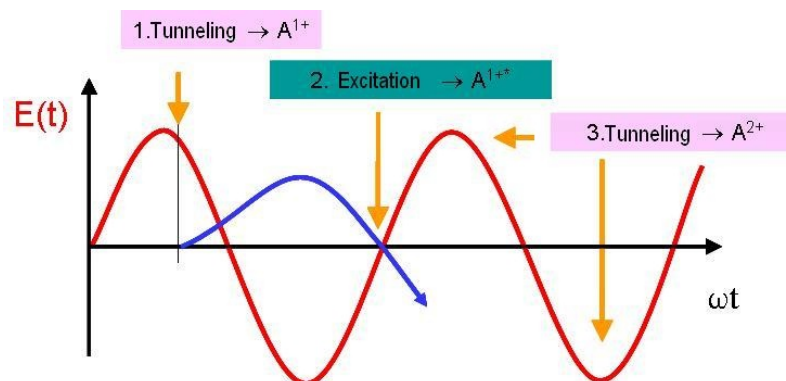

Figure 7.8: Mechanism of RESI (recollision excitation with subsequent ionization): The electron is tunneling into the continuum and is accelerated by the laser field. At the moment of rescattering the ion gets excited into a higher state. The excited ion has now a smaller ionization threshold. Therefore it gets ionized easily in one of the next field maxima via tunneling ionization.

Because the ionization of the second electron is happening via tunneling of the excited state, the momentum distribution in the direction of the polarization axis looks totally different in this type of recollision mechanism. As one can see in figure 7.9 a distribution that is typical for tunneling ionization with a maximum at $p_{ion\|} = 0$ can be observed [190]. On the other side it is considerably broadened in comparison with the momentum distribution of the sequential ionization (cf. figure 7.5). This is owed to the circumstance that electrons from the excited state can tunnel not only at the maximum of the field but also at different times that have lower field strength. Because of this the probability of large drift momenta is higher in the mechanism of RESI as in the sequential tunneling ionization. This leads to a maximum in the distribution (cp. figure 7.5).
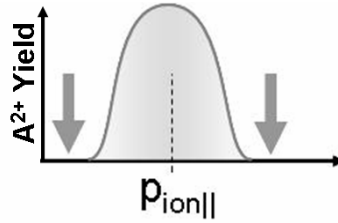

Figure 7.9: Longitudinal momentum distribution of the RESI mechanism according to [190]. The arrows are marking $p_{ion\|} = 2\sqrt{U_P}$. The maximum is at $p_{ion\|} = 0$ which is typical for the tunneling ionization.

However at most experimental conditions RESI and the $(e, 2e)$ like ionization do not appear separated. Therefore, in these cases it comes to a superposition of the momentum distributions of the double ionization. This leads to the fact that a double hump structure that should have an ion yield of zero at $p_{ion\|} = 0$ can not be observed (see figure 7.11). For a quantitative analysis and simulations please refer to [188].

7.1.3.2 Carrier envelope phase dependence of the non-sequential double ionization of rare gas atoms

The electric field of a laser pulse can be described as:

$$\vec{E}(t) = \vec{E}_0(t) \cdot \cos(\omega_L t - \varphi), \tag{7.12}$$

a pulse envelope with a maximum at $t = 0$, $E_0(t)$, the carrier frequency, ω_L, and the CEP (φ) that is freely adjustable and stabilized in modern laser systems. As one can see in figure 7.10 the electric field of an ultra-short laser pulse is changing its characteristic drastically depending on the CEP. For a CEP of $\varphi = 0°$, a so called cosine pulse, there is only one large maximum of the electric field in one direction while the other maxima are significantly smaller. In contrast the pulse at a CEP of $\varphi = \pi/2$, called sine pulse, has two maxima in different directions with the same magnitude and therefore does not induce an asymmetry in processes depending of the pulses electric field as described in section 7.1.2.

The NSDI can occur in two different ways that share the first step. First an electron is released via tunneling ionization. Then the free electron is accelerated away from the
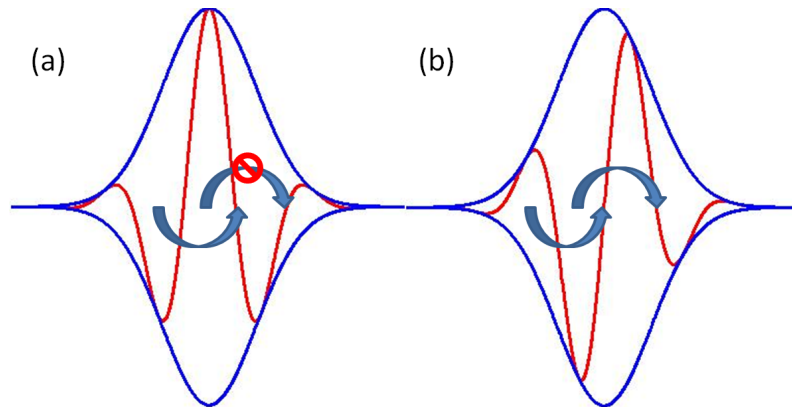
Figure 7.10: Illustration of the electric field for a cosine pulse (a) and a sine pulse (b). In the asymmetric electric field of a cosine pulse, an ionized electron can only rescatter if it is ionized within the first maximum. When it is ionized in the second maximum of the light field, the successive electric field is not strong enough to guide the electron back to the core. For a sine pulse rescattering is possible for two different ionization times.

ion and then back when the direction of the electric field of the laser changes its direction. Depending on the nature of the pulse the electric field is strong enough to guide the electron back to the ion. That is where the CEP dependence is induced. If the electron collides with the parent ion, either an $(e, 2e)$ like collision ionization can take place or a collision excitation can occur. In the case of the excitation, the ion can easily get tunnel ionized a second time in the next maximum of the laser field. This process is called RESI (Recollision Excitation with Subsequent Ionization).

As shown in figure 7.10 in a cosine and a sine pulse, different electron trajectories contribute to the double ionization depending on the nature of the pulse. When the electron returns to the ion and an $(e, 2e)$ scattering occurs, the resulting doubly charged ion gets accelerated. This leads to a characteristic peak in the recoil ion momentum distribution. For a suitable electric field waveform, ionization and recollision with sufficient energy can be restricted to a single double ionization event. This leads to a fading of one of the two humps in the double hump structure which is characteristic for NSDI in few-cycle laser fields. This has been measured before for argon by Liu in 2004 and for neon by Gimpel in 2006 [194, 195] but because of the limited acquisition time with CEP stabilized lasers the statistics were rather poor. With the new approach with single-shot phase tagging it was possible to overcome this restriction.

The momentum distributions of argon and neon are very different (cf. figures 7.15 and 7.19), because the RESI contribution (see section 7.1.3.1.2) is filling the dip between the two humps (cf. figure 7.11). According to Rudenko *et al.* [190], the final ionization step of RESI is a tunneling ionization with its momentum distribution centered at zero. The phase dependence of RESI has not been in the focus until now. The effects observed here are analog to the phase dependence of the single ionization of the rare gas atoms as described by Chelkowski *et al.* [196]. This means the obvious phase dependence in the
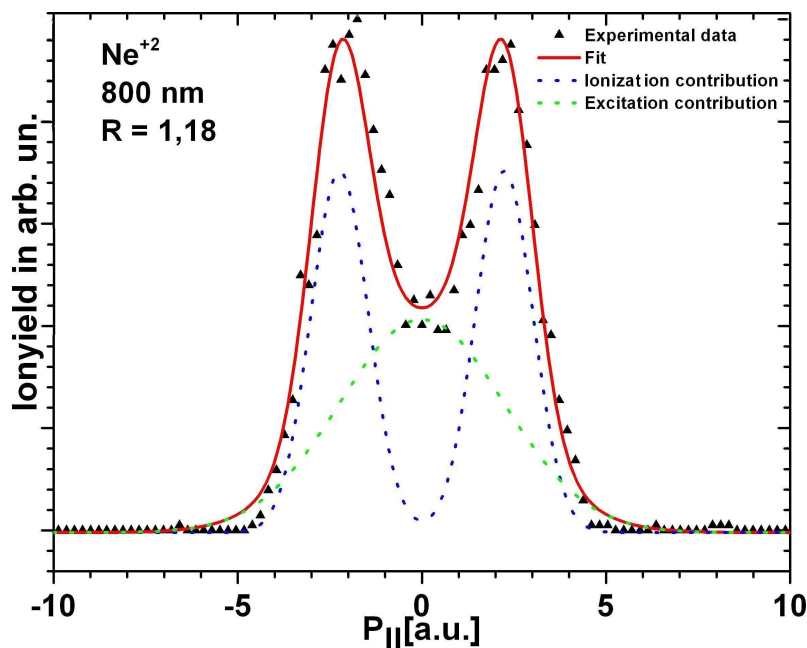
Figure 7.11: Fit of the double hump structure of neon. The ionization and excitation contribution of the recollision are illustrated. The $(e, 2e)$ like ionization has a more obvious phase dependence than the RESI part. In argon the excitation part is much larger. This leads to a filling of the minimum. (Further information in and picture from [188])

measurement of the double ionization is mostly on the $(e, 2e)$ process and will be visible in an asymmetric depletion of the double hump structure at large momenta. For the phase dependence of the RESI process one has to look more carefully and further measurements were also the electrons from the NSDI were measured in coincidence may shed more light into this.

By adopting the new technique of single-shot phase tagging (cf. 7.2.2) to an IR laser system with sub 4 fs pulses, it was possible to measure a continuous picture of the CEP dependence of the longitudinal recoil ion momentum distribution instead of measuring at specific CEPs. Also longer acquisition times were possible, because the laser system had not to be phase stabilized, and a correlation between the CEP and the peak intensity could be excluded. This enabled us to measure the phase dependence of NSDI of neon and argon with an unmatched phase resolution.

7.2 The IR laser setup

7.2.1 The femtosecond laser system

For the IR experiments described in this thesis a Chirped Pulse Amplification (CPA) system from the company *Femtolasers* was used. The oscillator is a Ti:Sa (titanium

doped sapphire) solid state laser that is pumped by a CW frequency doubled Nd:YAG laser with a wavelength of 532 nm. The oscillator produces a seed pulse for the amplifier that first has to be stretched from a pulse length of seven fs to a length of seven to eight ps. This is done by a set of chirped mirrors and bulk glass. If this was not the case, the laser pulse would gain an intensity during the amplification that exceeds the damage threshold of the amplification Ti:Sa crystal. Due to stretching, a long pulse with a strong temporal chirp is given, leading to a lower peak intensity which does not harm the crystal. Now the pulse is sent four times through the Ti:Sa amplification crystal that is pumped by a pulsed, frequency doubled Nd:YAG laser, and is amplified by a factor of several thousand. If from this point all of the seed pulses would be amplified, the thermal load would be too high. Therefore, a Pockels-cell is used to reduce the repetition rate from 80 MHz to 3 kHz [197]. Now there are fewer pulses, which extract energy from the pump crystal and less pump energy is needed for a certain gain. These selected pulses pass the crystal for another five times and gain in total more than a factor of 500,000 in energy. After amplification the pulse is compressed by a prism compressor and a chirped pulse compressor to a pulse length of 20 fs. Due to gain narrowing during the amplification the short pulse length provided by the oscillator cannot be reached after the amplification [198].

To achieve short pulse duration, the beam is focused into a neon filled hollow core fiber. In this fiber self focusing and wave guiding effects take place, so that the intensity is high for a long distance [199]. This results in self-steepening and self-phase-modulation which lead to spectral broadening. In our case, the spectrum reaches from the blue (450 nm) down to the mid infrared (1100 nm). This broadened pulse becomes recolliminated after the fiber and again compressed by a chirped mirror compressor. At the beamline that was used here sub 3 fs pulses can be reached [200].

7.2.2 The stereo ATI

For this thesis also IR experiments have been performed at the MPQ in Garching. These experiments involved measurements of phase effects of molecules and atoms. A novel technique for phase measurements was utilized, namely the single shot stereo ATI technique, described here.

Presently, the CEP effects for a given process are typically measured by locking and scanning the CEP while acquiring data. This can take more than 24 hours for full differential measurements including a delay scan. The phase locking technique is complex and is typically achieved via feedback loops, which themselves are only stable for several minutes in the worst case, and several hours in the ideal case. Thus, stabilization of the laser operating parameters, e.g. temperature and power [201, 202], is required if phase lock over a period of hours has to be achieved. Therefore, for many applications, it may be simpler and more effective to renounce the CEP locking mechanisms if a precise measurement of the CEP can be made for every single laser pulse. Ideally, one would like to have a robust way to measure the absolute CEP of each pulse with a high precision and accuracy in real time while using minimal laser power. This way the information can be used as an additional data column for every recorded laser shot of a single shot

measurement. Additionally, in situations when CEP locking is desired or required, such a technique could serve as a powerful diagnostic tool or an alternative method of feedback [194]. Although multiple techniques have been developed which are capable of retrieving the CEP [203–207], determining the CEP of each and every laser shot individually and continuously in real time for a kHz laser system was only recently achieved [208].
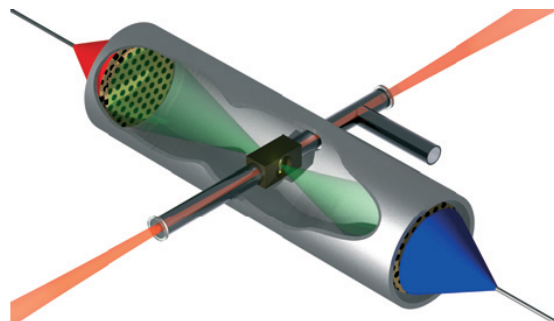

Figure 7.12: The single-shot stereo-ATI phase meter. Two opposing TOF spectrometers are mounted in a compact high-vacuum apparatus, carefully shielded (symbolized by the μ-metal-shielding tubes) from electrical and magnetic fields. Xenon atoms at a pressure in the order of 10^{-2} mbar fills the inner part of a differential pumping stage. The xenon atoms are ionized near the focus of the laser beam and enter the ultrahigh-vacuum drift tubes through the vertical slits. The electrons are then detected with a pair of MCP detectors. Drawing taken from [208].

7.2.2.1 Mapping the CEP with rescattered ATI electrons

The approach used here for the phase measurement relies on ATI (Above Threshold Ionization see section 7.1.1.1) in an isotropic medium (gaseous xenon) by a linearly polarized few-cycle pulse (for the configuration see fig. 7.12). The asymmetric field of the laser pulse results in an asymmetric photoelectron emission in opposite directions parallel to the laser polarization. There are two different mechanisms leading to typical ATI photoelectron spectra. Most photoelectrons leave the atoms directly with low energy ($< 2\,U_P$). A tiny fraction ($< 1\,\%$) are accelerated back to the parent ion and rescatter at a time t_1 approximately three quarters of an optical cycle after the initial ionization at time t_0. Rescattered ATI electrons can acquire substantial kinetic energy (up to $10\,U_P$) and form a characteristic plateau [209] at the high energy side of the photoelectron spectra. This phase measurement relies exclusively on the investigation of these plateau electrons as they show a stronger phase dependence than direct photoelectrons [196, 210]. For low-energy (direct) electrons, asymmetric ionization yields at instant t_0 are largely wiped out by the deflection of the photoelectrons in the laser field [211]. High-energy (rescattered) electrons re-collide with the ion core as already noted. After backscattering at time t_1, they can be accelerated to high energy only if the field strength of the laser pulse is large enough during the optical cycle following the scattering event. In addition, the field strength should also

be high at the instant t_0 of initial ionization to provide high ionization probability. As t_0 and t_1 differ by approximately three quarters of an optical cycle, both conditions are hard to meet for a few-cycle pulse. This, together with some other boundary conditions in the kinematics of re-colliding electrons, gives rise to the strong CEP dependence of the plateau part of the photoelectron spectra.
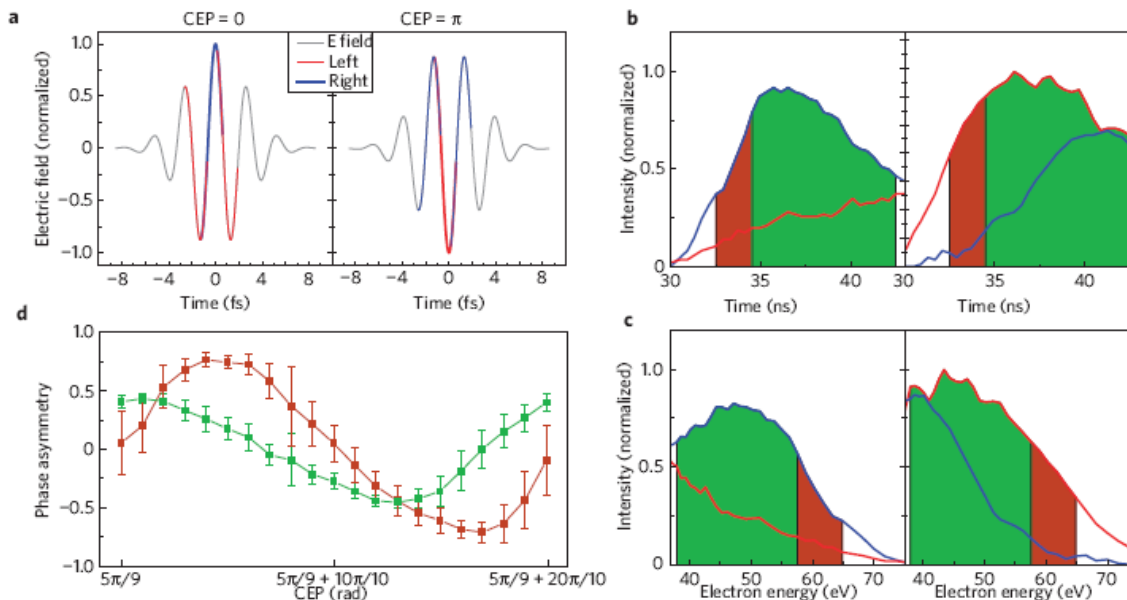

Figure 7.13: ATI with few-cycle pulses. **a**, Travel times of re-scattered electrons (red and blue lines) in the ATI process in the electric field of a cosine and anti-cosine pulse. Red and blue indicates whether the electron, re-scattered after its trip, is detected by the left or right detector. **b**, **c**, Single-shot left and right TOF spectra **b** and converted energy spectra **c** recorded experimentally. The green and red areas indicate the spectral ranges used to extract the phase asymmetry parameters x and y (definition see text). **d**, Dependence of the phase asymmetry parameters x and y on the CEP. Depending on the selection of the spectral ranges from which the parameters are derived the sinusoidal curves are shifted, in this case by 60°. (Picture taken from [208])

The travel times of a few re-scattered electrons in the laser field are shown in fig. 7.13a for cosine and sine pulses. Red and blue lines indicate electrons propagating to the left and right detectors, respectively. The asymmetry of the photoelectron spectra (fig. 7.13b,c) is quantified by the normalized phase asymmetry parameter: $(P_L - P_R) / (P_L + P_R)$, where P_L and P_R are the numbers of electrons integrated over a certain energy interval emitted in the left and right directions. It has been demonstrated experimentally and numerically [196, 211, 212] that the phase asymmetry parameter is depending on the CEP in a nearly sine-like way if P_L and P_R are determined from the complete high-energy spectra. The differential asymmetry, that is the asymmetry calculated for a given range of electron energies, changes in a nearly sine-like way with a shift of the CEP. However there is a gradual phase shift in this dependence with increasing electron energy. A novel method

for measuring and retrieving the CEP was applied, which exploits this observed shift (see fig. 7.13d) is the single-shot Stereo-ATI technique. Two CEP asymmetry parameters were defined. These ranges are indicated by the green and brown areas on the time-of-flight and energy spectra for the cosine and sine waveforms of the laser pulse in fig. 7.13b and c. The time-of-flight spectra for CEP retrieval were used because those are the raw unprocessed signals from the measurement apparatus. Parameter x was calculated as $(P_L - P_R)/(P_L + P_R)$, where P_L and P_R are the integrated signals. y was calculated analog. The two Parameter CEP asymmetry curves obtained in this way are shifted against each other by approximately 60°.
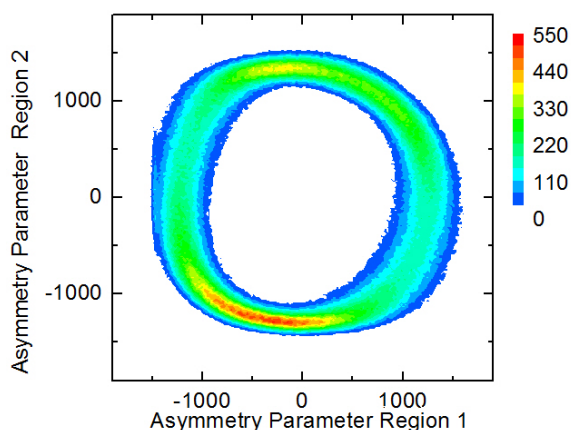
Figure 7.14: Mapping the CEP of non-phase-stabilized consecutive laser pulses. Consecutive single laser shots from a non-phase-stabilized laser at 3 kHz repetition rate represented on a parametric plot in which the axes x and y are the phase asymmetry parameters derived for two TOF ranges in the ATI spectra.

Instead of the conventional linear representation (phase asymmetry versus phase), new insight can be gained by plotting these sine-like phase asymmetries on a Lissajous like parametric plot with each axis corresponding to one of the two CEP asymmetries. In fig. 7.14, laser shots with a random CEP are shown in that representation. With the two phase asymmetry parameters, the CEP of each shot (in the entire 2π range) is mapped to one point on the ellipse-like curve, which implies that there is no phase uncertainty. The reason for a slightly deformed ellipse is due to the fact that the phase asymmetry curves are not perfectly sine shaped and that the responses are not exactly identical if the two electron detector are not identical, what they never are.

7.3 Experimental results and discussion

7.3.1 Neon

Neon is a perfect model to study the phase dependence of the $(e, 2e)$ like process in the NSDI, because it is the dominating process. The double hump structure, typical for the

$(e, 2e)$ process can be clearly seen in neon and RESI plays a much less important role (cf. [188]). As mentioned above in neon mostly the $(e, 2e)$ process is contributing to the NSDI. Therefore we can concentrate on its phase dependence.
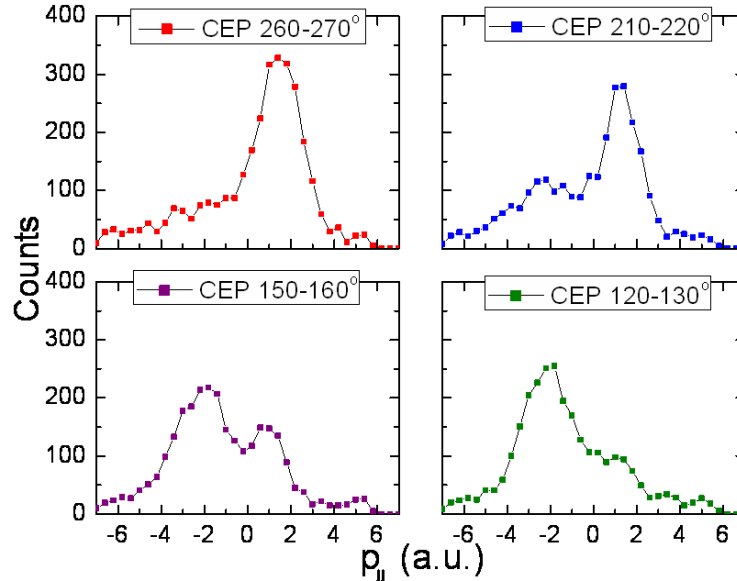

Figure 7.15: Longitudinal momentum distribution of neon at four different CEPs. The shift in the momentum distribution in dependence of the CEP is very pronounced. This data was measured with sub 4 fs pulses and a peak intensity of approximately $5 \cdot 10^{14}$ W/cm^2.

The neon data presented here was measured with a pulse length of approximately 4 fs, at a center wavelength of 750 nm and a peak intensity of approximately $5.2 \pm 1.3 \cdot 10^{14}$ W/cm^2. This intensity was extracted from the position of the maxima in the double hump structure that are located at $\pm 2\ U_P$. Unfortunately the intensity estimation with this position has a large uncertainty.

In figure 7.15 the CEP-dependent change of the double hump structure of the dication recoil momentum is very pronounced for NSDI of neon. The individual panels are integrated over a segment of the CEP circle. A very large asymmetry with the right hump dominating the spectrum between $260°$ and $270°$ can be seen, this changes into a rise of the left hump between $210°$ and $220°$. The emphasis shifts further on to the left in the next plotted segment between $150°$ and $160°$ and at a phase between $120°$ and $130°$ the right hump is mostly suppressed, while the left one is very strong. The most striking feature in this measurement is the almost completely transfer of events from one side of the distribution to the other.

If now the momentum is plotted against the phase (see figure 7.16) one can see a continuously change of the signal from one direction to the other and then back again. The phase effect is extremely pronounced.

The asymmetry parameter is a measure of the asymmetry of the momentum distribution
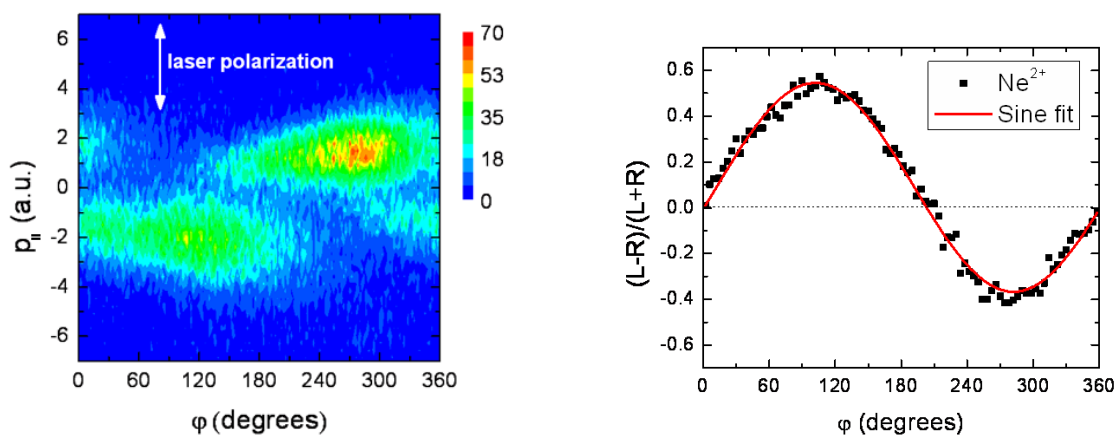
Figure 7.16: Left: Plot of the ion momentum distribution in polarization direction vs. the phase. The depletion of one of the two maxima near ± 2 a.u. at a phases of $100°$ and $280°$ is nicely pronounced. Right: Asymmetry parameter vs. phase. The asymmetry follows a almost perfect sine function.

in polarization direction [2]. It compares the number of counts in the left channel and the right channel with each other while a maximum asymmetry has the absolute value of 1. As one can see in the right picture of figure 7.16 the asymmetry is nicely pronounced and follows a sine function in a nearly perfect way. This measurement was the high signal-to-noise measurement of the CEP-dependent asymmetry in neon, which became only feasible with the implementation of the phase-tagging concept described in 7.2.2. It was possible to achieve much higher statistics as in previous measurements and additionally we were able to measure all phases at once and did not have the risk that a shift in the laser parameters falsifies our results.

If the double ionization events are integrated over all momenta, the dependence of the double ionization yield on the CE-phase can be explored. Naively one would expect that the double ionization yield depends on the maximum electric field in the laser pulse. If this shape is now compared to the measured doubly charges ion yield in figure 7.17 it can be seen that this expectation is only applicable in a limited way. The minima can be found at the integer multiple of π while the maxima are shifted in respect to the minima by $\pi/2$.

7.3.2 Argon

In the double ionization of argon, which was also measured with sub 4 fs pulses at a peak intensity of approximately $1.6 \pm 0.4 \cdot 10^{14}$ W/cm^2, the double hump structure is not visible. It is known [164], that in argon RESI is a much more important process at low intensities than $(e, 2e)$ Therefore in argon a different CEP dependence might be expected than in neon. The intensity is again estimated from the $2\,U_p$ cutoff in the longitudinal momentum.

---

[2] $\frac{L-R}{L+R}$, where L is the integral over the events with a negative momentum and R is the ion yield with a positive momentum.
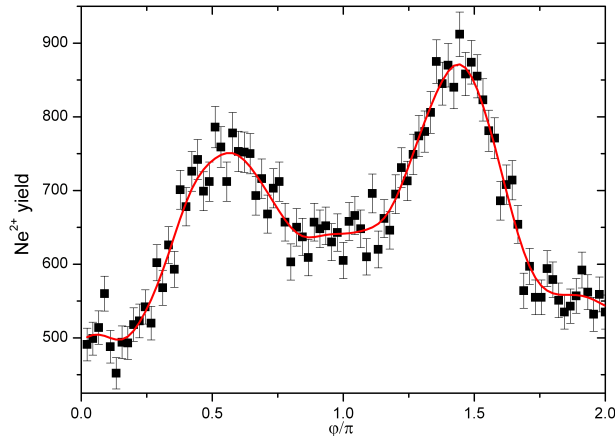
Figure 7.17: Integrated ion yield of the double ionization of neon in dependence of the phase.

The phase effects of the RESI contribution have not been investigated before and until now there are also no theoretical predictions. Triggered by our results calculations are in progress.
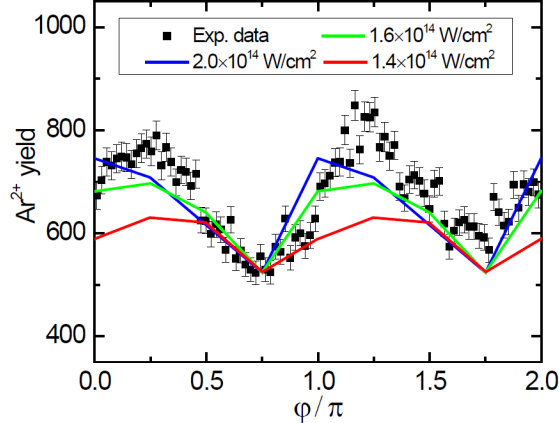
Figure 7.18: Comparison of the experimental CEP-dependent Ar^{2+} yield (black squares) with theoretical predictions (colored lines) for three different intensities from Micheau *et al.* [213]. The error bars indicate the statistical error of the experimental data.

Employing the phase-tagging approach, for the first time the CEP dependence of the Ar^{2+} ion yield for constant pulse duration and intensity has been measured (see figure 7.18). The intensity in our measurement $1.6(\pm 0.1) \times 10^{14}$ W/cm^2 is determined from the $2U_p$ cutoff in the longitudinal momentum (along the laser polarization axis) of H_2O^+, which was present as background in the jet in our experiments on argon. The experimental Ar^{2+} ion yield data in figure 7.18 is compared to recently published theoretical results by Micheau *et al.* [213]. They calculated the Ar^{2+} yield for a 5-cycle pulse centered at 800 nm at three intensities of $(1.4, 1.6, 2.0) \times 10^{14}$ W/cm^2. The theoretical curve for 1.6×10^{14} W/cm^2

agrees best with the data presented here, consistent with the experimentally determined intensity. The calculations predict minima in the Ar^{2+} yield at approximately $3/4\pi$ and $7/4\pi$, which are independent of intensity in this range [213]. In figure 7.18, we choose φ_0 in the experimental data such that the dip in the total Ar^{2+} yield occurs at the same phase as in the theoretical curves. Although the yield is clearly CEP dependent, it has a $\pm\pi$ inversion symmetry. However, this ambiguity can be eliminated with the phase-dependent Ar^{2+} momentum spectra.

As can be seen in figure 7.19, for argon the momentum distribution is shifting from the left to the right as a function of the CEP, but the shift is not as pronounced as for neon (cf. 7.15). In figure 7.19 the red curve is integrated over a phase between 113° and 117° and the blue one, with a phase between 299° and 303°, show a very nice asymmetry and differ significantly from the distribution with an integrated phase plotted in black.
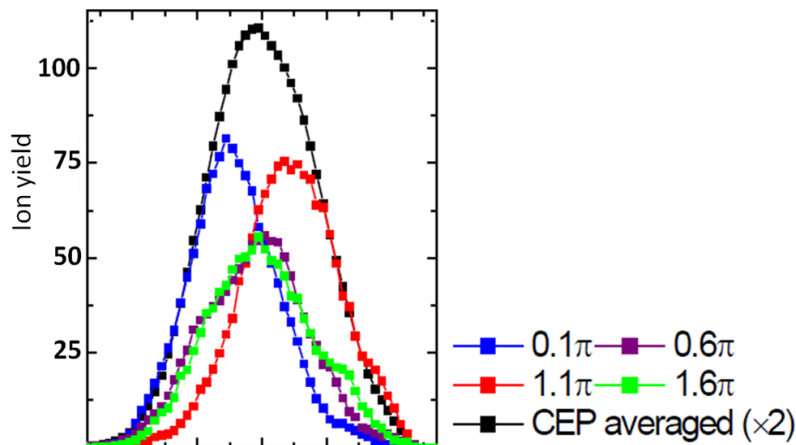
Figure 7.19: Longitudinal ion momentum distribution of the double ionization of argon measured with sub 4 fs pulses at a peak intensity of $1.6 \cdot 10^{14}$ W/cm^2. The integral over all phases is plotted in black. One can see that the dip between the two humps is filled up. In red is the momentum distribution at a phase between 113° and 117° and in blue at a phase between 299° and 303°.

If we draw our attention to figure 7.20, on the right the longitudinal momentum is plotted versus the phase. In contrast to the neon measurement we do not see islands of high count rate instead we can see a band that shifts up and down. This may be understood if the large contribution of the RESI process is taken into account, which should have a phase dependence that is similar to the single ionization via tunneling [211]. There the main part of the phase dependence is a shift in the high momentum part similar to what can be observed here.

On the right side of figure 7.20 the asymmetry parameter is plotted against the phase and it follows a sine curve just as with the $(e, 2e)$ process in neon. If only the large momenta are taken into account for the asymmetry parameter, the behavior of the asymmetry is about the same as in neon.
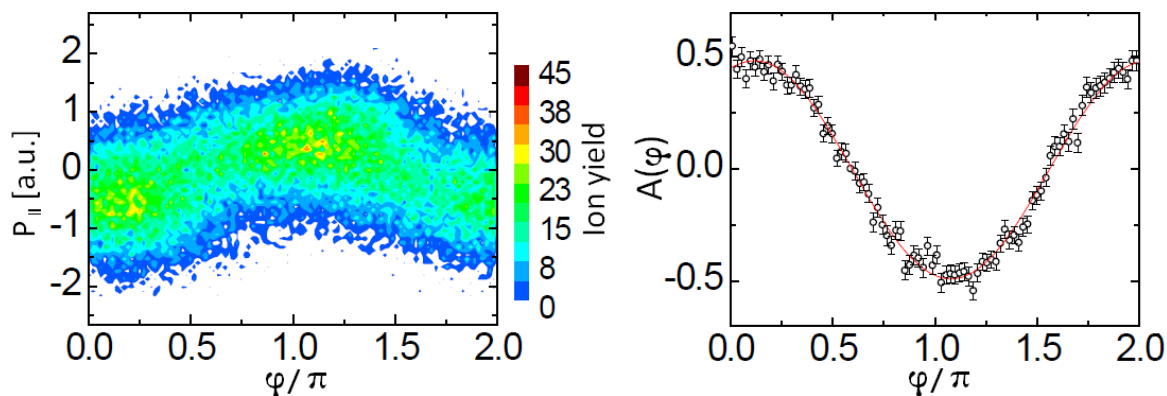
Figure 7.20: Left: Longitudinal ion momenta vs. the phase for argon. Right: Asymmetry parameter versus the phase. The momenta chosen for the evaluation of the asymmetry parameter are between ± 1 a.u. and ± 2 a.u..

7.4 Conclusion

As shown in this chapter, we were the first to combine single-shot phase tagging and the reaction microscope technique allowing to record the full reaction dynamics. This enabled us to measure the phase dependence of NSDI with a sharpness of detail that has not been achieved before. These measurements showed that the phase dependence of the $(e, 2e)$ like double ionization process manifests itself in a very pronounced depletion of one or the other of the two maxima in the characteristic double hump structure of the longitudinal momentum distribution. The even more startling finding is the phase dependence in a regime of the up to this point mostly disregarded RESI mechanism. With ongoing theoretical studies and recent measurements that include also the two emitted electrons we hope to shed light into this issue.

Chapter 8

Conclusion

In this thesis, XUV pump-probe experiments using femtosecond XUV pulses from free electron lasers have been performed for the first time to time-resolve ultrafast electronic and nuclear dynamics in atoms and molecules. This is done to reveal the dynamics of nonlinear effects in the multiphoton ionization, since even the two photon single ionization is not jet understood [146].

To perform the XUV-pump XUV-probe experiments, it was necessary to design a split mirror assembly (see 2.3) to delay a fraction, usually one half, of the pulse. This device was combined with a reaction-microscope that allowed the recording of the full 3D momentum information of all fragments (ions as well as electrons) from the interaction of the laser with an atom or molecule.

Since unseeded FELs do not have a shot-to-shot reproducible temporal structure, it was necessary to characterize the pulses, as described in chapter 3. Utilizing the split-mirror setup, non-linear autocorrelation measurements were performed. We were the first to characterize the pulses of SCSS (Spring8 Compact SASE Source) in Harima(Japan) and also implemented such measurements at FLASH (Free Electron Laser Hamburg). In cooperation with T. Pfeifer it was possible to simulate the multipeak structure from FEL pulses out of the autocorrelation trace. Pulses with an overall temporal width of down to 30 fs and spikes with a width of below 10 fs were characterized. The knowledge on the pulse characteristics enabled us to perform calculations for more complex experiments where the pulse structure plays a role and where the partly coherent pulses were essential in achieving a time-resolution surpassing the XUV pulse duration.

The first XUV-pump XUV-probe experiments on molecules were performed at FLASH with oxygen and nitrogen as targets. The fragments from the doubly, triply and fourfold ionized oxygen and nitrogen molecules were analyzed. Except for the fragments from O_2^{2+} very pronounced dissociative features in the ion kinetic energy release (KER) spectra could be observed. In addition, broad features in the KER spectra of ionic fragments independent of the pump-probe time delay were observed, which are ascribed to the population of bound states by the pump pulse. The nuclear wavepacket motion in such states would cause an oscillatory behavior, which, however, was not observed in these first experiments due to a so far limited time-resolution using the FLASH pulses and a limited signal-to-noise ratio.

All the dissociative features in the spectra of kinetic energy release (KER) vs. delay spectra could be reproduced. The data show that such measurements can help to track molecular dynamics in real-time and ultimately image the potential energy surfaces that are responsible for the unfolding dynamics.

As part of our pump-probe experiments on oxygen, the transient XUV depletion dynamics of highly excited O_2^+ following XUV photoionization was studied. The analysis of the experimental results indicates that the autoionization dynamics of a super-excited molecular ion has been measured. Further theoretical analysis is needed to understand the data in more detail and attempt a simulation of the experimental traces recorded for photon energies of 38 eV and 46 eV. This autoionization process of oxygen is interesting for the understanding of such processes in the ionosphere of the earth where high energetic photons are absorbed by oxygen and nitrogen molecules. To understand and model such processes, these first measurements may serve as a reference to test theoretical predictions of the inner valence ionization of oxygen molecules and successive autoionization processes.

The two photon double ionization (TPDI) of deuterium was studied by time dependent XUV pump XUV probe as well as single pulse XUV experiments. In the single pulse experiments the KER distribution of the non-coincident deuterium ions could be reproduced theoretically within the Born-Oppenheimer-approximation. The non-sequential TPDI, where two photons are absorbed simultaneously, and the sequential TPDI, where one photon is absorbed and after some evolution, the final ionization step takes place with another photon, could be distinguished. These results are a significant step forward in the understanding of TPDI. The time dependence of the TPDI of deuterium was then examined by following the $1s\sigma_g$ D_2^+ bound-state vibrational wave-packet. Its motion was detected with a time resolution better than 10 fs. The comparison to model calculations showed a good agreement with respect to the experimentally observed vibrational period of the state of 22 ±4 fs.

Our XUV pump-probe scheme combined with many-particle imaging methods opens a variety of future possibilities. (i) Highly excited states, such as metastable twofold ionized states in N_2^{2+} or doubly excited D_2^{**}, can easily be reached within just one frequency-controlled XUV pump step. Moreover, light-induced conformational changes in molecules (isomerization) or investigations of the dynamics at conical intersections will become accessible. (ii) At sufficient photon energies the nuclear wavepacket as a whole is projected from position (R) to momentum space allowing for its complete imaging. This is different from previous measurements with IR lasers where the wave-packet could not be traced at small R. (iii) Pump and probe steps are free from aberrations in the sense that they ideally involve one-photon absorption processes. (iv) Measuring the emitted electron by coincidence will allow time-dependent "imaging of molecules from within". This will lead to a deeper understanding of matter-light interaction and nonlinear multiphoton ionization effects.

Independent from this, in chapter 7 the carrier envelope phase (CEP) dependence of the non-sequential double ionization (NSDI) of the rare gas atoms of argon and neon was investigated using near-infrared radiation. Strong field ionization is examined with most different Keldysh parameter, compared to the XUV-experiments even though the fields do

have the same strength. These measurements showed that the phase dependence manifests itself in a very pronounced depletion of one of the two maxima in the characteristic double hump structure of the longitudinal Ar^{2+} recoil momentum distribution. Most interesting, is the phase dependence of the up to this point mostly disregarded RESI (rescattering with subsequent ionization) mechanism. A very pronounced sine like variation of the asymmetry in the longitudinal Ar^{2+} recoil momentum with a period of 2π could be observed for both NSDI processes.

Acknowledgment

First of all I would like to thank my wife Andrea for her fondly support and the understanding for my vast times of absence and negligence. Then my recognition goes to my advisor Matthias Kling. I would like to thank him for the supervision and for an open ear whenever it was needed. Also without the excellent work when it comes to the arrangement of new cooperations or to seize grants to ensure the funding for our very expensive worldwide projects. Also very special thanks to Ferenz Krausz for giving me the opportunity to work in his group with all the benefits that are special to his group and his cluster of excellence, MAP. Also I would like to show my gratitude to Matthias Lezius from which I learned a lot about experimental techniques and had uncounted fruitful discussions with. Next my thanks are with my collaborators from the Max Planck Institute for Nuclear Physics in Heidelberg, especially Robert Moshammer who was an excellent teacher in the field of atom- and molecular physics, Claus-Dieter Schröter, Kai-Uwe Kühnel from whom I learned really a lot about UHV and experiment design, Moritz Kurka and Yuhai Jiang that showed me how to use the analysis and the rest of the group of Joachim Ullrich. Also special thanks to Artem Rudenko from the Max Planck Advanced Studies Group at CFEL in Hamburg. He was most of the time the major brain behind all our experiments and was always there when we were measuring, shared his vast knowledge with me and was always there when I needed him. Without those people my work would not have been possible and I would like to say thank you for several months of shared beam-time. I am grateful to Kiyoshi Ueda's group from Tohoku University, Sendai, for the possibility to work in his fascinating country and Hironobu Fukuzawa and his team for the warm accommodation at our beam-times and in Sendai. Also I would like to thank my coworkers in Garching with whom I build up the reaction-microscope and performed measurements at AS1: Nora Jonson and Boris Bergues. It was a pleasure to work together with them. Also my gratitude is with Hartmut Schröder for all the fruitful discussions and all the ideas and with Sergey Zherebtsov who took over several night shifts during beam times at AS1 so I could get some hours of sleep. My special thanks are with Adrian Wirth. We started on the same day and shared a lot during those years and whenever we had the chance to work together we had a nice time. Also my thanks are with the technicians I worked with, especially Walter Ritt from the MPQ and Bernd Knape and Christan Kaiser from the MPI in Heidelberg. Special thanks also to my successor Matthias Kübel with whom I had some really nice beam-times and it was very nice working with him. Furthermore I would like to express my gratitude to my fellow companions in misfortune Frederik Süßmann, Yingying Yang, Irina Znakovskaya, Vladislav Yakovlev, Elisabeth Magerl, Justin Gagnon and Michael Hofstetter and all the other people from the Krausz Group. Last but not least many thanks to my parents that supported me on my whole path in every thinkable way.

Appendix

Atomic Units

In atomic and molecular physics often *atomic units* are used. The basic units for length, mass, charge and velocity depend on the corresponding values for an electron in the ground state of the hydrogen atom. This results in the following base quantities and constants:

Base units and natural constants

$r_e = 1\,au = 5,2918 \cdot 10^{-11}m$	Bohr radius of the hydrogen K-shell
$v_e = 1\,au = 2,1877 \cdot 10^{6}m/s$	velocity on the Bohr orbit
$m_e = 1\,au = 9,1095 \cdot 10^{-31}kg$	rest mass of the electron
$q_e = e = 1\,au = 1,6022 \cdot 10^{-19}As$	charge of the electron
$\hbar = m_e v_e r_e = 1\,au$	Angular momentum quantum
$c = e^2/(\hbar\alpha) = 137\,au$	speed of light

Often helpful to know are the conversion factors between atomic units and other major units:

Scaling factors

Energy	$E\,[eV] = 27,2 \cdot E\,[au]$
Momentum	$p\,[kg\,m/s] = 1,995 \cdot 10^{-24} \cdot p\,[au]$

Bibliography

[1] M. Göppert-Mayer. über elementarakte mit zwei quantensprüngen. *Annalen der Physik*, 9:273, 1931.

[2] V. Hughes and L. Grabner. The radiofrequency spectrum of rb^{85}f and rb^{87}f by the electric resonance method. *Phys. Rev.*, 79(2):314–322, 1950.

[3] G. s. Voronov and N.B. Delone. *JETP Letters*, 1:66, 1965.

[4] L.V. Keldysh. Ionization in the field of a strong electromagnetic wave. *Sov. Phys. JETP*, 20:1307, 1965.

[5] A.M. Perelomov, V.S. Popov, and M.V. Terentev. *Sov. Phys.JETP*, 23:924, 1966.

[6] Perelomov A.M., V.S. Popov, and M.V. Terentev. *Sov. Phys.JETP*, 24:207, 1966.

[7] A.I. Nikishov and V.I. Ritus. *Sov. Phys.JETP*, 23:162, 1966.

[8] V.V. Suran and I.P. Zapesochny. *Sov. Phys.- Techn. Phys. Lett.*, 1:420, 1975.

[9] R. Dörner, Th. Weber, M. Weckenbrock, A. Staudte, M. Hattass, H. Schmidt-Böcking, R. Moshammer, and J. Ullrich. Multiple ionization in strong laser fields. In B. Bederson and H. Walther, editors, *Advances In Atomic, Molecular, and Optical Physics*, volume 48, pages 1 – 34. Academic Press, 2002.

[10] A. Becker, R. Dörner, and R. Moshammer. Multiple fragmentation of atoms in femtosecond laser pulses. *J. Phys. B*, 38(9):S753, 2005.

[11] J. S. Briggs and V. Schmidt. Differential cross sections for photo-double-ionization of the helium atom. *J. Phys. B*, 33(1):R1, 2000.

[12] L. Avaldi and A. Huetz. Photodouble ionization and the dynamics of electron pairs in the continuum. *J. Phys. B*, 38(9):S861, 2005.

[13] M.Yu. Kuchiev. Atomic antenna. *Sov.Phys.- JETP Lett.*, 45(7):404, 1987.

[14] P. B. Corkum. Plasma perspective on strong field multiphoton ionization. *Phys. Rev. Lett.*, 71(13):1994, 1993.

[15] D. N. Fittinghoff, P. R. Bolton, B. Chang, and K. C. Kulander. Polarization dependence of tunneling ionization of helium and neon by 120-fs pulses at 614 nm. *Phys. Rev. A*, 49(3):2174, 1994.

[16] S. Larochelle, A. Talebpour, and S.L. Chin. Non-sequential multiple ionization of rare gas atoms in a ti:sapphire laser field. *J. Phys. B*, 31(6):1201–1214, 1998.

[17] Y. Liu, S. Tschuch, A. Rudenko, M. Dürr, M. Siegel, U. Morgner, R. Moshammer, and J. Ullrich. Strong-field double ionization of ar below the recollision threshold. *Phys. Rev. Lett.*, 101(5):053001, 2008.

[18] A. Emmanouilidou and A. Staudte. Intensity dependence of strong-field double-ionization mechanisms: From field-assisted recollision ionization to recollision-assisted field ionization. *Phys. Rev. A*, 80(5):053415, 2009.

[19] F. Mauger, C. Chandre, and T. Uzer. Strong field double ionization: The phase space perspective. *Phys. Rev. Lett.*, 102(17):173002, 2009.

[20] S. L. Haan, Z. S. Smith, K. N. Shomsky, P. W. Plantinga, and T. L. Atallah. Anticorrelated electrons from high-intensity nonsequential double ionization of atoms. *Phys. Rev. A*, 81(2):023409, 2010.

[21] F. Krausz and M. Ivanov. Attosecond physics. *Rev. Mod. Phys.*, 81(1):163–234, 2009.

[22] P. Agostini and L. F. DiMauro. The physics of attosecond light pulses. *Reports on Progress in Physics*, 67(6):813, 2004.

[23] J. Feldhaus, J. Arthur, and J. B. Hastings. X-ray free-electron lasers. *J. Phys. B*, 38(9):S799, 2005.

[24] W. Ackermann, G. Asova, V. Ayvazyan, A. Azima, N. Baboi, J. Bähr, V. Balandin, B. Beutner, A. Brandt, A. Bolzmann, R. Brinkmann, O. I. Brovko, M. Castellano, P. Castro, L. Catani, E. Chiadroni, S. Choroba, A. Cianchi, J. T. Costello, D. Cubaynes, J. Dardis, W. Decking, H. Delsim-Hashemi, A. Delserieys, G. Di Pirro, M. Dohlus, S. Düsterer, A. Eckhardt, H. T. Edwards, M. B. Faatz, J. Feldhaus, K. Flöttmann, J. Frisch, L. Fröhlich, T. Garvey, U. Gensch, Ch. Gerth, Görler, N. Golubeva, H.-J. Grabosch, M. Grecki, O. Grimm, K. Hacker, U. Hahn, J. H. Han, K. Honkavaara, T. Hott, M. Hüning, Y. Ivanisenko, E. Jaeschke, W. Jalmuzna, T. Jezynski, R. Kammering, V. Katalev, K. Kavanagh, E. T. Kennedy, S. Khodyachykh, K. Klose, V. Kocharyan, M. Körfer, M. Kollewe, W. Koprek, S. Korepanov, D. Kostin, M. Krassilnikov, G. Kube, M. Kuhlmann, C. L. S. Lewis, L. Lilje, T. Limberg, D. F. Lipka, Löhl, H. Luna, M. Luong, M. Martins, M. Meyer, P. Michelato, V. Miltchev, W. D. Möller, L. Monaco, W. F. O. Müller, O. Napieralski, O. Napoly, P. Nicolosi, D. Nölle, T. Nuez, A. Oppelt, C. Pagani, R. Paparella, N. Pchalek, J. Pedregosa-Gutierrez, B. Petersen, B. Petrosyan, G. Petrosyan, L. Petrosyan, J. Pflüger, E. Plönjes, L. Poletto, K. Pozniak, E. Prat, D. Proch, P. Pucyk,

P. Radcliffe, H. Redlin, K. Rehlich, M. Richter, M. Roehrs, J. Roensch, R. Romaniuk, M. Ross, J. Rossbach, V. Rybnikov, M. Sachwitz, E. L. Saldin, W. Sandner, H. Schlarb, B. Schmidt, M. Schmitz, P. Schmüser, J. R. Schneider, E. A. Schneidmiller, S. Schnepp, S. Schreiber, M. Seide, D. Sertore, A. V. Shabunov, C. Simon, S. Simrock, E. Sombrowski, A. A. Sorokin, P. Spanknebel, R. Spesyvtsev, L. Staykov, B. Steffen, F. Stephan, F. Stulle, H. Thom, K. Tiedtke, M. Tischer, S. Toleikis, R. Treusch, D. Trines, I. Tsakov, E. Vogel, T. Weiland, Weise H., M. Wellhöfer, M. Wendt, I. Will, A. Winter, K. Wittenburg, W. Wurth, Yeates, M. V. Yurkov, Zagorodnov I., and K. Zapfe. Operation of a free-electron laser from the extreme ultraviolet to the water window. *Nature Photonics*, 1:336, 2007.

[25] T. Shintake, H. Tanaka, T. Himeji, T. Tanaka, K. Togawa, M. Yabashi, Y. Otake, Y. Asano, T. Bizen, T. Fukui, S. Goto, A. Higashiya, T. Hirono, N. Hosoda, T. Inagaki, S. Inoue, M. Ishii, Y. Kim, H. Kimura, M. Kitamura, T. Kobayashi, H. Maesaka, T. Masuda, S. Matsui, T. Matsushita, X. Marchal, M. Nagasono, H. Ohashi, T. Ohata, T. Ohshima, K. Onoe, K. Shirasawa, T. Takagi, S. Takahashi, M. Takeuchi, K. Tamasaku, R. Tanaka, Y. Tanaka, T. Tanikawa, T. Togashi, S. Wu, A. Yamashita, K. Yanagida, C. Zhang, H. Kitamura, and T. Ishikawa. A compact free-electron laser for generating coherent radiation in the extreme ultraviolet region. *Nature Photonics*, 2(9):555, 2008.

[26] Y. Ding, A. Brachmann, F.-J. Decker, D. Dowell, P. Emma, J. Frisch, S. Gilevich, G. Hays, Ph. Hering, Z. Huang, R. Iverson, H. Loos, A. Miahnahri, H.-D. Nuhn, D. Ratner, J. Turner, J. Welch, W. White, and J. Wu. Measurements and simulations of ultralow emittance and ultrashort electron beams in the linac coherent light source. *Phys. Rev. Lett.*, 102(25):254801, 2009.

[27] A. A. Sorokin, S. V. Bobashev, K. Tiedtke, and M. Richter. Multi-photon ionization of molecular nitrogen by femtosecond soft x-ray fel pulses. *J. Phys. B*, 39(14):L299, 2006.

[28] Y. Nabekawa, H. Hasegawa, E. J. Takahashi, and K. Midorikawa. Production of doubly charged helium ions by two-photon absorption of an intense sub-10-fs soft x-ray pulse at 42 ev photon energy. *Phys. Rev. Lett.*, 94(4):043001, 2005.

[29] H. Hasegawa, E. J. Takahashi, Y. Nabekawa, K. L. Ishikawa, and K. Midorikawa. Multiphoton ionization of *he* by using intense high-order harmonics in the soft-x-ray region. *Phys. Rev. A*, 71(2):023407, 2005.

[30] H. Wabnitz, A. R. B. de Castro, P. Gürtler, T. Laarmann, W. Laasch, J. Schulz, and T. Möller. Multiple ionization of rare gas atoms irradiated with intense vuv radiation. *Phys. Rev. Lett.*, 94(2):023001, 2005.

[31] E. P. Benis, D. Charalambidis, T. N. Kitsopoulos, G. D. Tsakiris, and P. Tzallas. Two-photon double ionization of rare gases by a superposition of harmonics. *Phys. Rev. A*, 74(5):051402, 2006.

[32] A. Föhlisch, M. Nagasono, M. Deppe, E. Suljoti, F. Hennies, A. Pietzsch, and W. Wurth. High-brilliance free-electron-laser photoionization of n_2 : Ground-state depletion and radiation-field-induced modifications. *Phys. Rev. A*, 76(1):013411, 2007.

[33] M. Nagasono, E. Suljoti, A. Pietzsch, F. Hennies, M. Wellhöfer, J.T. Hoeft, M. Martins, W. Wurth, R. Treusch, J. Feldhaus, J.R. Schneider, and A. Föhlisch. Resonant two-photon absorption of extreme-ultraviolet free-electron-laser radiation in helium. *Phys. Rev. A*, 75(5):051406, 2007.

[34] A. A. Sorokin, M. Wellhöfer, S. V. Bobashev, K. Tiedtke, and M. Richter. X-ray-laser interaction with matter and the role of multiphoton ionization: Free-electron-laser studies on neon and helium. *Phys. Rev. A*, 75(5):051402, 2007.

[35] A. A. Sorokin, S. V. Bobashev, T. Feigl, K. Tiedtke, H. Wabnitz, and M. Richter. Photoelectric effect at ultrahigh intensities. *Phys. Rev. Lett.*, 99(21):213002, 2007.

[36] R. Moshammer, Y. H. Jiang, L. Foucar, A. Rudenko, Th. Ergler, C. D. Schröter, S. Lüdemann, K. Zrost, D. Fischer, J. Titze, T. Jahnke, M. Schöffler, T. Weber, R. Dörner, T. J. M. Zouros, A. Dorn, T. Ferger, K. U. Kühnel, S. Düsterer, R. Treusch, P. Radcliffe, E. Plönjes, and J. Ullrich. Few-photon multiple ionization of ne and ar by strong free-electron-laser pulses. *Phys. Rev. Lett.*, 98(20):203001, 2007.

[37] A. Rudenko, L. Foucar, M. Kurka, Th. Ergler, K. U. Kühnel, Y. H. Jiang, A. Voitkiv, B. Najjari, A. Kheifets, S. Lüdemann, T. Havermeier, M. Smolarski, S. Schössler, K. Cole, M. Schöffler, R. Dörner, S. Düsterer, W. Li, B. Keitel, R. Treusch, M. Gensch, C. D. Schröter, R. Moshammer, and J. Ullrich. Recoil-ion momentum distributions for two-photon double ionization of he and ne by 44 ev free-electron laser radiation. *Phys. Rev. Lett.*, 101(7):073003, 2008.

[38] R. Mitzner, A. A. Sorokin, B. Siemer, S. Roling, M. Rutkowski, H. Zacharias, M. Neeb, T. Noll, F. Siewert, W. Eberhardt, M. Richter, P. Juranic, K. Tiedtke, and J. Feldhaus. Direct autocorrelation of soft-x-ray free-electron-laser pulses by time-resolved two-photon double ionization of he. *Phys. Rev. A*, 80(2):025402, 2009.

[39] M. Richter, M. Y. Amusia, S. V. Bobashev, T. Feigl, P. N. Juranić, M. Martins, A. A. Sorokin, and K. Tiedtke. Extreme ultraviolet laser excites atomic giant resonance. *Phys. Rev. Lett.*, 102(16):163002, 2009.

[40] Y. H. Jiang, A. Rudenko, M. Kurka, K. U. Kühnel, Th. Ergler, L. Foucar, M. Schöffler, S. Schössler, T. Havermeier, M. Smolarski, K. Cole, R. Dörner, S. Düsterer, R. Treusch, M. Gensch, C. D. Schröter, R. Moshammer, and J. Ullrich. Few-photon multiple ionization of n_2 by extreme ultraviolet free-electron laser radiation. *Phys. Rev. Lett.*, 102(12):123002, 2009.

[41] M. Kurka, A. Rudenko, L. Foucar, K. U. Kühnel, Y. H. Jiang, Th. Ergler, T. Havermeier, M. Smolarski, S. Schössler, K. Cole, M. Schöffler, R. Dörner, M. Gensch, S. Düsterer, R. Treusch, S. Fritzsche, A. N. Grum-Grzhimailo, E. V. Gryzlova, N. M. Kabachnik, C.D. Schröter, R. Moshammer, and J. Ullrich. Two-photon double ionization of ne by free-electron laser radiation: a kinematically complete experiment. *J. Phys. B*, 42(14):141002, 2009.

[42] Y. H. Jiang, A. Rudenko, M. Kurka, K. U. Kühnel, L. Foucar, Th. Ergler, S. Lüdemann, K. Zrost, T. Ferger, D. Fischer, A. Dorn, J. Titze, T. Jahnke, M. Schöffler, S. Schössler, T. Havermeier, M. Smolarski, K. Cole, R. Dörner, T. J. M. Zouros, S. Düsterer, R. Treusch, M. Gensch, C.D. Schröter, R. Moshammer, and J. Ullrich. Euv-photon-induced multiple ionization and fragmentation dynamics: from atoms to molecules. *J. Phys. B*, 42(13):134012, 2009.

[43] H. Fukuzawa, K. Motomura, X.-J. Liu, G. Prümper, M. Okunishi, K. Ueda, N. Saito, H. Iwayama, K. Nagaya, M. Yao, M. Nagasono, A. Higashiya, M. Yabashi, T. Ishikawa, H. Ohashi, and H. Kimura. Ion momentum spectroscopy of n 2 and o 2 molecules irradiated by euv free-electron laser pulses. *J. Phys. B*, 42(18):181001, 2009.

[44] K. Motomura, H. Fukuzawa, L. Foucar, X.-J. Liu, G. Prümper, K. Ueda, N. Saito, H. Iwayama, K. Nagaya, H. Murakami, M. Yao, A. Belkacem, M. Nagasono, A. Higashiya, M. Yabashi, T. Ishikawa, H. Ohashi, and H. Kimura. Multiple ionization of atomic argon irradiated by euv free-electron laser pulses at 62 nm: evidence of sequential electron strip. *J. Phys. B*, 42(22):221003, 2009.

[45] T. Sato, T. Okino, K. Yamanouchi, A. Yagishita, F. Kannari, K. Yamakawa, K. Midorikawa, H. Nakano, M. Yabashi, M. Nagasono, and M. Ishikawa. Dissociative two-photon ionization of n2 in extreme ultraviolet by intense self-amplified spontaneous emission free electron laser light. *Applied Physics Letters*, 92(15):154103, 2008.

[46] P. Lambropoulos and L. A. A. Nikolopoulos. Angular distributions in double ionization of helium under xuv sub-femtosecond radiation. *New Journal of Physics*, 10(2):025012, 2008.

[47] E. Foumouo, G. L. Kamta, G. Edah, and B. Piraux. Theory of multiphoton single and double ionization of two-electron atomic systems driven by short-wavelength electric fields: An ab initio treatment. *Phys. Rev. A*, 74(6):063409, 2006.

[48] R. Shakeshaft. Two-photon single and double ionization of helium. *Phys. Rev. A*, 76(6):063405, 2007.

[49] D. A. Horner, F. Morales, T. N. Rescigno, F. Martín, and C. W. McCurdy. Two-photon double ionization of helium above and below the threshold for sequential ionization. *Phys. Rev. A*, 76(3):030701, 2007.

[50] A. S. Kheifets, A. I. Ivanov, and I. Bray. Different escape modes in two-photon double ionization of helium. *Phys. Rev. A*, 75(2):024702, 2007.

[51] I. A. Ivanov and A. S. Kheifets. Two-photon double ionization of helium in the region of photon energies $42 - -50ev$. *Phys. Rev. A*, 75(3):033411, 2007.

[52] D. A. Horner, T. N. Rescigno, and C. W. McCurdy. Decoding sequential versus nonsequential two-photon double ionization of helium using nuclear recoil. *Phys. Rev. A*, 77(3):030703, 2008.

[53] D. A. Horner, C. W. McCurdy, and T. N. Rescigno. Triple differential cross sections and nuclear recoil in two-photon double ionization of helium. *Phys. Rev. A*, 78(4):043416, 2008.

[54] M. G. Makris and P. Lambropoulos. Theoretical interpretation of multiphoton ionization of neon by soft-x-ray intense radiation. *Phys. Rev. A*, 77(2):023401, 2008.

[55] J. Feist, S. Nagele, R. Pazourek, E. Persson, B. I. Schneider, L. A. Collins, and J. Burgdörfer. Nonsequential two-photon double ionization of helium. *Phys. Rev. A*, 77(4):043420, 2008.

[56] X. Guan, K. Bartschat, and B. I. Schneider. Dynamics of two-photon double ionization of helium in short intense xuv laser pulses. *Phys. Rev. A*, 77(4):043421, 2008.

[57] P. Antoine, E. Foumouo, B. Piraux, T. Shimizu, H. Hasegawa, Y. Nabekawa, and K. Midorikawa. Two-photon double ionization of helium: An experimental lower bound of the total cross section. *Phys. Rev. A*, 78(2):023415, 2008.

[58] D. A. Horner, T. N. Rescigno, and C. W. McCurdy. Nuclear recoil cross sections from time-dependent studies of two-photon double ionization of helium. *Phys. Rev. A*, 81(2):023410, 2010.

[59] L. Hamonou, W. van der Hart, K. M. Dunseath, and M. Terao-Dunseath. Two-photon emission of a 2p electron from ne + and consequences for sequential double ionization of ne. *J. Phys. B*, 41(1):015603, 2008.

[60] A. S. Kheifets. Photoelectron angular correlation pattern in sequential two-photon double ionization of neon. *J. Phys. B*, 42(13):134016, 2009.

[61] S. Fritzsche, A. N. Grum-Grzhimailo, E. V. Gryzlova, and N. M. Kabachnik. Angular distributions and angular correlations in sequential two-photon double ionization of atoms. *J. Phys. B*, 41(16):165601, 2008.

[62] A. S. Kheifets. Sequential two-photon double ionization of noble gas atoms. *J. Phys. B*, 40(22):F313, 2007.

[63] L. A. A. Nikolopoulos and P. Lambropoulos. Time-dependent theory of double ionization of helium under xuv radiation. *J. Phys. B*, 40(7):1347, 2007.

[64] J. Feist, R. Pazourek, S. Nagele, E. Persson, B. I. Schneider, L. A. Collins, and J. Burgdörfer. Electron correlation in two-photon double ionization of helium from attosecond to xfel pulses. *J. Phys. B*, 42(13):134014, 2009.

[65] L. Hamonou, M. A. Lysaght, and H. W. van der Hart. Influence of autoionizing states on the pulse-length dependence of strong-field ne + photoionization at 38.4 ev. *J. Phys. B*, 43(4):045601, 2010.

[66] M. Drescher, M. Hentschel, R. Kienberger, Gabriel T., C. Spielmann, G. A. Reider, P. B. Corkum, and F. Krausz. X-ray Pulses Approaching the Attosecond Frontier. *Science*, 291(5510):1923–1927, 2001.

[67] E. Goulielmakis, M. Uiberacker, R. Kienberger, A. Baltuska, V. Yakovlev, A. Scrinzi, Th. Westerwalbesloh, U. Kleineberg, U. Heinzmann, M. Drescher, and F. Krausz. Direct Measurement of Light Waves. *Science*, 305(5688):1267–1269, 2004.

[68] M. Ueberacker, Th. Uphues, M. Schultze, A. J. Verhoef, V. Yakovlev, M. F. Kling, J. Rauschenberger, N. M. Kabachnik, H. Schröder, M. Lezius, K. L. Kompa, H.G. Muller, M. J. J. Vrakking, S. Hendel, U. Kleineberg, U. Heinzmann, M. Drescher, and F. Krausz. Attosecond real-time observation of electron tunnelling in atoms. *Nature*, 446(7136):627, 2007.

[69] E. Gagnon, P. Ranitovic, X.M. Tong, C. L. Cocke, M. M. Murnane, H. C. Kapteyn, and A. S. Sandhu. Soft X-ray-Driven Femtosecond Molecular Dynamics. *Science*, 317(5843):1374–1378, 2007.

[70] A. S. Sandhu, E. Gagnon, R. Santra, V..a Sharma, W. Li, P. Ho, P. Ranitovic, C. L. Cocke, M. M. Murnane, and H. C. Kapteyn. Observing the Creation of Electronic Feshbach Resonances in Soft X-ray-Induced O2 Dissociation. *Science*, 322(5904):1081–1085, 2008.

[71] A. M. Lindenberg, J. Larsson, K. Sokolowski-Tinten, K. J. Gaffney, C. Blome, O. Synnergren, J. Sheppard, C. Caleman, A. G. MacPhee, D. Weinstein, D. P. Lowney, T. K. Allison, T. Matthews, R. W. Falcone, A. L. Cavalieri, D. M. Fritz, S. H. Lee, P. H. Bucksbaum, D. A. Reis, J. Rudati, P. H. Fuoss, C. C. Kao, D. P. Siddons, R. Pahl, J. Als-Nielsen, S. Duesterer, R. Ischebeck, H. Schlarb, H. Schulte-Schrepping, Th. Tschentscher, J. Schneider, D. von der Linde, O. Hignette, F. Sette, H. N. Chapman, R. W. Lee, T. N. Hansen, S. Techert, J. S. Wark, M. Bergh, G. Huldt, D. van der Spoel, N. Timneanu, J. Hajdu, R. A. Akre, E. Bong, P. Krejcik, J. Arthur, S. Brennan, K. Luening, and J. B. Hastings. Atomic-Scale Visualization of Inertial Dynamics. *Science*, 308(5720):392–395, 2005.

[72] F. Krasniqi, B. Najjari, L. Strüder, D. Rolles, A. Voitkiv, and J. Ullrich. Imaging molecules from within: Ultrafast angström-scale structure determination of molecules via photoelectron holography using free-electron lasers. *Phys. Rev. A*, 81(3):033411, 2010.

[73] A. H. Zewail. Femtochemistry: Atomic-scale dynamics of the chemical bond. *The Journal of Physical Chemistry A*, 104(24):5660–5694, 2000.

[74] M. Weckenbrock, D. Zeidler, A. Staudte, Th. Weber, M. Schöffler, M. Meckel, S. Kammer, M. Smolarski, O. Jagutzki, V. R. Bhardwaj, D. M. Rayner, D. M. Villeneuve, P. B. Corkum, and R. Dörner. Fully differential rates for femtosecond multiphoton double ionization of neon. *Phys. Rev. Lett.*, 92(21):213002, 2004.

[75] A. Rudenko, V. L. B. de Jesus, Th. Ergler, K. Zrost, B. Feuerstein, C. D. Schröter, R. Moshammer, and J. Ullrich. Correlated two-electron momentum spectra for strong-field nonsequential double ionization of he at 800 nm. *Phys. Rev. Lett.*, 99(26):263003, 2007.

[76] A. Knapp, A. Kheifets, I. Bray, Th. Weber, A. L. Landers, S. Schössler, T. Jahnke, J. Nickles, S. Kammer, O. Jagutzki, L. Ph. H. Schmidt, T. Osipov, J. Rösch, M. H. Prior, H. Schmidt-Böcking, C. L. Cocke, and R. Dörner. Mechanisms of photo double ionization of helium by 530 ev photons. *Phys. Rev. Lett.*, 89(3):033004, 2002.

[77] E. Eremina, X. Liu, H. Rottke, W. Sandner, M. G. Schätzel, A. Dreischuh, G. G. Paulus, H. Walther, R. Moshammer, and J. Ullrich. Influence of molecular structure on double ionization of n_2 and o_2 by high intensity ultrashort laser pulses. *Phys. Rev. Lett.*, 92(17):173001, 2004.

[78] D. Zeidler, A. Staudte, A. B. Bardon, D. M. Villeneuve, R. Dörner, and P. B. Corkum. Controlling attosecond double ionization dynamics via molecular alignment. *Phys. Rev. Lett.*, 95(20):203003, 2005.

[79] D. Akoury, K. Kreidi, T. Jahnke, Th. Weber, A. Staudte, M. Schoffler, N. Neumann, J. Titze, L. Ph. H. Schmidt, A. Czasch, O. Jagutzki, R. A. Costa Fraga, R. E. Grisenti, R. Diez Muino, N. A. Cherepkov, S. K. Semenov, P. Ranitovic, C. L. Cocke, T. Osipov, H. Adaniya, J. C. Thompson, M. H. Prior, A. Belkacem, A. L. Landers, H. Schmidt-Bocking, and R. Dorner. The Simplest Double Slit: Interference and Entanglement in Double Photoionization of H2. *Science*, 318(5852):949–952, 2007.

[80] M. S. Schöffler, J. Titze, N. Petridis, T. Jahnke, K. Cole, L. Ph. H. Schmidt, A. Czasch, D. Akoury, O. Jagutzki, J. B. Williams, N. A. Cherepkov, S. K. Semenov, C. W. McCurdy, T. N. Rescigno, C. L. Cocke, T. Osipov, S. Lee, M. H. Prior, A. Belkacem, A. L. Landers, H. Schmidt-Bocking, Th. Weber, and R. Dorner. Ultrafast Probing of Core Hole Localization in N2. *Science*, 320(5878):920–923, 2008.

[81] R. Moshammer, J. Ullrich, M. Unverzagt, W. Schmitt, and H. Schmidt-Böcking. A 4π recoil-ion electron momentum analyzer: A high-resolution 'microscope' for the investigation of the dynamics of atomic, molecular and nuclear reactions. *Nuclear Instruments and Methods in Physics Research Section B: Beam Interactions with Materials and Atoms*, 108(4):425 – 445, 1996.

[82] R. Dörner, V. Mergel, O. Jagutzki, L. Spielberger, J. Ullrich, R. Moshammer, and H. Schmidt-Böcking. Cold target recoil ion momentum spectroscopy: a [']momentum microscope' to view atomic collision dynamics. *Physics Reports*, 330(2-3):95 – 192, 2000.

[83] J. Ullrich, R. Moshammer, A. Dorn, R. Dörner, L. Ph. H. Schmidt, and H. Schmidt-Böcking. Recoil-ion and electron momentum spectroscopy: reaction-microscopes. *Reports on Progress in Physics*, 66(9):1463, 2003.

[84] V.L.B. de Jesus, A. Rudenko, B. Feuerstein, K. Zrost, C.D. Schröter, R. Moshammer, and J. Ullrich. Reaction microscopes applied to study atomic and molecular fragmentation in intense laser fields: non-sequential double ionization of helium. *J. el. spec. rel. phen.*, 141:127, 2004.

[85] A. Rudenko, B. Feuerstein, K. Zrost, V. L. B. de Jesus, Th. Ergler, C. Dimopoulou, C.D. Schröter, R. Moshammer, and J. Ullrich. Fragmentation dynamics of molecular hydrogen in strong ultrashort laser pulses. *J. Phys. B*, 38(5):487, 2005.

[86] A. S. Alnaser, B. Ulrich, X. M. Tong, I. V. Litvinyuk, C. M. Maharjan, P. Ranitovic, T. Osipov, R. Ali, S. Ghimire, Z. Chang, C. D. Lin, and C. L. Cocke. Simultaneous real-time tracking of wave packets evolving on two different potential curves in h_2^+ and d_2^+. *Phys. Rev. A*, 72(3):030702, 2005.

[87] Th. Ergler, A. Rudenko, B. Feuerstein, K. Zrost, C. D. Schröter, R. Moshammer, and J. Ullrich. Time-resolved imaging and manipulation of h_2 fragmentation in intense laser fields. *Phys. Rev. Lett.*, 95(9):093001, 2005.

[88] Th. Ergler, A. Rudenko, B. Feuerstein, K. Zrost, C. D. Schröter, R. Moshammer, and J. Ullrich. Spatiotemporal imaging of ultrafast molecular motion: Collapse and revival of the d_2^+ nuclear wave packet. *Phys. Rev. Lett.*, 97(19):193001, 2006.

[89] M. Meckel, D. Comtois, D. Zeidler, A. Staudte, D. Pavicic, H. C. Bandulet, H. Pepin, J. C. Kieffer, R. Dorner, D. M. Villeneuve, and P. B. Corkum. Laser-Induced Electron Tunneling and Diffraction. *Science*, 320(5882):1478–1482, 2008.

[90] I. A. Bocharova, H. Mashiko, M. Magrakvelidze, D. Ray, P. Ranitovic, C. L. Cocke, and I. V. Litvinyuk. Direct coulomb-explosion imaging of coherent nuclear dynamics induced by few-cycle laser pulses in light and heavy hydrogen. *Phys. Rev. A*, 77(5):053407, 2008.

[91] Y. H. Jiang, A. Rudenko, E. Plésiat, L. Foucar, M. Kurka, K. U. Kühnel, Th. Ergler, J. F. Pérez-Torres, F. Martín, O. Herrwerth, M. Lezius, M. F. Kling, J. Titze, T. Jahnke, R. Dörner, J. L. Sanz-Vicario, M. Schöffler, J. van Tilborg, A. Belkacem, K. Ueda, T. J. M. Zouros, S. Düsterer, R. Treusch, C. D. Schröter, R. Moshammer, and J. Ullrich. Tracing direct and sequential two-photon double ionization of d_2 in femtosecond extreme-ultraviolet laser pulses. *Phys. Rev. A*, 81(2):021401, 2010.

[92] A. H. Zewail. Laser femtochemistry. *Science*, 242(4886):1645, 1988.

[93] A. H. Zewail. Femtosecond transition-state dynamics. *Faraday Discuss. Chem. Soc.*, 91:207, 1991.

[94] A. H. Zewail. Femtochemistry: Recent progress in studies of dynamics and control of reactions and their transition states. *J. Phys. Chem.*, 100(31):12701, 1996.

[95] M. Kremer, B. Fischer, B. Feuerstein, V. L. B. de Jesus, V. Sharma, C. Hofrichter, A. Rudenko, U. Thumm, C. D. Schröter, R. Moshammer, and J. Ullrich. Electron localization in molecular fragmentation of $h2$ by carrier-envelope phase stabilized laser pulses. *Phys. Rev. Lett.*, 103(21):213003, 2009.

[96] E. Goulielmakis, Z.-H. Loh, A. Wirth, R. Santra, N. Rohringer, V. S. Yakovlev, S. Zherebtsov, T. Pfeifer, A. M. Azzeer, M. F. Kling, S. R. Leone, and F. Krausz. Real-time observation of valence electron motion. *Nature*, 466(7307):739, 1996.

[97] Y. H. Jiang, A. Rudenko, J. F. Pérez-Torres, O. Herrwerth, L. Foucar, M. Kurka, K. U. Kühnel, M. Toppin, E. Plésiat, F. Morales, F. Martín, M. Lezius, M. F. Kling, T. Jahnke, R. Dörner, J. L. Sanz-Vicario, J. van Tilborg, A. Belkacem, M. Schulz, K. Ueda, T. J. M. Zouros, S. Düsterer, R. Treusch, C. D. Schröter, R. Moshammer, and J. Ullrich. Investigating two-photon double ionization of d_2 by xuv-pump–xuv-probe experiments. *Phys. Rev. A*, 81(5):051402, 2010.

[98] Y. H. Jiang, A. Rudenko, O. Herrwerth, L. Foucar, M. Kurka, K. U. Kühnel, M. Lezius, M. F. Kling, J. van Tilborg, A. Belkacem, K. Ueda, S. Düsterer, R. Treusch, C. D. Schröter, R. Moshammer, and J. Ullrich. Ultrafast extreme ultraviolet induced isomerization of acetylene cations. *Phys. Rev. Lett.*, 105(26):263002, 2010.

[99] A. Staudte. *Subfemtosecond Electron Dynamics of H^2 in Strong Fields*. Dissertation, Johann Wolfgang Goethe Universität, Frankfurt am Main, 2005.

[100] F. Fabre, G. Petite, P. Agostini, and M. Clement. Multiphoton above-threshold ionisation of xenon at 0.53 and 1.06 μm. *J. Phys. B*, 15(9):1353, 1982.

[101] P. Lambropoulos. Topics on multiphoton processes in atoms. *Adv. At. Mol. Phys.*, 12:87, 1976.

[102] M. Lundqvist, D. Edvardsson, P. Baltzer, M. Larsson, and B. Wannberg. Observation of predissociation and tunnelling processes in o_2^{2+}: a study using doppler free kinetic energy release spectroscopy and ab initio ci calculations. *J. Phys. B*, 29(3):499, 1996.

[103] A. D. McNaught and A. Wilkinson. *IUPAC Compendium of Chemical Terminology*. Royal Society of Chemistry, 1997.

[104] W. Demptröder. *Molecular physics : theoretical principles and experimental methods*. Wiley-VCH, Weinheim, 1. auflage edition, 2005.

[105] DESY-TESLA-FEL-2002-01. *SASE FEL at the TESLA Facility, Phase 2*. Technischer bericht, DESY, Hamburg, 2002.

[106] K. Wille. *Physik der Teilchenbeschleuniger und Synchrotronstrahlungsquellen*. B.G.Teubner, Stuttgart, 2. auflage edition, 1986.

[107] J. M. J. Madey. Stimulated emission of bremsstrahlung in a periodic magnetic field. *Journal of Applied Physics*, 42(5):1906–1913, 1971.

[108] T. Brabec and F. Krausz. Intense few-cycle laser fields: Frontiers of nonlinear optics. *Rev. Mod. Phys.*, 72(2):545–591, 2000.

[109] C. Pellegrini. Progress toward a soft x-ray fel. *Nuclear Instruments and Methods in Physics Research*, A272:364, 1988.

[110] J. R. Schneider, R. H. Nielsen, J. Feldhaus, B. Keitel, W. Laasch, P. Schmueser, B. Sonntag, and K. Tiedtke. *The free electron laser Hamburg*. Deutsches Elektronen-Synchrotron DESY, 2007.

[111] A. Becker and F. H. M. Faisal. Intense-field many-body s -matrix theory. *J. Phys. B*, 38(3):R1, 2005.

[112] Dokumantation scss. Available online at http://www-xfel.spring8.or.jp/index.htm.

[113] T. Shintake, H. Tanaka, T. Hara, T. Tanaka, K. Togawa, M. Yabashi, Y. Otake, Y. Asano, T. Fukui, T. Hasegawa, A. Higashiya, N. Hosoda, T. Inagaki, S. Inoue, Y. Kim, M. Kitamura, N. Kumagai, H. Maesaka, S. Matsui, M. Nagasono, T. Ohshima, T. Sakurai, K. Tamasaku, Y. Tanaka, T. Tanikawa, T. Togashi, and S. Wu. Stable operation of a self-amplified spontaneous-emission free-electron laser in the extremely ultraviolet region. *Phys. Rev. ST Accel. Beams*, 12(7):070701, 2009.

[114] R. Dörner, V. Mergel, O. Jagutzki, L. Spielberger, J. Ullrich, R. Moshammer, and H. Schmidt-Böcking. Cold target recoil ion momentum spectroscopy: a [']momentum microscope' to view atomic collision dynamics. *Physics Reports*, 330(2-3):95 – 192, 2000.

[115] J. Ullrich and R. Moshammer. Recoil-ion and electron momentum spectroscopy: reactionmicroscopes. *Rep.Prog.Phys.*, 66:1463, 2003.

[116] D. Fischer. *Mehr-Teilchen-Dynamik in der Einfach- und Doppelionisation von Helium durch geladene Projektile.* PhD thesis, Universität Heidelberg, 2003.

[117] D. R. Miller. Free jet sources. In *Atomic and Molecular Beam Methods*, pages 14–53. Oxford University Press, 1988.

[118] A. Czasch. *Doppelt hoch angeregte Zustände von Helium: Partielle Wirkungsquersschnitte und Winkelverteilungen der Elektronenemission.* PhD thesis, Universität Frankfurt a.M., 2004.

[119] I. N. Bronstein. *Taschenbuch der Mathematik.* Verlag Harri Deutsch, 5. auflage edition, 2001.

[120] M. Kurka. *Zwei- und Drei-Photonen Doppelionisation von Helium und Neon am Freie-Elektronen-Laser in Hamburg.* Diplomarbeit, Ruprecht-Karls-Universität, Heidelberg, 2007.

[121] K. L. Brown and G. W. Tautfest. Faraday-cup monitors for high-energy electron beams. *Review of Scientific Instruments*, 27(9):696–702, 1956.

[122] Datasheet micos wt100 & wt85. Available online at http://www.micos-online.com.

[123] Datasheet pi s-325. Available online at http://www.physikinstrumente.com.

[124] Datasheet pi p-628. Available online at http://www.physikinstrumente.com.

[125] R. Mitzner, B. Siemer, M. Neeb, T. Noll, F. Siewert, S. Roling, M. Rutkowski, A. A. Sorokin, M. Richter, P. Juranic, K. Tiedtke, J. Feldhaus, W. Eberhardt, and H. Zacharias. Spatio-temporal coherence of free electron laser pulses in the soft x-ray regime. *Opt. Express*, 16(24):19909–19919, 2008.

[126] W. F. Schlotter, F. Sorgenfrei, T. Beeck, M. Beye, S. Gieschen, H. Meyer, M. Nagasono, A. Föhlisch, and W. Wurth. Longitudinal coherence measurements of an extreme-ultraviolet free-electron laser. *Opt. Lett.*, 35(3):372–374, 2010.

[127] N. Rohringer and R. Santra. X-ray nonlinear optical processes using a self-amplified spontaneous emission free-electron laser. *Phys. Rev. A*, 76(3):033416, 2007.

[128] C. Iaconis and I.A. Walmsley. Spectral phase interferometry for direct electric-field reconstruction of ultrashort optical pulses. *Opt. Lett.*, 23(10):792–794, 1998.

[129] U. Frühling, M. Wieland, M. Gensch, T. Gebert, B. Schutte, M. Krikunova, R. Kalms, F. Budzyn, O. Grimm, J. Rossbach, E. Plonjes, and M. Drescher. Single-shot terahertzfield-driven x-ray streak camera. *Nat. Photonics*, 3(9):523528, 2009.

[130] T. Pfeifer, Y. Jiang, S. Düsterer, R. Moshammer, and J. Ullrich. Partial-coherence method to model experimental free-electron laser pulse statistics. *Opt. Lett.*, 35(20):3441–3443, 2010.

[131] R. Moshammer, Th. Pfeifer, A. Rudenko, Y.H. Jiang, L. Foucar, M. Kurka, K. U. Kühnel, C.D. Schröter, J. Ullrich, O. Herrwerth, M. F. Kling, X.-J. Liu, K. Motomura, H. Fukuzawa, A. Yamada, K. Ueda, K. L. Ishikawa, K. Nagaya, H. Iwayama, A. Sugishima, Y. Mizoguchi, S. Yase, M. Yao, N. Saito, A. Belkacem, M. Nagasono, A. Higashiya, M. Yabashi, T. Ishikawa, H. Ohashi, H. Kimura, and T. Togashi. Second-order autocorrelation of xuv fel pulses via time resolved two-photon single ionization of he. *Submitted to Opt. Exp.*, 2011.

[132] I. A. Bocharova, A. S. Alnaser, U. Thumm, T. Niederhausen, D. Ray, C. L. Cocke, and I. V. Litvinyuk. Time-resolved coulomb-explosion imaging of nuclear wave-packet dynamics induced in diatomic molecules by intense few-cycle laser pulses. *Phys. Rev. A*, 83(1):013417, 2011.

[133] T. Aoto, K. Ito, Y. Hikosaka, A. Shibasaki, R. Hirayama, N. Yamamono, and E. Miyoshi. Inner-valence states of n2+ and the dissociation dynamics studied by threshold photoelectron spectroscopy and configuration interaction calculation. *J. Chem. Phys .*, 124(23):234306, 2006.

[134] Beebe. N. H. F., E. W. Thulstrup, and A. Andersen. Configuration interaction calculations of low?lying electronic states of o2,o2+, and o22+. *J. Chem. Phys .*, 64(5):2080–2093, 1976.

[135] A. Mitrushenkov, P. Palmieri, G. Chambaud, and P. Rosmus. Spin-orbit induced predissociation of the b2[sigma]g- and 22[sigma]g+ states of the o2+ ion. *Chem. Phys. Let.*, 378(5-6):463 – 469, 2003.

[136] E. W. Thulstrup and A. Andersen. Configuration interaction studies of bound, low-lying states of n_2^- , n_2 , n_2^+ and n_2^{2+}. *J. Phys. B*, 8(6):965, 1975.

[137] A. A. Wills, A. A. Cafolla, and J. Comer. The production of autoionizing states of atomic oxygen by the photodissociation of o 2. *J. Phys. B*, 24(18):3989, 1991.

[138] S. Hsieh and J. H. D. Eland. Direct and indirect dissociative double photoionization of diatomic molecules. *J. Phys. B*, 29(23):5795, 1996.

[139] W. Cao, S. De, K. P. Singh, S. Chen, M. S. Schöffler, A. S. Alnaser, I. A. Bocharova, G. Laurent, D. Ray, S. Zherebtsov, M. F. Kling, I. Ben-Itzhak, I. V. Litvinyuk, A. Belkacem, T. Osipov, T. Rescigno, and C. L. Cocke. Dynamic modification of the fragmentation of co^{q+} excited states generated with high-order harmonics. *Phys. Rev. A*, 82(4):043410, 2010.

[140] T. Odagiri, H. Miyagi, M. Murata, H. Fukuzawa, M. Kurokawa, M. Kitajima, and N. Kouchi. Inner-valence excited and multiply excited states of molecular oxygen around the double-ionization potential as probed by a pair of fluorescence photons. *J. Phys. B*, 42(5):055101, 2009.

[141] P. Bolognesi, D. B. Thompson, L. Avaldi, M. A. MacDonald, M. C. A. Lopes, D. R. Cooper, and G. C. King. Vibrationally selected $o^+ - o^+$ fragmentation of o_2 below the adiabatic double-ionization potential studied via electron-electron coincidence spectroscopy. *Phys. Rev. Lett.*, 82(10):2075–2078, 1999.

[142] S. De, I. A. Bocharova, M. Magrakvelidze, D. Ray, W. Cao, B. Bergues, U. Thumm, M. F. Kling, I. V. Litvinyuk, and C. L. Cocke. Tracking nuclear wave-packet dynamics in molecular oxygen ions with few-cycle infrared laser pulses. *Phys. Rev. A*, 82(1):013408, 2010.

[143] P. Johnsson, W. Siu, A. Gijsbertsen, J. Verhoeven, A. S. Meijer, W. van der Zande, and M. J. J. Vrakking. Velocity map imaging of atomic and molecular processes at the free electron laser in hamburg (flash). *J. Mod. Opt.*, 55(16):2693 – 2709, 2008.

[144] Y. Lu, Z.X. He, J.N. Cutler, S.H. Southworth, W.C. Stolte, and J.A.R. Samson. Dissociative photoionization study of o2. *Journal of Electron Spectroscopy and Related Phenomena*, 94(1-2):135 – 147, 1998.

[145] E. Foumouo, Ph. Antoine, B. Piraux, L. Malegat, H. Bachau, and R. Shakeshaft. Evidence for highly correlated electron dynamics in two-photon double ionization of helium. *J. Phys. B*, 41(5):051001, 2008.

[146] M. Kurka, J. Feist, D. A. Horner, A. Rudenko, Y. H. Jiang, K. U. Kühnel, L. Foucar, T. N. Rescigno, C. W. McCurdy, R. Pazourek, S. Nagele, M. Schulz, O. Herrwerth, M. Lezius, M. F. Kling, M. Schöffler, A. Belkacem, S. Düsterer, R. Treusch, B. I. Schneider, L. A. Collins, J. Burgdörfer, C.D. Schröter, R. Moshammer, and J. Ullrich. Differential cross sections for non-sequential double ionization of he by 52 ev photons from the free electron laser in hamburg, flash. *New J. Phys.*, 12(7):073035, 2010.

[147] K. Hoshina, A. Hishikawa, K. Kato, T. Sako, K. Yamanouchi, E. J. Takahashi, Y. Nabekawa, and K. Midorikawa. Dissociative ati of h 2 and d 2 in intense soft x-ray laser fields. *J. Phys. B*, 39(4):813, 2006.

[148] J. Colgan, M. S. Pindzola, and F. Robicheaux. Two-photon double ionization of the hydrogen molecule. *J. Phys. B*, 41(12):121002, 2008.

[149] F. Morales, F. Martn, Horner. D. A., T. N. Rescigno, and C. W. McCurdy. Two-photon double ionization of h 2 at 30 ev using exterior complex scaling. *J. Phys. B*, 42(13):134013, 2009.

[150] J. L. Sanz-Vicario, H. Bachau, and F. Martín. Time-dependent theoretical description of molecular autoionization produced by femtosecond xuv laser pulses. *Phys. Rev. A*, 73(3):033410, 2006.

[151] K. Ito, R.I. Hall, and M. Ukai. Dissociative photoionization of h2 and d2 in the energy region of 25-45 ev. 104(21):8449–8457, 1996.

[152] T. Havermeier. *Photoionisation und doppelt angeregte Zustände in Wasserstoff- und Deuterium-Molekülen*. Diplomathesis, Universität Frankfurt, Frankfurt, 2006.

[153] F. Martin, J. Fernandez, T. Havermeier, L. Foucar, Th. Weber, K. Kreidi, M. Schöffler, L. Schmidt, T. Jahnke, O. Jagutzki, A. Czasch, E. P. Benis, T. Osipov, A. L. Landers, A. Belkacem, M. H. Prior, H. Schmidt-Böcking, C. L. Cocke, and R. Dörner. Single photon-induced symmetry breaking of h2 dissociation. *Science*, 315(5812):629–633, 2007.

[154] M. Førre, S. Barmaki, and H. Bachau. Nuclear interference in the coulomb explosion of h_2^+ in short vuv laser fields. *Phys. Rev. Lett.*, 102(12):123001, 2009.

[155] J. F. Perez-Torres, F. Morales, J. L. Sanz-Vicario, and F. Martin. Asymmetric electron angular distributions in resonant dissociative photoionization of h2 with ultrashort xuv pulses. *Phys. Rev. A*, 80:011402, 2009.

[156] J. F. Pérez-Torres, F. Morales, J. L. Sanz-Vicario, and F. Martín. Asymmetric electron angular distributions in resonant dissociative photoionization of h_2 with ultrashort xuv pulses. *Phys. Rev. A*, 80(1):011402, 2009.

[157] C. D. Lin, X. M. Tong, and T. Morishita. Direct experimental visualization of atomic and electron dynamics with attosecond pulses. *J. Phys. B*, 39(13):S419, 2006.

[158] P. Agostini, F. Fabre, G. Mainfray, G. Petite, and N. K. Rahman. Free-free transitions following six-photon ionization of xenon atoms. *Phys. Rev. Lett.*, 42(17):1127–1130, 1979.

[159] R. R. Freeman, T. J. McIlrath, P. H. Bucksbaum, and M. Bashkansky. Pondermotive effects on angular distributions of photoelectrons. *Phys. Rev. Lett.*, 57(25):3156, 1986.

[160] G. G. Paulus, F. Grasbon, and H. Walther. Channel-closing-induced resonances in the above-threshold ionization plateau. *Phys. Rev. A*, 64:021401, 2001.

[161] N. Bohr. über die anwendung der quantentheorie auf den atombau. *Zeitschrift f. Physik*, 13(1):117, 1923.

[162] E. Eremina. *Electron correlation in multiple ionization of atoms and molecules by intense ultra-short laser pulses*. PhD thesis, Technische Universit/"at Berlin, Berlin, 2005.

[163] N. B. Delone and V. P. Krainov. Tunneling and barrier-suppression ionization of atoms and ions in a laser radiation field. *Physics - Uspekhi*, 41(5):469, 1998.

[164] K. Zrost. *Wechselwirkung von Atomen und kleinen Molekülen mit intensiven, ultrakurzen Laserpulsen.* Dissertation, Ruprecht-Karls-Universität, Heidelberg, 2005.

[165] S. Augst, D. D. Meyerhofer, D. Strickland, and S. L. Chint. Laser ionization of noble gases by coulomb-barrier suppression. *J. Opt. Soc. Am. B*, 8(4):858–867, 1991.

[166] I. Aleksakhin, N. Delone, I. Zapesochnyi, and V. Suran. Observation and study of two-electron multiphoton. ionization of atoms. *Sov. Phys. JETP*, 48:1814, 1979.

[167] A. L'Huillier, L.A. Lompre, G. Mainfray, and C. Manus. Multiply charged ions formed by multiphoton absorption processes in the continuum. *Phys. Rev. Lett.*, 49(26):447, 1982.

[168] F. H. M. Faisal. Multiple absorption of laser photons by atoms. *J. Phys. B*, 6:L89, 1973.

[169] H. R. Reis. Effect of an intense electromagnetic field on a weakly bound system. *Phys. Rev. A*, 5(22):1786, 1980.

[170] A. Szöke, K. C. Kulander, and J. N. Bardsley. Simple calculations on two-colour multiphoton ionization. *J. Phys. B*, 24:3165, 1991.

[171] D. N. Fittinghoff, P. R. Bolton, B. Chang, and K. C. Kulander. Observation of nonsequential double ionization of helium with optical tunneling. *Phys. Rev. Lett.*, 69(18):2642, 1992.

[172] A. l'Huillier, L. A. Lompre, G. Mainfray, and C. Manus. Multiply charged ions induced by multiphoton absorption in rare gases at 0.53 μ m. *Phys. Rev. A*, 27(5):2503–2512, 1983.

[173] A. l'Huillier, L. A. Lompre, G. Mainfray, and C. Manus. Multiply charged ions induced by multiphoton absorption in rare gases at 0.53 μm. *Phys. Rev. A*, 27(5):2503, 1983.

[174] B. Walker, B. Sheehy, L. F. DiMauro, P. Agostini, K. J. Schafer, and K. C. Kulander. Precision measurement of strong field double ionization of helium. *Phys. Rev. Lett.*, 73(9):1227, 1994.

[175] B. Walker, E. Mevel, B. Yang, and Chambaret-J. P. Breger, P., A. Antonetti, L. F. DiMauro, and P. Agostini. Double ionization in the perturbative and tunneling regimes. *Phys. Rev. A*, 48(2):R894, 1993.

[176] Augst S., A. Talebpour, S. L. Chin, Y. Beaudoin, and M. Chaker. Nonsequential triple ionization of argon atoms in a high-intensity laser field. *Phys. Rev. A*, 52(2):R917, 1995.

[177] A. Talebpour, S. Larochelle, and S. L. Chin. Non-sequential and sequential double ionization of no in an intense femtosecond ti:sapphire laser pulse. *J. Phys. B*, 30:L245, 1997.

[178] C. Cornaggia and Ph. Hering. Laser-induced non-sequential double ionization of small molecules. *J. Phys. B*, 31:L503, 1998.

[179] C. Guo, M. Li, J. P. Nibarger, and G. N. Gibson. Single and double ionization of diatomic molecules in strong laser fields. *Phys. Rev. A*, 58(6):R4271, 1998.

[180] P. Dietrich, N. H. Burnett, M. Ivanov, and P. B. Corkum. High-harmonic generation and correlated two-electron multiphoton ionization with elliptically polarized light. *Phys. Rev. A*, 50(5):R3585–R3588, 1994.

[181] K. J. Schafer, Yang B., L. F. DiMauro, and K. C. Kulander. Above threshold ionization beyond the high harmonic cutoff. *Phys. Rev. Lett.*, 70(11):1599, 1993.

[182] S. Dewald. *Erzeugung intensiver Lichtfelder mit einem Laseroszillator und deren Wechselwirkung mit Atomen*. Dissertation, Ruprecht-Karls-Universität, Heidelberg, 2006.

[183] B. Sheehy, R. Lafon, M. Widmer, B. Walker, L. F. DiMauro, P. A. Agostini, and K. C. Kulander. Single- and multiple-electron dynamics in the strong-field tunneling limit. *Phys. Rev. A*, 58(5):3942–3952, 1998.

[184] R. Moshammer, B. Feuerstein, W. Schmitt, A. Dorn, C. D. Schröter, J. Ullrich, H. Rottke, C. Trump, M. Wittmann, G. Korn, K. Hoffmann, and W. Sandner. Momentum distributions of ne^{n+} ions created by an intense ultrashort laser pulse. *Phys. Rev. Lett.*, 83(3):447, 200.

[185] Th. Weber, M. Weckenbrock, A. Staudte, L. Spielberger, O. Jagutzki, V. Mergel, F. Afaneh, G. Urbasch, M. Vollmer, H. Giessen, and R. Dörner. Recoil-ion momentum distributions for single and double ionization of helium in strong laser fields. *Phys. Rev. Lett.*, 84(3):443–446, 2000.

[186] B. Witzel, N. A. Papadogiannis, and D. Charalambidis. Charge-state resolved above threshold ionization. *Phys. Rev. Lett.*, 85(11):2268–2271, 2000.

[187] R. Moshammer, J. Ullrich, B. Feuerstein, D. Fischer, A. Dorn, C.D. Schröter, J. R. Lpez-Urrutia Crespo, C. Höhr, H. Rottke, C. Trump, M. Wittmann, G. Korn, K. Hoffmann, and W. Sandner. Strongly directed electron emission in non-sequential double ionization of ne by intense laser pulses. *J. Phys. B*, 36(6):L113, 2003.

[188] O. Herrwerth, A. Rudenko, M. Kremer, V. L. B. de Jesus, B. Fischer, G. Gademann, K. Simeonidis, A. Achtelik, Th. Ergler, B. Feuerstein, C.D. Schröter, R. Moshammer, and J. Ullrich. Wavelength dependence of sub-laser-cycle few-electron dynamics in strong-field multiple ionization. *New Journal of Physics*, 10(2):025007, 2008.

[189] V. L. B. de Jesus, B. Feuerstein, K. Zrost, D. Fischer, A. Rudenko, F. Afaneh, C.D. Schröter, R. Moshammer, and J. Ullrich. Atomic structure dependence of nonsequential double ionization of he, ne and ar in strong laser pulses. *J. Phys. B*, 37(8):L161, 2004.

[190] A. Rudenko, K. Zrost, B. Feuerstein, V. L. B. de Jesus, C. D. Schröter, R. Moshammer, and J. Ullrich. Correlated multielectron dynamics in ultrafast laser pulse interactions with atoms. *Phys. Rev. Lett.*, 93(25):253001, 2004.

[191] K. Zrost, A. Rudenko, Th. Ergler, B. Feuerstein, V. L. B. de Jesus, C.D. Schröter, R. Moshammer, and J. Ullrich. Multiple ionization of ne and ar by intense 25 fs laser pulses: few-electron dynamics studied with ion momentum spectroscopy. *J. Phys. B*, 39(13):S371, 2006.

[192] X. Liu, C. F. de Morisson Faria, W. Becker, and P. B. Corkum. Attosecond electron thermalization by laser-driven electron recollision in atoms. *J. Phys. B*, 39(16):L305, 2006.

[193] B. Feuerstein, R. Moshammer, and J. Ullrich. Nonsequential multiple ionization in intense laser pulses: interpretation of ion momentum distributions within the classical 'rescattering' model. *J. Phys. B*, 33(21):L823, 2000.

[194] X. Liu, H. Rottke, E. Eremina, W. Sandner, E. Goulielmakis, K. O. Keeffe, M. Lezius, F. Krausz, F. Lindner, M. G. Schätzel, G. G. Paulus, and H. Walther. Nonsequential double ionization at the single-optical-cycle limit. *Phys. Rev. Lett.*, 93(26):263001, 2004.

[195] H. Gimpel. *Erzeugung und Anwendung intensiver ultrakurzer Lichtpulse mit stabiler TrägerEinhüllendenPhase*. Dissertation, Ruprecht-Karls-Universität, Heidelberg, 2006.

[196] S. Chelkowski and A. D. Bandrauk. Asymmetries in strong-field photoionization by few-cycle laser pulses: Kinetic-energy spectra and semiclassical explanation of the asymmetries of fast and slow electrons. *Phys. Rev. A*, 71(5):053815, 2005.

[197] R. Schneider. *Aufbau eines Laserverstärkersystems und Anwendung bei Photoionisationsexperimenten*. Dissertation, Technischen Universität Berlin, Berlin, 2003.

[198] C. Le Blanc, P. Curley, and F. Salin. Gain-narrowing and gain-shifting of ultra-short pulses in ti: sapphire amplifiers. *Optics Communications*, 131(4-6):391 – 398, 1996.

[199] M. Nisoli, S. De Silvestri, and O. Svelto. Generation of high energy 10 fs pulses by a new pulse compression technique. *Applied Physics Letters*, 68(20):2793–2795, 1996.

[200] E. Goulielmakis, S. Koehler, B. Reiter, M. Schultze, A. J. Verhoef, E. E. Serebryannikov, A. M. Zheltikov, and F. Krausz. Ultrabroadband, coherent light source based on self-channeling of few-cycle pulses in helium. *Opt. Lett.*, 33(13):1407–1409, 2008.

[201] C. Yun, S. Chen, H. Wang, M. Chini, and Z. Chang. Temperature feedback control for long-term carrier-envelope phase locking. *Appl. Opt.*, 48:5127–5130, 2009.

[202] H. Wang, C. Li, J. Tackett, H. Mashiko, E. Nakamura, C. M.and Moon, and Z. Chang. Power locking of high-repetition-rate chirped pulse amplifiers. *Appl. Phys. B: Laser Opt.*, 89:275–279, 2007.

[203] R. Holzwarth, Th. Udem, T. W. Hänsch, J. C. Knight, W. J. Wadsworth, and P. St. J. Russell. Optical frequency synthesizer for precision spectroscopy. *Phys. Rev. Lett.*, 85(11):2264–2267, 2000.

[204] M. Kakehata, H. Takada, Y. Kobayashi, K. Torizuka, Y. Fujihira, T. Homma, and H. Takahashi. Single-shot measurement of carrier-envelope phase changes by spectral interferometry. *Opt. Lett.*, 26(18):1436–1438, 2001.

[205] C. A. Haworth, L. E. Chipperfield, J. S. Robinson, P. L. Knight, J. P. Marangos J. P., and J. W. G. Tisch. Nonsequential double ionization at the single-optical-cycle limit. *Nature Physics*, 3:52–57, 2007.

[206] T. M. Fortier, P. A. Roos, D. J. Jones, S. T. Cundiff, R. D. R. Bhat, and J. E. Sipe. Carrier-envelope phase-controlled quantum interference of injected photocurrents in semiconductors. *Phys. Rev. Lett.*, 92(14):147403, 2004.

[207] M. Kress, T. Loffler, M. D. Thomson, R. Dorner, H. Gimpel, K. Zrost, T. Ergler, R. Moshammer, U. Morgner, J. Ullrich, and H. G. Roskos. Determination of the carrierenvelope phase of few-cycle laser pulses with terahertz-emission spectroscopy. *Nature Physics*, 2:327–331, 2006.

[208] T. Wittmann, B. Horvath, W. Helml, M. G. Schätzel, X. Gu, A. L. Cavalieri, Paulus G. G., and Kienberger R. Single-shot carrierenvelope phase measurement of few-cycle laser pulses. *Nature Physics*, 5:357, 2009.

[209] A. Rudenko, K. Zrost, C. D. Schröter, V. L. B. de Jesus, B. Feuerstein, R. Moshammer, and J. Ullrich. Resonant structures in the low-energy electron continuum for single ionization of atoms in the tunnelling regime. *J. Phys. B*, 37(24):L407, 2004.

[210] D.B. Milosević, G.G. Paulus, and W. Becker. High-order above-threshold ionization with few-cycle pulse: a meter of the absolute phase. *Opt. Exp.*, 11:1418–+, 2003.

[211] G. G. Paulus, F. Lindner, D.B. Milosević, and W. Becker. Phase-controlled single-cycle strong-field photoionization. *Physica Scripta*, 2004(T110):120, 2004.

[212] G. G. Paulus, F. Lindner, H. Walther, A. Baltuška, E. Goulielmakis, M. Lezius, and F. Krausz. Measurement of the phase of few-cycle laser pulses. *Phys. Rev. Lett.*, 91(25):253004, 2003.

[213] S. Micheau, Z. Chen, A.T. Le, and C. D. Lin. Quantitative rescattering theory for nonsequential double ionization of atoms by intense laser pulses. *Phys. Rev. A*, 79(1):013417, 2009.